Electroencephalographic Signal Source Estimation

Using Power Dissipation and Interface Surface Charge

by

Francisco Javier Solis

A Dissertation Presented in Partial Fulfillment
of the Requirements for the Degree
Doctor of Philosophy

Approved April 2020 by the
Graduate Supervisory Committee:

Antonia Papandreou-Suppappola, Chair
Visar Berisha
Daniel Bliss
Bahman Moraffah

ARIZONA STATE UNIVERSITY

May 2020

ABSTRACT

The inverse problem in electroencephalography (EEG) is the determination of form and location of neural activity associated to EEG recordings. This determination is of interest in evoked potential experiments where the activity is elicited by an external stimulus. This work investigates three aspects of this problem: the use of forward methods in its solution, the elimination of artifacts that complicate the accurate determination of sources, and the construction of physical models that capture the electrical properties of the human head. Results from this work aim to increase the accuracy and performance of the inverse solution process.

The inverse problem can be approached by constructing forward solutions where, for a know source, the scalp potentials are determined. This work demonstrates that the use of two variables, the dissipated power and the accumulated charge at interfaces, leads to a new solution method for the forward problem. The accumulated charge satisfies a boundary integral equation. Consideration of dissipated power determines bounds on the range of eigenvalues of the integral operators that appear in this formulation. The new method uses the eigenvalue structure to regularize singular integral operators thus allowing unambiguous solutions to the forward problem.

A major problem in the estimation of properties of neural sources is the presence of artifacts that corrupt EEG recordings. A method is proposed for the determination of inverse solutions that integrates sequential Bayesian estimation with probabilistic data association in order to suppress artifacts before estimating neural activity. This method improves the tracking of neural activity in a dynamic setting in the presence of artifacts.

Solution of the inverse problem requires the use of models of the human head. The electrical properties of biological tissues are best described by frequency dependent complex conductivities. Head models in EEG analysis, however, usually consider

head regions as having only constant real conductivities. This work presents a model for tissues as composed of confined electrolytes that predicts complex conductivities for macroscopic measurements. These results indicate ways in which EEG models can be improved.

TABLE OF CONTENTS

CHAPTER Page

CHAPTER Page

LIST OF TABLES

Table Page

LIST OF FIGURES

CHAPTER Page

Chapter 1

INTRODUCTION

1.1 Localization in the Brain

Phineas Gage was an American railroad worker who in 1848 was injured in an accident [1]. An explosion drove an iron rod through his head destroying part of his brain. Figure 1.1 shows a reconstruction of the trajectory of the rod. While he was able to physically recover from the accident, with his motor abilities essentially unaltered, his personality suffered in contrast dramatic changes. His speech became profanity laced, and his previous consistency and reliability as worker disappeared; he became untrustworthy and irresponsible. This famous medical case provided concrete, if anecdotal, evidence for the theory of localization in the brain. Proponents of this idea noted that the accounts of his behavioral change could be understood assuming that mental activities associated with social interactions are carried out at precise locations in the brain. With some modifications and many caveats this idea is now firmly established. While brain plasticity allows the partial remapping of brain functions in case of injury, normal mental tasks involve heightened activity at well defined locations. The study of the spatial and temporal characteristics of mental activity is nevertheless far from complete, and it is the purpose of the present work to contribute to the understanding of brain activity through improvements in the methods used for mapping external stimuli to their response locus in the brain.

A much less intrusive method of for studying brain activity, the electroencephalogram (EEG from now on), was developed in the early 20th century by Hans Berger and Richard Canton, following earlier experimentation in animals [2]. This method

Figure 1.1: The path of the iron rod through Phineas Gage' skull (from Ref.[1])

consists of the recording of electric potentials at the surface of the subjects scalps as shown in Figure 1.2. While these measurements are rather indirect, they do reflect the concrete localized activity inside the brain [3, 4]. More recently, other methods of investigation such as functional Magnetic Resonance Imaging (fMRI) [5] have been developed that provide more detailed views of brain activity, but EEG remains a central tool of research for its relative ease of use.

Not only is the observation of brain activity a subject of obvious scientific interest, but it clearly has very important practical applications. All methods of brain function mapping have been put to use as diagnostic tools in neuromedicine. In addition, the emerging field of brain interfacing is paving the way for the development of effective communication methods unmediated by motor activity, with many possible applications ranging from medicine to entertainment and nearly everything in between [6, 7].

There are several current applications of EEG to brain research and medicine. One is the determination of the location and other properties of the brain activity elicited

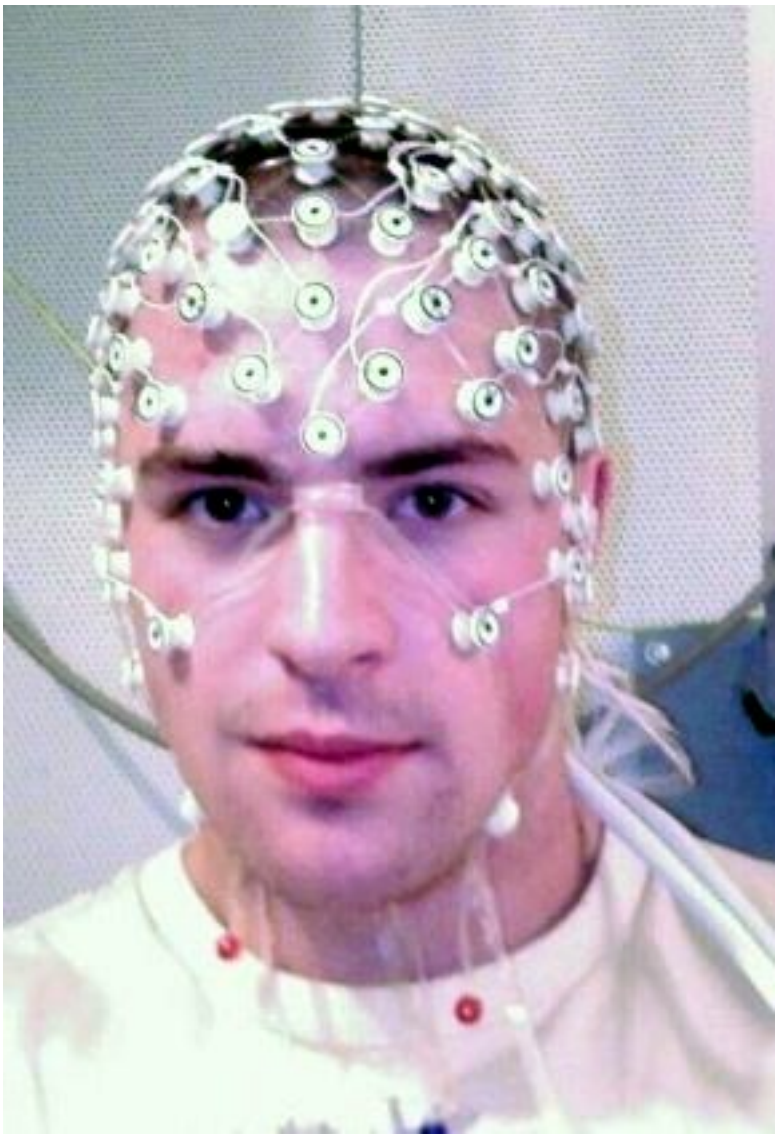

Figure 1.2: Subject with EEG electrodes ready for measurements; a far less intrusive alternative to brain investigations. Image by Douglas Myers, Public Domain.

by specific external stimuli [8]. Additionally, the characteristics of the EEG under different physiological conditions can be used as a tool for assessing the presence and features of special brain activity states such as sleep [9] or seizure attacks [10].

1.2 Motivation for This Work

The work presented here aims at improving the methods used in applications of EEG to brain activity localization. In a typical localization experiment, an external visual or auditory stimulus is presented to an individual who, in turn, responds in some way to it. Associated with the presence of the stimulus and the response, localized neural activity appears in the brain. The activity generates electric signals that are measured at the scalp, forming the EEG recording. These recordings can then be analyzed to determine the location of the neural activity. This determination is the *EEG inverse problem*. Such analysis requires the use of a model that can connect observations with features of the source. A practical approach to the solution of the inverse problem is to use filtering methods, where simulations of observation for assumed locations are compared to the actual data and lead to an estimation of the source location. This method requires the solution of the forward problem: the determination of scalp potentials from prescribed information about the source.

In addition to the filtering method mentioned above, there exists many approaches to the solution of the inverse problem. Some of these methods have been developed in considerable detail and implemented as software packages that allow an user to input EEG recordings and produce estimates of source localization, in addition to provide other information. Examples of these packages are EEGLAB [11] and OpenMEEG [12].

The EEG inverse problem cannot be considered, however, fully solved. A number of fundamental and practical problems still exist. Methods of solution of the forward

problem can be improved and should be better understood. Systematic errors due to the presence of artifacts need be addressed. The models most commonly used to relate sources and measurements do not capture important features observed in biological tissues. The present work contributes to the solution of these problems.

1.3 Contributions

The contributions of the present work are briefly summarized here, with more detailed and technical conclusions presented in the relevant chapters.

This work also presents a new approach to the elimination of artifacts in EEG. In addition to noise that can be effectively be considered as random. EEG signals can be disrupted by the presence of artifacts: large signals associated with identifiable physiological activity such as as yawning or eye movement. A common approach to the elimination of these artifacts has been to carry out an independent component analysis (ICA) of the EEG signal and identify some of the channels as associated to artifacts. A different method is devised here that uses Bayesian sequential estimation. A key difference between the methods is that the new approach can be used in dynamic settings where the decomposition implied by ICA is not effective.

This work also considers in detail the structure of forward solutions that are required in filtering approaches to the solution of the inverse problem. It is shown that the use of surface charge accumulation and power dissipation variables leads to an alternative formulation of the forward problem. Using descriptions of the human head as composed of a set of homogeneous regions, each with a constant conductivity, the forward problem is formulated as an boundary integral equation, which is equivalent to the commonly used Geselowitz integral equation (GIE), that uses the electric potential as variable. Using the properties of power dissipation, it is shown that important characteristics of the integral operators that appear in these equations obey

bounds in their eigenvalue sets. These bounds lead to a better understanding of the problem structure and are used to develop a novel approach to the solution of the forward problem. When surfaces are discretized, the integral operators are represented as matrices, which can be singular and make the forward solution ill-defined. The properties of the eigenvalues allow the construction of regularized versions of these matrices, rendering them invertible and thus allowing the solution of the problem. Other properties of the EEG system are also clarified using these variables.

All methods of solution of the inverse problem rely on physical models connecting measurement and neural source. The most common model, leading to the GIE, assumes that heads are composed of homogeneous regions each of constant conductivity. It is well established, however, that the electric properties of most biological tissues are best described by complex conductivities so that, when considered as part of electric circuits, they exhibit a complex impedance. In this work, a model for tissue conductivity is developed that explicitly considers the contribution of the confined electrolytes that appear in tissues. It is shown that they can account for most conductive properties of tissues at low frequencies These results indicate that physiological models that include consideration of complex conductivities should be incorporated in the study of EEG and the solutions of its associated inverse problem.

1.4 Content

This document is organized as follows. A description of the EEG and its biophysical interpretation appears in Chapter 2. The next set of chapters considers the dynamic estimation of sources in the presence of artifices The statistical methods required for its analysis are presented in Chapter 3. Their implementation, in the context of the EEG appears in Chapter 4.

The next few chapters detail progress on the use of charge and power variables to establish properties of the EEG forward solution. The structure of these variables is outlined in Chapter 5. Using these variables, it is possible to elucidate several properties of the integral operators that appear in the problem. The space of solutions of the relevant equations appear in Chapter 6. This chapter also discusses the application of these results to the construction of a method for forward solutions that takes advantage of the structure of the solution space. Details of the method implementation, along with sample results, appear in in Chapter 7.

Finally, a discussion of a model of tissue conductivity based on the properties of confined electrolytes appears in Chapter 8.

Chapter 2

EEG: PROPERTIES AND MODELS

EEG recordings are a fundamental tool of neuroscience. They provide a view of the large scale activity of the brain but have the drawback of coarseness and a relatively indirect relation with cellular level processes. This chapter reviews some of the fundamental characteristics of EEG and the models used to describe evoked potentials, that is, activities that results from external influences.

2.1 Basic EEG Recording Techniques

Modern EEG recordings use a set of electrodes placed against the scalp at a set of standardized positions. These electrodes record the potential difference between their location and a a common reference point. The electrodes are typically made of a silver alloy. This material is chosen so that the electrodes can quickly reach and maintain stable electroplates when placed against biological tissue [4]. The electrodes can be electrically passive or active. Passive electrodes typically present impedances of 10 to 20 kΩ, and in high precision applications, a key criteria is their uniformity. On the other hand, the electrodes themselves can be constructed with integrated circuitry to help in the detection and processing of signals. Standard EEG equipment often use sets of 16, 32, 64, 128, 160 or 256 electrodes, but manufacturers can provide a different set number. To identify their locations, a standard nomenclature has been developed and is referred to as the ten-twenty electrode system [13]. An example of how the labels are used is shown in Figure 2.1. When a small number of electrodes is used, they are applied to the scalp with collodion (a thick liquid acting as a glue). For large sets of electrodes, it is simpler to place the electrodes on a cap which is then

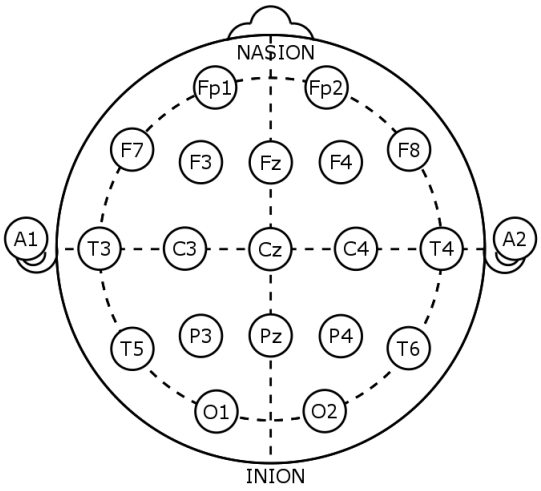

Figure 2.1: Labels in the ten-twenty nomenclature for a system of 20 electrodes. (Public domain image)

set against the scalp that is covered with gel in preparation.

2.2 Management and Processing of EEG Data

Contemporary use of EEG recordings takes advantage of digital means of recording, storing and processing of the data. Specialized software facilitate these tasks. For this work, we processed data using the freely available EEGLAB package that runs as an add-on to Matlab [11]. The package provides tools for data organization, selection and labeling. For visualization purposes, it provides rendering tools for two-dimensional (2D) and three-dimensional (3D) plots of the data, superimposed on semi-realistic shapes of heads. It includes processing tools to eliminate biases and noise. It also includes time-frequency analysis and independent component analysis tools.

2.3 EEG Recordings and Their Characteristics

EEG digital recordings are typically carried out at sampling rates if the order of 100 to a 1,000 Hz. Sampling at these frequencies is sufficient to capture essential

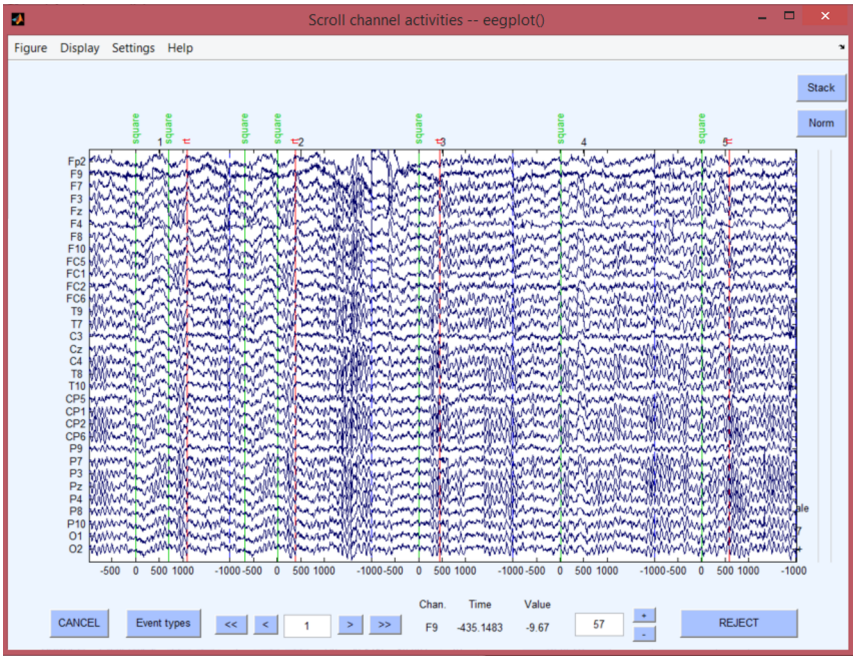

Figure 2.2: A typical digital display of EEG recordings in scroll format. Data for each sensor is identified by their name on the left. The scroll was generated by the EEGLAB interface.

brain responses. This is because experiments addressing evoked potentials present interesting characteristic behavior over time frames in the order of 100 ms. To resolve these features, it is therefore required to sample the electrode potentials at 200 Hz or higher. Such rate is feasible with common instrumentation.

The actual recordings of an EEG session are often presented in the form of a scroll, replicating the look of paper-recorded EEGs as shown in Figure 2.2. The recordings take the form of graphs of potential (with respect to a common fixed point) against time. The captured potentials are typically in the μV range, but are subject to a baseline drift that can be in the scale of the actual measurement. Elimination of these biases requires preprocessing of the data.

Electrical activity in the brain, as measured by EEG, can be broadly classified into spontaneous EEG and evoked potentials. Evoked potentials are recordings of responses to experimental situations that introduce time-localized attention grabbing

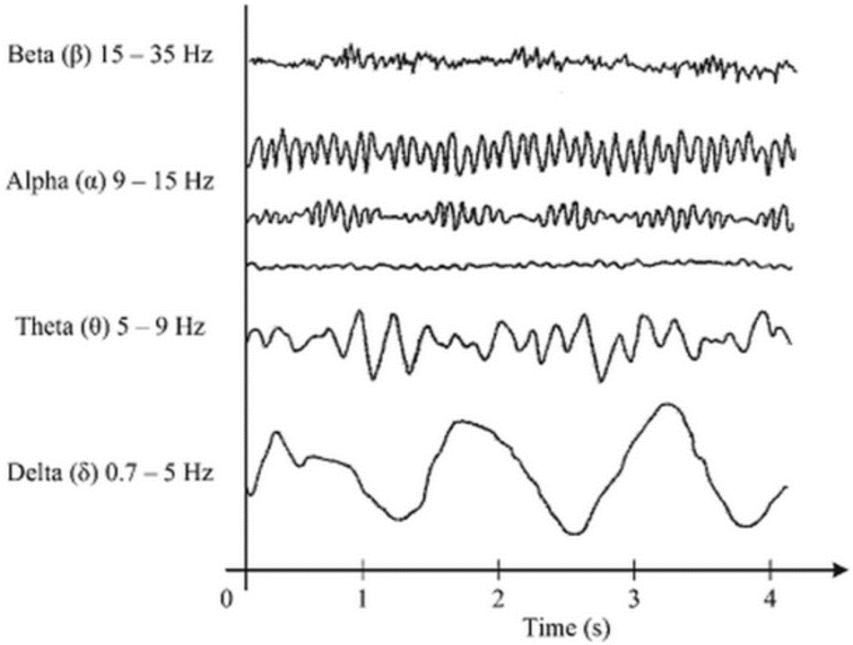

Figure 2.3: Examples of EEG brain waves in different frequency bands. (Image by Chatterjee and Miller [14]).

events. Spontaneous EEG corresponds to experimental conditions that, while controlled, do not introduce these events.

A dominant feature of spontaneous EEG is the presence of well defined waves of relatively steady frequency [3]. These waves are typically classified by their frequency range as illustrated in Figure 2.3. Alpha (α) waves are oscillations in the frequency range 8-13 Hz. They are associated with a relaxed but wakeful state; in EEG recordings, these waves have amplitudes up to 50 μV. The beta (β) waves, in the 14-26 Hz frequency range are an indicator of conscious activity with amplitudes in the range of 30 μV. The gamma (γ) waves comprise any high frequency activity, at 30 Hz and above. Delta (δ) waves, on the other hand, are low frequency oscillations in the range 0.7-5 Hz, primarily associated with deep sleep. Finally, theta (θ) waves, in the 5-9 Hz range, indicate transitional activity from wakefulness to sleep and are also associated with subconscious mental activity.

Evoked potentials are responses to specific stimuli, and as such, they are localized in time, occurring right after the stimulus.

2.4 Biophysical Origin of EEG

All human conscious processes are effected by electrical activity in the brain. In addition, many motor and sensory functions are processed in the brain in close interaction with the rest of the nervous system. Physiologically, the brain can be divided into three regions, the brainstem, the cerebellum and the cerebrum [15]. The brainstem connects the brain with the spinal cord providing means for signal transmission. The cerebellum is associated with muscular control, and cognitive functions are associated with cerebrum processes. The outer part of the cerebrum is known as the cerebral cortex. At a cellular level, it contains about 10^{10} neurons that are strongly interconnected. These neurons can have up to 10^5 synapses, which are connections with other neurons capable to transmit signals.

The fundamental activity of neurons is electric in nature. Structurally, neurons have two special types of appendages, dendrites and an axon, as shown in the scheme in Figure 2.4. The dendrites collect signals transmitted to them by other neurons at synapses; while this transmission is of chemical nature, it only occurs when the electric potential at the synapse location satisfies certain conditions. The neuron processes this information and emits, in turn, electric signals that propagate through the axon at speeds of order of 1 m/s and eventually excite the axon synapses to transfer information to other neurons. The potentials generated change the rest conditions by potential differences in the order of 10 mV. The generation and transmission of these electric pulses are complex processes that require the intake and ejection of ions at specific locations to create the net potential changes and currents associated with the signals. As shown in the scheme of Figure 2.5, the local modified potential travels

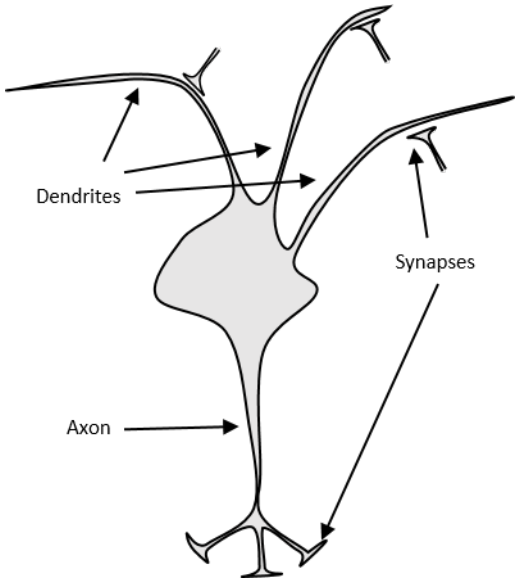

Figure 2.4: Scheme of a neuron showing its dendrites and axon and a number of synapses.

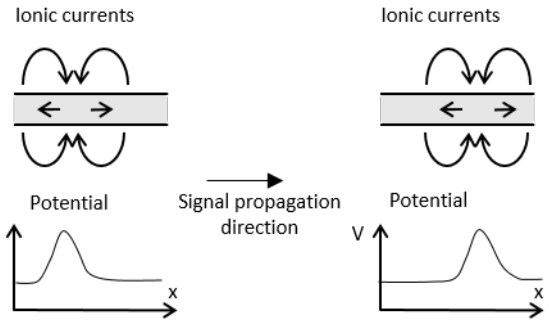

Figure 2.5: Scheme of the ionic current structure associated with signal transmission along an axon.

unidirectionally away from the neuron body along the axon, and in the process, generates currents inside the axon but also in the extracellular region; it is the collective effect of these currents that is associated with EEG measurements.

2.5 Forward Models for EEG

In settings that involve evoked potentials, the fundamental model for the interpretation of EEG results assumes that the response to external stimuli consists of highly localized activity in the brain. It also assumes that this activity is reflected

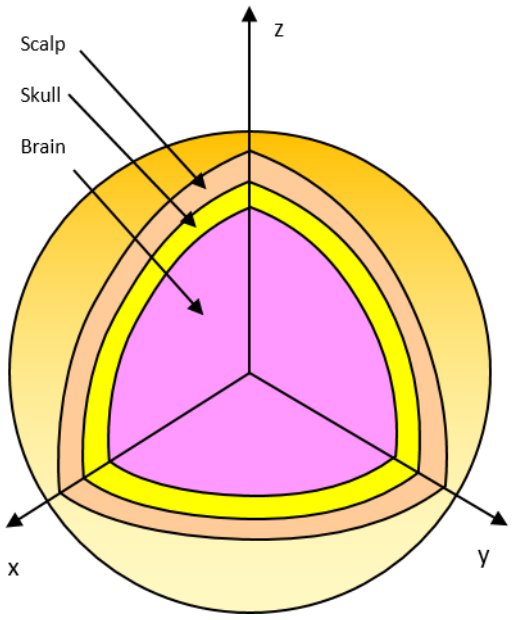

Figure 2.6: Scheme of the three sphere model of the head.

in the emergence of a relatively large but localized current. The activity of a large number of neurons in a specific region adds up to a coherent current with an associated electric potential field. Using this idea, it is possible to construct models for the relation between the source currents and the measured EEGs. Extensive work has been carried out towards this goal. See reviews, for example, in [16, 17].

In practical applications, however, the most commonly used and relatively realistic model is a three-layer model that considers currents through a set of homogeneous environments [18–24]. A spherical head model with three layers is shown in Figure 2.6.

The three-layer model assumes that the currents in the extracellular region of the brain flow in an environment that can be described as a homogeneous conductor, which therefore obeys the local form of Ohm's law given by

$$\mathbf{J} = \sigma \mathbf{E}. \tag{2.1}$$

Here, $\mathbf{J}$ is the current density, $\mathbf{E}$ is the electric field and σ is the conductivity of the brain's extracellular region. In the brain region, it is assumed that the collective effect of an evoked response is to create a strong net current, that can be represented by a set of sources and sinks in a relatively small region. The strength and space distribution of these sources and sinks can be approximated, as a single source and a companion sink of the same strength. The source and sink locations are indicated by the 3D position vectors $\mathbf{x}_s$, and $\mathbf{x}_k$. Their separation is $\mathbf{a} = \mathbf{x}_s - \mathbf{x}_k$ and their midpoint is $\mathbf{x}_c = (\mathbf{x}_s + \mathbf{x}_k)/2$. The current emerging from the source is I and the same current disappears at the sink. The current sinks and sources correspond to non-zero contributions of the divergence of the current field; each source and sink divergence can be represented as a delta function. The divergence of the current can be expanded as:

$$\nabla \cdot \mathbf{J} = I(\delta(\mathbf{x} - \mathbf{x}_s) - \delta(\mathbf{x} - \mathbf{x}_k)) \approx I\,\mathbf{a} \cdot \nabla\delta(\mathbf{x}-\mathbf{x}_c). \tag{2.2}$$

where ∇ is the gradient operator. Using the relation between the current and the field, and assuming that there are D regions with net source-sink pairs centered at locations $\mathbf{x}_c^{(d)}$, $d = 1, \ldots, D$, the electric field must satisfy

$$\nabla \cdot \mathbf{E} = \sum_{d=1}^{D} \mathbf{q}_d\, \delta'(\mathbf{x} - \mathbf{x}_c^{(d)}), \tag{2.3}$$

where $\mathbf{q}_d = I_d\, \mathbf{a}_d\, \sigma$ is the strength of the effective dipole associated with the d-th source-sink pair. Finally, the electric field $\mathbf{E} = -\nabla\psi$ can be written as the gradient of the potential ψ so that

$$\nabla^2\psi = -\sum_{d=1}^{D} \mathbf{q}_d \cdot \nabla\delta(\mathbf{x} - \mathbf{x}_c^{(d)}) \tag{2.4}$$

The structure of this equation indicates that the localized currents generate an electric

field identical to that of a static set of dipoles in homogeneous media.

In the multilayer model, it is necessary to also require the potential to satisfy two boundary conditions at each interface. Each interface bounds two regions; at all points of the interface, the potential must be continuous and for regions labeled a and b, one can write:

$$\psi|_a = \psi|_b \tag{2.5}$$

where the vertical $|_a$ is used to denote the evaluation at points in the interface in the region indicated by the subindex. Additionally, as current must be conserved, the components of the current normal to the interface must also be equal. Assuming that the unit vector normal to the interface is $\mathbf{n}$, the condition can be written as

$$\mathbf{J} \cdot \mathbf{n}|_i = \mathbf{J} \cdot \mathbf{n}|_{i+1}. \tag{2.6}$$

For models that assume homogeneous media, the total potential is linear on the dipole moments associated with the currents. If the solutions for the potential $\psi(\mathbf{r}; \mathbf{r}_d, \mathbf{q}_d)$ evaluated at position $\mathbf{r}$, due to a dipole of magnitude $\mathbf{q}_d$ located at position $\mathbf{r}_d$, are known, the net potential is simply the sum of the D solutions:

$$\psi(\mathbf{r}; \mathbf{r}_1, \ldots, \mathbf{r}_D, \mathbf{q}_1, \ldots, \mathbf{q}_D) = \sum_{d=1}^{D} \psi(\mathbf{r}; \mathbf{r}_d, \mathbf{q}_d). \tag{2.7}$$

The solutions for individual dipoles are obtained as follows. A standard Cartesian system of coordinates is used, as shown in Figure 2.7. In the brain region, a change of coordinates can always be carried out so as to position the dipole at a point in the z-axis and to have the dipole lying in the x-z plane. The solution ψ_I, for a single dipole source in an infinite homogeneous space, is given by

$$\psi_I(\mathbf{r}; \mathbf{r}_d, \mathbf{q}_d) = \frac{1}{4\pi} \frac{1}{|\mathbf{r} - \mathbf{r}_d|^3} \mathbf{q} \cdot (\mathbf{r} - \mathbf{r}_d). \tag{2.8}$$

In a finite sphere or in a region bounded by two concentric spheres, the more general solution ψ_G to the Poisson equation 2.4, with a single dipole, has the form

$$\psi_G(\mathbf{r}) = \sum_{n=0}^{n=\infty} \sum_{m=-n}^{m=n} \left(A_{n,m} r^n + B_{n,m} r^{-(n+1)}\right) P_n^m(\cos\theta)\, e^{i\,m\phi}. \tag{2.9}$$

Here $\mathbf{r}$ is the point at which the potential is evaluated Its spherical coordinates expression is $\mathbf{r} = (r, \theta, \phi)$. The expansion uses two indices, n, m, and for each pair of values, P_n^m denotes the associated Legendre polynomial. The imaginary unit is $i = \sqrt{-1}$. In the dipole source case, when the orientation described above is used, only the terms with $|m| \leq 1$ are non-zero. In the brain region, the series expansion of the infinite space solution, equation 2.8, determines the coefficients $B_{n,m}$. The coefficients $A_{n,m}$ for this region and the coefficients for the rest of the concentric spheres are determined from the solution to the boundary conditions in equations 2.5 and 2.6, along with the requirement that outside the conductive regions the potential should vanish at large distances. Schematically, the net potential can be written as the dot product of a vector function $\mathbf{G}$ and the dipole moment $\mathbf{q}_d$:

$$\psi(\mathbf{r}; \mathbf{r}_d, \mathbf{q}_d) = \mathbf{G}(\mathbf{r}, \mathbf{r}_d) \cdot \mathbf{q}_d. \tag{2.10}$$

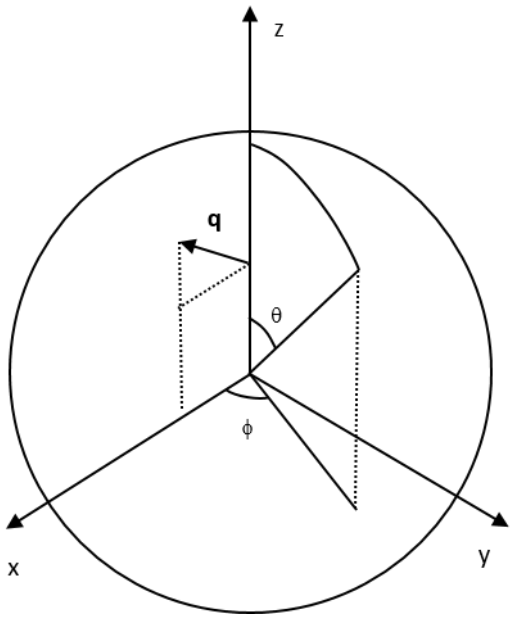

Figure 2.7: A dipole with position along the z-axis lying in the x-z plane. The figure shows the polar θ, and and azimuthal ϕ angles for a generic position.

Chapter 3

STATISTICAL PROCESSING METHODS

This chapter provides background on some statistical methods that have been used in analyzing EEG recordings. The background information follows mostly from [25].

3.1 Dynamic Parameter Estimation Using Kalman Filtering

A state space model provides the representation of a physical dynamic system that can be described using continuous state variables for which measurements can be used to estimate the states. These systems are often considered as being observed at a sequence of equally spaced time steps. Mathematically, the relevant relations between the system state $\mathbf{z}_t$ at time step t, and its measurements or observed properties $\mathbf{y}_t$ can be presented using the pair of equations

$$\mathbf{z}_t = g(\mathbf{u}_t, \mathbf{z}_{t-1}, \theta, \epsilon_t) \tag{3.1}$$

$$\mathbf{y}_t = h(\mathbf{z}_t, \mathbf{u}_t, \gamma_t) \tag{3.2}$$

where $\mathbf{u}_t$ is a vector of optional control variables, ϵ_t and γ_t are the system and observation noise variables, respectively, and θ are the model parameters. The function $g(\cdot)$ is the transition function, while $h(\cdot)$ provides the observation model. The general goal of the analysis of the system is the recursive determination of the belief state $p(\mathbf{z}_t|\mathbf{y}_{1:t}, \mathbf{u}_{1:t}, \theta)$. The belief state is the probability that the system be described by the parameter state vector $\mathbf{z}_t$ at time step t, given observations $\mathbf{y}_{1:t}$ from time steps 1 to t. It is assumed that the parameters θ and the control variables $\mathbf{u}_{1:t}$ are known.

The Kalman filter (KF) is a method for estimating the dynamic state parameter vector $\mathbf{z_t}$, under certain conditions on the state space model [26, 27]. In particular, the KF assumes that the transition model and the observation model are both linear so that

$$\mathbf{z}_t = \mathbf{A}_t \mathbf{z}_{t-1} + \mathbf{B}_t \mathbf{u}_t + \epsilon_t \tag{3.3}$$

and

$$\mathbf{y}_t = \mathbf{C}_t \mathbf{z}_t + \mathbf{D}_t \mathbf{u}_t + \gamma_t. \tag{3.4}$$

It is also assumed that the system and observation noise are both Gaussian, namely,

$$\epsilon_t \sim \mathcal{N}(\mathbf{0}, \mathbf{Q}_t) \tag{3.5}$$

and

$$\gamma_t \sim \mathcal{N}(\mathbf{0}, \mathbf{R}_t), \tag{3.6}$$

where $\mathcal{N}(\mu, \mathbf{C})$ denotes a Gaussian distribution with mean μ and contrivance matrix $\mathbf{C}$.

The solution to the KF is iterative. In particular, assuming an initial density $p(z_0|y_0, u_0)$, the system model is used to obtain

$$p(\mathbf{z}_t|\mathbf{y}_{1:t}, \mathbf{u}_{1:t}) = \mathcal{N}(\mathbf{z}_t|\mu_t, \Sigma_t). \tag{3.7}$$

The prediction stage of the KF is used to obtain

$$p(\mathbf{z}_{t+1}|\mathbf{y}_{1:t}, \mathbf{u}_{1:t}) \;\; = \;\; \mathcal{N}(\mathbf{z}_t|\mu_{t+1|t}, \Sigma_{t+1|t}) \tag{3.8}$$

with

$$\mu_{t+1|t} = \mathbf{A}_{t+1}\mu_t + \mathbf{B}_{t+1}\mathbf{u}_t, \tag{3.9}$$

and

$$\Sigma_{t+1|t} = \mathbf{A}_{t+1}\Sigma_t\mathbf{A}_t^T + \mathbf{Q}_t. \tag{3.10}$$

The new measurement y_{t+1} at the update stage and Bayes' rule are then used to obtain

$$p(\mathbf{z}_{t+1}|\mathbf{y}_{t+1}, \mathbf{y}_{1:t}, \mathbf{u}_{1:t+1}) \propto p(\mathbf{y}_{t+1}|\mathbf{z}_t, \mathbf{u}_t)p(\mathbf{z}_{t+1}|\mathbf{y}_{1:t}, \mathbf{u}_{1:t+1}). \tag{3.11}$$

Explicitly, the result is given by

$$p(\mathbf{z}_{t+1}|\mathbf{y}_{1:t+1}, \mathbf{u}_{1:t+1}) = \mathcal{N}(\mathbf{z}_{t+1}|\mu_{t+1}, \Sigma_{t+1}) \tag{3.12}$$

with

$$\mu_{t+1} = \mu_{t+1|t} + \mathbf{K}_{t+1}\mathbf{r}_{t+1} \tag{3.13}$$

and

$$\Sigma_{t+1} = (\mathbf{I} - \mathbf{K_t}\mathbf{C}_t)\Sigma_{t+1|t}. \tag{3.14}$$

In these expressions $\mathbf{r}_t$ is the residual, that is, the difference between the predicted and actual observation

$$\mathbf{r}_t = \mathbf{y}_t - \hat{\mathbf{y}}_t. \tag{3.15}$$

The predicted observation is given by

$$\hat{\mathbf{y}}_{t+1} = \mathbb{E}[\mathbf{y}_{t+1}|\mathbf{y}_{1:t}] = \mathbf{C}_{t+1}\mu_{t+1|t} + \mathbf{D}_{t+1}\mathbf{u}_{t+1}, \tag{3.16}$$

where $\mathbb{E}$ denotes statistical expectation. The Kalman gain $\mathbf{K}_c$ in (3.14) is

$$\mathbf{K}_{t+1} = \Sigma_{t+1|t}\mathbf{C}_{t+1}^T\mathbf{S}_{t+1}^{-1} \tag{3.17}$$

and the auxiliary matrix is defined as

$$\mathbf{S}_{t+1} = \mathbf{C}_{t+1}\Sigma_{t+1|t}\mathbf{C}_{t+1}^T + \mathbf{R}_t \tag{3.18}$$

where $\mathbf{R}_{t+1}$ is the covariance of the measurement noise at time step $t+1$.

3.2 Particle Filtering

The particle filtering approach takes advantage of Monte Carlo simulations to carry out the Bayesian inference of the probability distribution of a system state given a set of previous observations and a known model [28, 29]. Unlike the KF approach, this method does not require linearity in the state space model or Gaussian distributed noise.

The model produces an approximation to the probability distribution of the state of the system of the form

$$p(\mathbf{z}_{1:t}|\mathbf{y}_{1:t}) \approx \sum_{s=1}^{S} \hat{w}_t^s \delta(\mathbf{z}_{1:t} - \mathbf{z}_{1:t}^{(s)}) \tag{3.19}$$

where $\hat{w}^{(s)}$ are normalized weights. That is, the probability distribution is then derived from a collection of particles determined from previous observations.

In Monte Carlo methods, the generation of updated weights is obtained using a proposal function $q(\mathbf{z}_{1:t}^s|\mathbf{y}_{1:t})$. The importance weights are then

$$\hat{w}_t^s \propto \frac{p(\mathbf{z}_{1:t}|\mathbf{y}_{1:t})}{q(\mathbf{z}_{1:t}|\mathbf{y}_{1:t})} \tag{3.20}$$

which can then be normalized as

$$\hat{w}_t^{(s)} = \frac{w_t^{(s)}}{\sum_{s'} w_t^{(s')}}. \tag{3.21}$$

A number of simplifications can be applied to this general scheme. In particular, it is common to construct the proposal function so as to have a recursive structure of the form

$$q(\mathbf{z}_{1:t}|\mathbf{y}_{1:t}) = q(\mathbf{z}_t|\mathbf{z}_{1:t}, \mathbf{y}_{1:t}) q(\mathbf{z}_{1:t-1}|\mathbf{y}_{1:t-1}). \tag{3.22}$$

In this way, the importance weights also acquire a sequential structure

$$w_t^{(s)} = \frac{p(\mathbf{y}_t|\mathbf{z}_t^{(s)}) p(\mathbf{z}_t^{(s)}|\mathbf{z}_{t-1}^{(s)})}{q(\mathbf{z}_t^{(s)}|\mathbf{z}_{1:t-1}^{(s)}, \mathbf{y}_{1:t})}. \tag{3.23}$$

A further common simplification assumes that only the most recent measurements are needed for the construction of the proposal. This is:

$$w_t^{(s)} \propto w_{t-1}^{(s)} \frac{p(\mathbf{y}_t|\mathbf{z}_t^{(s)}) p(\mathbf{z}_t^{(s)}|\mathbf{z}_{t-1}^{(s)})}{q(\mathbf{z}_t^{(s)}|\mathbf{z}_{t-1}^{(s)}, \mathbf{y}_t)}. \tag{3.24}$$

The most common proposal distribution is obtained from sampling the posterior distribution

$$q(\mathbf{z}_t|\mathbf{z}_{t-1}^{(s)}, \mathbf{y}_t) = p(\mathbf{z}_t|\mathbf{z}_{t-1}^{(s)}) \tag{3.25}$$

and the weights simplify to

$$w_t^{(s)} \propto w_{t-1}^{(s)} p(\mathbf{y}_t|\mathbf{z}_t^{(s)}). \tag{3.26}$$

Finally, the posterior can be approximated as

$$p(\mathbf{z}_{1:t}|\mathbf{y}_{1:t}) \approx \sum_{s=1}^{S} \hat{w}_t^{(s)} \delta(\mathbf{z}_t - \mathbf{z}_t^{(s)}) \tag{3.27}$$

so that only the most recent step is explicitly needed for an update.

This method is generally applied with an added resampling step. The purpose is to correct for the fact that often a number of the particles have negligible weights, and in effect, the sampling is using a reduced number of particles.

3.3 Rao-Blackwellized Particle Filters

If the state space model can be factored into a linear and nonlinear form, then the computational complexity of particle filtering can be reduced. This is the case for some models for the observed potentials in EEG such as the one described in section 2.5. In these models, the dipole moments $\mathbf{q}$ and the dipole positions$\mathbf{r}$ play in fact such roles. The variable $\mathbf{q}$ enters into the model in such a simple way that its distribution can be exactly determined as long as that of $\mathbf{r}$ is known. In this way one only has to sample $\mathbf{r}$. The particles of the filter represent specific values for the variables $\mathbf{r}$ but carry a distribution for the variables $\mathbf{q}$. The corresponding estimation method is called the Rao-Blackwellization of the particle filtering. Its detailed description and application to EEG recordings can be found in [29–31].

3.4 Probability Hypothesis Density Filtering

The method of probability hypothesis density filtering (PHDF) allows the treatment of problems where it is required to dynamically estimate the parameters of a number of objects simultaneously; the number of the objects can be unknown and vary with time. Instead of using the full probability distribution for the objects, the PHDF uses, as a set of approximations where only knowledge of the first moment of the distribution is required [32, 33]. The first moment of the multiparticle distri-

bution is the particle probability density in state space. The number and state of the objects is determined from the particle probability density by associating objects to local maxima of the distribution. These objects are assumed interchangeable and therefore the set of particles is described as a random finite set (RFS).

The PHDF setting considers a number of objects N_t present at time t, and a corresponding set of M_t measurements. The collections of objects state parameters and measurements are represented collectively as

$$\mathbf{Z}_t = \{\mathbf{z}_t^1, \ldots, \mathbf{z}_t^{N_t}\} \tag{3.28}$$

and

$$\mathbf{Y}_t = \{\mathbf{y}_t^1, \ldots, \mathbf{y}_t^{M_t}\}. \tag{3.29}$$

The PHDF method seeks to characterize the posterior density functions $p(\mathbf{z}_t|\mathbf{y}_{t-1})$ by means of an intensity function $\lambda(\mathbf{z}_t|\mathbf{y}_{t-1})$. This function is effectively a density in state space, and technically is the first moment of the posterior density $p(\mathbf{z}_t|\mathbf{y}_{t-1})$. The prediction at time t is obtained from knowledge of previous intensities and terms corresponding to new particles:

$$\begin{aligned}\lambda(\mathbf{z}_t|\mathbf{y}_{t-1}) = \int & [P_{t|t-1}(\mathbf{z}_{t-1})p(\mathbf{z}_t|\mathbf{y}_{t-1}) + \\ & \lambda^{spn}(\mathbf{z}_t|\mathbf{y}_{t-1})]\lambda(\mathbf{z}_{t-1}|\mathbf{y}_{t-1})d\mathbf{x}_{t-1} + \lambda^{new}(\mathbf{z}_t|\mathbf{y}_t).\end{aligned} \tag{3.30}$$

In this expression, λ^{spn} is the intensity function of particles spawned by already present particles while λ^{new} corresponds to new particles. The posterior is updated using new measurements:

$$\lambda(\mathbf{z}_t|\mathbf{y}_t) = (1 - P^D(\mathbf{z}_t))\lambda(\mathbf{z}_t|\mathbf{y}_{t-1}) + \sum_{Z_k} \frac{P^D(\mathbf{z}_t)p(\mathbf{y}_t|\mathbf{z}_t)\lambda(\mathbf{z}_t|\mathbf{y}_{t-1})}{\lambda^{clutter}(\mathbf{y}_t) + \int P^D(\tilde{\mathbf{z}}_t)p(\mathbf{z}_t|\tilde{\mathbf{z}}_t)\lambda(\tilde{\mathbf{z}}_t|\mathbf{y}_{t-1})d\tilde{\mathbf{z}}_k},$$

where $P^D(\mathbf{z}_t)$ is the probability that a source with state parameter $\mathbf{z_t}$ at time t still exists at time $t+1$, and $\lambda^{clutter}$ is a contribution to the intensity associated to the presence of clutter in the state space.

The PHDF can be implemented as a particle filter [34]. The key assumption is that the intensity function can be represented as a set of T_t particles with corresponding weights $w_t^{(n)}$:

$$\lambda(\mathbf{z}_t|\mathbf{y}_t) \approx \sum_{n=1}^{T_{t-1}} w_t^{(n)} \delta(\mathbf{z}_t - \mathbf{z}_t^{(n)}) + \lambda^{new}(\mathbf{z}_t|\mathbf{y}_t). \tag{3.31}$$

It is assumed that the values $\{\mathbf{z}_t^{(n)}\}_n^{T_{t-1}}$ are drawn from the proposal density $q(\cdot|\mathbf{z}_t^{(n)}, \mathbf{y}_t)$ while the remaining particles are drawn from the density $p(\cdot|\mathbf{y}_t)$,

$$\mathbf{z}_t^{(n)} \sim \begin{cases} q(\cdot|\mathbf{y}_t^{(n)}, \mathbf{z}_t) & n = 1, \ldots, T_{t-1} \\ p(\cdot|\mathbf{y}_t) & n = T_{t-1}+1, \ldots, T_t \end{cases} \tag{3.32}$$

so that the total predicted intensity is

$$\lambda(\mathbf{y}_t|\mathbf{z}_t) \approx \sum_{n=1}^{T_t} w_t^{(n)} \delta(\mathbf{z}_t - \mathbf{z}_t^{(n)}). \tag{3.33}$$

The difference between expressions (3.31) and (3.33) is in the use of $T_t - T_{t-1}$extra particles.

3.5 Independent Component Analysis

Independent component analysis (ICA) is a method for signal analysis [35–37] that has been extensively used in the context of EEG investigations [38, 39].

ICA is based on the idea that the mixture of two or more signals with different spectral properties add up to a net signal that has distinctive non-Gaussian properties. The basic example is the addition of two sinusoidal waves with different frequencies, each contributing to two different measuring channels. A sampling of the waves in the measuring channels leads to a set of points with essentially uniform density living in a region bounded by a rectangle. In contrast, a Gaussian model of these measurements leads to a density with elliptical geometry. The ICA method takes advantage of these differences to recover the initial independent components that make up the signal.

Following reference [37], one can consider the composition of an observed signal $\mathbf{x}$ in terms of a set of statistically independent variables that can be arranged in a column vector $\mathbf{s}$ with dimension equal to the number of assumed components. The observation is assumed linear on these components:

$$\mathbf{x}=\mathbf{A}\mathbf{s}. \tag{3.34}$$

The ultimate goal is to obtain a description of the components $\mathbf{s}$ in terms of the observation. That is, to construct the inverse $\mathbf{W}$ of the mixing matrix $\mathbf{A}$:

$$\mathbf{s} = \mathbf{W}\mathbf{x}. \tag{3.35}$$

The identification of the independent components requires the careful definition of independence in itself. In particular, two of the entries of the vector $\mathbf{s}$, s_i and s_j, are independent if their joint probability distribution is the product of their individual distributions:

$$p(s_1, s_2) = p_1(s_1)p_2(s_2). \tag{3.36}$$

This relation implies other more directly accessible conditions. It leads to a factor-

ization, and thus uncorrelatedness of the expectations:

$$\mathbb{E}[s_1 s_2] = \mathbb{E}[s_1]\mathbb{E}[s_2]. \tag{3.37}$$

This is, however, not a strong enough requirement for the identification of the independent components and other measures of non-Gaussianity, and therefore indicators of the presence of independent components, are necessary. A commonly used quantifier is the kurtosis of a random variable s, given by:

$$kurt(s) = \mathbb{E}[s^4] - 3\mathbb{E}[s^2]^2. \tag{3.38}$$

For a Gaussian distribution, this value is simply zero and therefore is a concrete measure of the deviation from Gaussianity.

Algorithmically, it is possible to pursue the identification of the linear subspaces with largest deviations from Gaussian behavior. The original sampled data is first normalized so as to have unit variance in all directions. A maximum of kurtosis indicates the location of an independent component. The algorithm can then recursively pick all the independent components. Other methods to obtain the ICA decomposition use other measures of the non-Gaussianity as indicators of independence.

3.6 Gaussian Mixture Models

To aid in the classification of complex data, it is useful to describe it in a relatively simple parametric way. Gaussian Mixture Models (GMM) provide an approximation to the distributions of variables that capture the location of maxima of a probability density as well as the spread of the distribution around those maxima [40]. Algorithms associated to GMMs aim to construct the best representation of a distribution by means of a Gaussian mixture. The mixture selected is the one that maximizes the likelihood of the observed data under the proposed distribution.

The general setup of the construction of GMMs is the assumption that the approximate probability distribution is

$$p(\mathbf{x}|\theta) = \sum_{k=1}^{K} \pi_k \mathcal{N}(\mathbf{x}|\mu_k, \Sigma_k) \tag{3.39}$$

where it is assumed that there are K components, with weights π_k, each contributing a Gaussian distribution with mean μ_k and variance Σ_k. These parameters are collectively represented by θ. The likelihood of an observed set, given a particular value of parameters is

$$\ell(\theta) = \sum_i \log p(x_i|\theta). \tag{3.40}$$

The optimal parameters are

$$\hat{\theta} = arg(\max(\ell(\theta))). \tag{3.41}$$

A solution to the problem is often sought using the expectation-maximization (EM) algorithm. In this iterative approach, the E and M steps are carried out in an alternating sequence. In the E step, one calculates the so called responsibilities r_{ik}

$$r_{ik} = \frac{\pi_k p(x_i|\theta_k^{(t-1)})}{\sum \pi_{k'} p(x_i|\theta_{k'}^{(t-1)})}. \tag{3.42}$$

These are, in essence, the probabilities that a given observation i is explained by component k. In the M step, the weights are updated as

$$\pi_k = \frac{1}{N} \sum_i r_{ik}. \tag{3.43}$$

The mean and covariance are updated as

$$\mu_k = \frac{\sum r_{ik} x_i}{r_k} \tag{3.44}$$

and

$$\Sigma_k = \frac{\Sigma r_{ik} x_i x_i^T}{r_k} - \mu_k \mu_k^T. \tag{3.45}$$

The algorithm can be stopped when the iterations do not further increase the likelihood by a preset value.

Chapter 4

ESTIMATION OF TIME VARYING SOURCES

4.1 Background

The problem of extracting information from evoked potentials measured through EEG and MEG has been addressed in many previous works before. As noted above, it is a basic assumption of the modeling of these recordings that it is possible to represent the potentials by means of a small set of activated localized dipoles with dynamic amplitudes but fixed locations and orientations. Such determination is known in the literature as the EEG/MEG inverse problem. As reviewed, for example, in [8], several methods have been employed in their solution. The most commonly used approaches have been the use of (a) multiple signal classification (RAP MUSIC) [41, 42], (b) spatial filters or beamformers [43, 44], and (c) Bayesian methods [45–53]. One of the reasons for the popularity of Bayesian methods is their previous use in tracking problems. Here the dipoles become the object whose position is sought given the EEG measurements which act as the detection tools. The approached taken in this work follows the work previously carried out by the Papandreou-Suppappola group [54–58] and that of the MIDA group [48, 51].

4.2 Data Structures and Model

To apply the particle filter method to EEG evoked potential problems it is necessary to set the problem in a structure that matches the format of particle filtering techniques. In addition, it can be shown that a number of useful simplifications such as the Rao-Blackwellization of the filtering can be applied in this setting. The precise

structure used in this work is described in this section.

First, the goal of the particle filters is to discern the location, as a function of time, of a set of dipole currents that best matches the observed experimental data. During a single experiment, of duration T seconds, the sensor data is sampled at a frequency f. In a given experiment each of the S sensors acquires $N = fT$ samples. If the experiment is repeated K times, the total sensor data can be expressed as K matrices of size $S \times N$; the symbol $Z^{(k)}$ is used for each of these matrices. The entries of the matrices are $z_{s,n}^{(k)}$ where k indexes the experiment, s indexes the sensor and n indexes the sample number. It is also convenient to write $\mathbf{z}_n$for the vector of measurements at time step n. The experiment number k is omitted except when actually needed as in most cases only one experiment is analyzed at a time and therefore, explicitly:

$$\mathbf{z}_n = [z_{1,n}, \ldots, z_{s,n}, \ldots, z_{S,n}]^T. \tag{4.1}$$

On the other hand, it is assumed that there exist D dipoles that produce the relevant signal observed at the sensors. The position and moment of the dipoles at time step n for experiment k, can be organized as a vector $\mathbf{X}_n^{(k)}$ of the form

$$\mathbf{X}_n^{(k)} = [\mathbf{r}_{1,n}^{(k)}, \mathbf{q}_{1,n}^{(k)}, \ldots, \mathbf{r}_{d,n}^{(k)}, \mathbf{q}_{d,n}^{(k)}, \ldots, \mathbf{r}_{D,n}^{(k)}, \mathbf{q}_{D,n}^{(k)}]^T. \tag{4.2}$$

Each of the vectors of position $\mathbf{r}$ and dipole moment $\mathbf{q}$ is a 1×3 vector, with their Cartesian coordinates as entries.

As presented in Chapter 2 these dipoles create a potential $\psi(\mathbf{r}_s)$ at the locations $\mathbf{r}_s$of the sensors, and their contributions are additive. The model discussed in that chapter can be written as

$$z_{s,n} = \psi(\mathbf{r}_s; \mathbf{X}_n) = \sum_{d=1}^{D} \psi(\mathbf{r}_s; \mathbf{r}_{d,n}, \mathbf{q}_{d,n}). \tag{4.3}$$

Furthermore, since the potential is linear on the moments, one can also write, adapting (2.10),

$$z_{s,n} = \sum_{d=1}^{D} G_s(\mathbf{r}_{d,n}) \mathbf{q}_{d,n}^T \tag{4.4}$$

where now G_s is an operator of dimension 1×3 that effectively evaluates the potential by multiplication with the moment of the dipole. Further details on the evaluation of this matrix are provided in the next section. The evaluation can be arranged into a matrix operation as:

$$z = GQ \tag{4.5}$$

where the dipole moments are concatenated into a single vector Q of dimensions $3D \times 1$, and the matrix G has dimension $S \times 3D$. Explicitly:

$$Q = [q_{1x}, q_{1y}, q_{1z}, \ldots, q_{dx}, q_{dy}, q_{dz}, \ldots, q_{Dx}, q_{Dy}, q_{Dz}]^T \tag{4.6}$$

where (q_{dx}, q_{dy}, q_{dz}) are the Cartesian components. The position vectors can be arranged as well into a single object R

$$R = [r_{1x}, r_{1y}, r_{1z}, \ldots, r_{dx}, r_{dy}, r_{dz}, \ldots, r_{Dx}, r_{Dy}, r_{Dz}]^T. \tag{4.7}$$

In bot cases the time index n has been omitted.

In comparing the field associated with a set of dipoles and the actual sensor measurements, it is assumed that the discrepancy $\mathbf{n}$ is a Gaussian random variable. The covariance Σ of this variable can be taken to be diagonal on the sensors, and estimated form measurements in the absence of evoked responses.

$$\mathbf{n}_n = \mathbf{z}_n - \hat{\mathbf{z}}_n \sim \mathcal{N}(0, \Sigma). \tag{4.8}$$

4.3 Calculation of Matrix Elements for the Dipole Model

The relation between the dipoles states and the measured potentials is captured in (4.5). The matrix G implements the model described in section 2.5. For convenience the key results are briefly repeated here. In practice, the matrix elements are evaluated using the EEGLAB package *leadfield*. This function takes as arguments the positions of the dipole and sensors and returns a $S \times 3$ matrix. The concatenation of the D matrices obtained, one for each dipole, form the total matrix G. The matrix elements $G_{s,g}$ with $g = 3(d-1)+1$, $3(d-1)+2$, $3(d-1)+3$ are given by the evaluation of the potential ψ at the sensor locations, given that the dipole position is $\mathbf{r}_d$, and its orientation is along the x, y, z axes respectively for dipole moments aligned with the Cartesian directions and of unit unit magnitude. These three matrix elements are, more explicitly,

$$G_{s,3(d-1)+1} = \psi(\mathbf{r}_s; \mathbf{r}_d, (1,0,0)), \tag{4.9}$$

$$G_{s,3(d-1)+2} = \psi(\mathbf{r}_s; \mathbf{r}_d, (0,1,0)), \tag{4.10}$$

$$G_{s,3(d-1)+1} = \psi(\mathbf{r}_s; \mathbf{r}_d, (0,0,1)). \tag{4.11}$$

In this way, if (q_{xd}, q_{yd}, q_{zd}) are the Cartesian components of the dipole moment, the net contribution to the potential is

$$\psi(\mathbf{r}_s;\mathbf{r}_d,\mathbf{q}_d) = q_{xd}\psi(\mathbf{r}_s;\mathbf{r}_d,(1,0,0)) + q_{yd}\psi(\mathbf{r}_s;\mathbf{r}_d,(0,1,0)) + q_{zd}\psi(\mathbf{r}_s;\mathbf{r}_d,(0,0,1)) \tag{4.12}$$

or

$$\psi(\mathbf{r}_s;\mathbf{r}_d,\mathbf{q}_d) = G_{s,3(d-1)+1}q_{xd} + G_{s,3(d-1)+2}q_{yd} + G_{s,3(d-1)+3}q_{zd}. \tag{4.13}$$

This potential is the d-th term in expression 2.7 written in terms of the matrix elements of G.

The EEGLAB *leadfield* function carries out the calculation of these matrix elements, taking as input the sensor positions $\mathbf{r}_s$ and one dipole position $\mathbf{r}_d$, and returns the $s \times 3$ matrix elements $G_{s,g}$ for all s and $g = 3(d-1)+1,\ 3(d-1)+2,\ 3(d-1)+3$. To start, a three dimensional rotation is carried to a new system of coordinates (x', y', z') so as to make the dipole position coincide with the z-axis and to make the x-component of the moment to only have non-zero x' and z' components (i.e. to lay on the $x' - z'$ plane). The rotation is implemented by a 3×3 matrix $\mathbf{R}_d$.

In the new system of coordinates, the dipole is located at $\mathbf{r}_d^{'} = (0, 0, z_d')$, and the rotation matrix can later be used to obtain the potentials $G_{s,3d+1}$, $G_{s,3d+2}$, and $G_{s,3d+3}$ from the potentials for unit dipoles in the x', y', z' directions. The field for the unit dipole in the y' direction can be obtained from a second rotation once the field for the moment in the x' direction is calculated, so that it is only necessary to consider dipoles in the $x'$and z' directions. These potentials are calculated by first expanding the dipole field at locations $\mathbf{r}'$ into an infinite series truncated to N_t terms. The expressions below do not use the truncation, but this is implicit in the actual evaluation. As the model considers several concentric spheres, the potential has a separate expansion in every region, labeled by the superscript (h) for $h = 1, \ldots, N_r$

where N_r is the number of regions considered. In each region we have an expansion of the form:

$$\psi^{(h)}(\mathbf{r}';\mathbf{r}'_d,\mathbf{q}'_d) \;=\; \frac{1}{4\pi r'^2}\cdot\sum_{n=1}^{n=\infty}\frac{2n+1}{n}\left(\frac{r'_d}{r'}\right)^{n-1}X_n \tag{4.14}$$

with

$$X_n = \left[q'_{zd}n\,A_n^{(h)}P_n(\cos\theta') + q'_{xd}\cos(\phi')B_n^{(h)}P_n^1(\cos\theta')\right] \tag{4.15}$$

where P_n are Legendre polynomials and P_n^m are the associated Legendre polynomials. The sensor location in the rotated frame is given by the spherical coordinates (r',θ',ϕ').

The coefficients are determined from a solution to the $2N_r-2$ equations implementing the boundary conditions (2.5) and (2.6) across the N_r-1 interfaces. The solutions to the equations can be generated using the following relations between the n-th terms of the series (see [21]). The evaluation of the potential uses only the coefficients for the outermost sphere with $(h)=N_r$. These coefficients are:

$$A_n^{(N_r)} = \frac{v_h}{n}B_n^{(N_r)} \tag{4.16}$$

$$B_n^{(N_r)} = \frac{n(2v_h+1)}{(2v_h+1)[v_{N_r}m_{22}+(v_{N_r}+1)m_{21}]}\left(\frac{r'_d}{r'}\right)^{2v_b-n}\left[\prod_{k=1}^{N_r}\left(\frac{R_{k-1}}{R_k}\right)^{v_k}\right] \tag{4.17}$$

$$v_h = [\sqrt{1+4n(n-1)(\zeta_i/\sigma_i)}-1]/2 \tag{4.18}$$

$$\begin{pmatrix} m_{11} & m_{12} \\ m_{21} & m_{22}\end{pmatrix} = \prod_{k=1}^{N_r-1}\frac{1}{2v_k+1}\begin{pmatrix} m_{11}^{(k)} & m_{12}^{(k)} \\ m_{21}^{(k)} & m_{22}^{(k)}\end{pmatrix} \tag{4.19}$$

$$m_{11}^{(k)} = v_{k+1}+(\sigma_k/\sigma_{k+1})(v_k+1) \tag{4.20}$$

$$m_{12}^{(k)} = [(\sigma_k/\sigma_{k+1})(v_k+1) - (v_k+1)](r'/R_k)^{2v_{k+1}+1} \tag{4.21}$$

$$m_{21}^{(k)} = [(\sigma_k/\sigma_{k+1})v - v_{k+1}](R_k/r')^{2v_k+1} \tag{4.22}$$

$$m_{22}^{(k)} = [(v_{k+1}+1) + (\sigma_k/\sigma_{k+1})v_k](r'/R_{k+1})^{2(v_{k+1}-v_k)}. \tag{4.23}$$

In the previous expressions the following definitions and conventions are used. The outermost sphere has maximum radius $R_{N_r} = r'$. The spherical region (h) has inner radius R_{h-1} and outer radius R_h. The coefficients v_k depend on n and must be calculated separately for each n. These expressions use the radial conductivities σ_h and tangential conductivities ζ_h for sphere (h). The relations above are simplified when $\zeta_h = \sigma_h$ as is the case for this manuscript and in the actual evaluation carried out by *leadfield*. The matrix product is carried out placing the highest index matrix first.

Once the coefficients are known up to to some truncated level, the potential is evaluated at all sensor positions for unit vectors $\mathbf{q}'$ and, after rotation to the original frame, these values provide the matrix elements required.

4.4 Estimation of Dipole Moments and Positions

The estimation of dipole positions and moments is carried out using a Rao-Blackwellized approach since, for a fixed set of dipole positions R, the estimation of the moments is a linear problem. The Rao-Blackwellization consists on first estimating the moments and then use particle filtering for the positions.

After updating positions for the filter particles (see below), the moment estimation is done by finding the best fit to the actual sensor recordings. The estimated moments are chosen to minimize the discrepancy between prediction and recordings

$$\hat{Q} = \arg(\min |\mathbf{z}_n - GQ|^2, Q). \tag{4.24}$$

This problem has a know solution based on the pseudoinverse $G^\dagger$of the operator G**:**

$$\hat{Q} = G^\dagger \mathbf{z}_n. \tag{4.25}$$

Substituting this result in the model given by (4.5). After obtaining these values it is possible to write the estimation problem for the positions as:

$$\mathbf{z}_n = G(R)G(R)^\dagger \mathbf{z}_n + \mathbf{n}_n. \tag{4.26}$$

The Gaussian distribution for the errors $\mathbf{n}$ induces a posterior probability distribution $p(R|\mathbf{z}_n)$. The particle filtering method produces an approximation to this distribution as a sum of delta functions as in (3.27).

Most neurological models of evoked potentials assume that the location of the dipoles remain stationary. Therefore, the model used for the update of the positions in the particle filter is simply:

$$R_{n+1} = R_n + \Delta \tag{4.27}$$

where Δ is a random displacement vector of length $3D$ with a Gaussian distribution of zero mean and isotropic covariance. The magnitude of the covariance is a parameter to be chosen during data analysis and simulation.

The initial distribution for the sequential particle filter process is homogeneous inside the brain region. The update of the particle positions is carried out in such a way that new particles are always inside the brain region. In this scheme it is also necessary to address the issue of equivalent points. Not only it is possible to generate nearby points as dipole locations; an unphysical result, but the particle filter might

reach the same set of distinct points and give them different labels. These problems are avoided by ordering the dipole locations according to their distance from the origin and according to their x and y coordinates if necessary. Locations too close to each other or that fall outside the bounds are rejected during the sampling algorithm.

The implementation of the algorithm sketched above requires the computation of the potentials due to sets of dipoles for a large number of different locations. This is the most computationally intensive step in the application of the method. To reduce running time, these potentials are precalculated over a grid and stored. Evaluation at a particular point is then obtained from interpolation over the saved grid values.

4.5 Data Set and Preprocessing

The next sections presents an example of the method described above. The data used is the *Psycophysics* set, which is a commonly used as test case for new methods. The set is part of the EEGLAB libraries [11]. As described in its distribution, a single trial of the experiment consist on the presentation of a visual stimuli to a subject. Five boxes, arranged horizontally, are presented to the subject at once. One of the boxes is of a color different from the rest. The subject is asked to respond to the stimuli by pressing a button. In some of the trials the subject is presented with a circle instead of square and is asked to ignore this instance; that is, to not press the button. The EEG recordings have a fixed length of 3 seconds. The stimuli is presented to the subject at 1 second from the start of the recording. The EEG is sampled on a standard 32 channel setup at a rate of 128 Hz. The data set comprises 80 repetitions of the experiment. As distributed, the data is annotated for the presence of the stimuli and the types of stimuli used.

The data was preprocessed using the methods suggested by the EEGLAB system. The data is low-pass filtered to retain only frequencies lower than 60 Hz, with the goal of eliminating the oscillations due to the instruments alternating current. A linear trend is subtracted from the time series to eliminate the drift on the signals. These are all functions implemented in the user interface of EEGLAB.

For visualization purposes, the potentials can be interpolated to all locations at the surface of the head and displayed in color maps. Snapshots of potential maps for the first trial of the experiment are presented in Figure 4.1.

Two other important preprocessing steps are available for this and other similar sets: averaging and artifact rejection. The first consists simply on creating a single effective experiment from the information available through repetitions. Simply, an

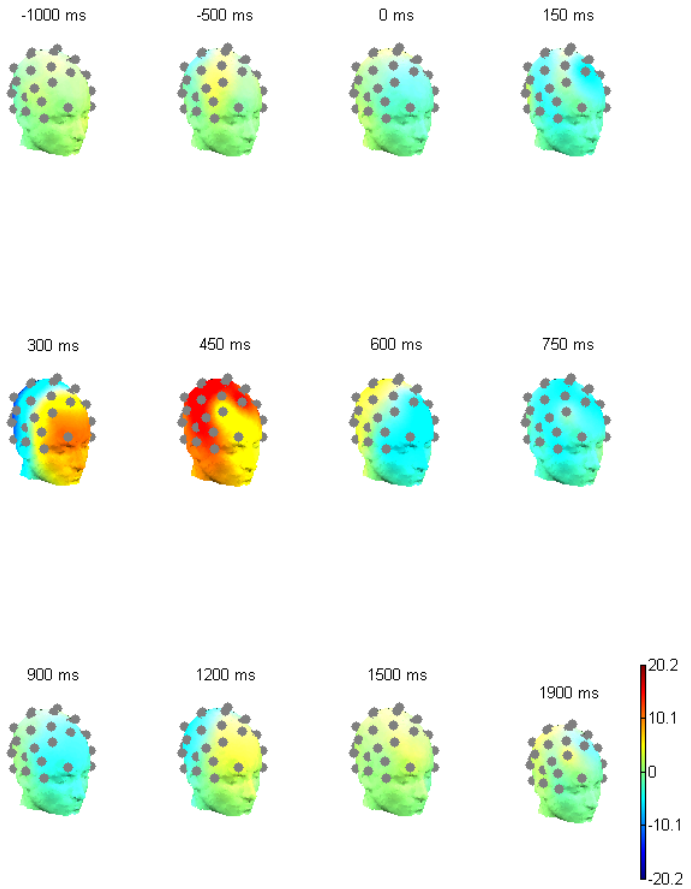

Figure 4.1: EEG potentials snapshots for one trial of the data set employed. The graphs include the location of the sensors. The external stimuli appears at $t = 0$ sec.

effective signal $\bar{z}$ is obtained from average over K experiments:

$$\bar{z}_n = \frac{1}{K} \sum_{k=}^{K} z_n^{(k)}. \tag{4.28}$$

For neatness the average signal will simply be denoted as z where there is no possibility of confusion. This averaging step is justified in that if the goal of the experiment is to detect the aspects common to all response trials, this average should contain a repetition of all key signals generated in the process. As the typical response occurs in an interval of the order of ˜500 *ms,* and it is in general observed that common features have a smooth behavior in this interval, there is little risk to eliminate relevant signals through averaging. Furthermore, this average partially addresses the presence of artifacts such as eye blinking as these are not present in all trials. The averaging reduces their importance even if it does not fully eliminate them. The result of this process is illustrated in Figure 4.2. There the potential for one particular channel (channel 10) is shown as a colored point for each of the trials, while the average is shown at the bottom of as a function of time. The diagram also shows the power spectrum for the average evoked potential.

The second general preprocessing technique is the determination of independent components using the ICA method. These were obtained using the *runica* package of EEGLAB. This algorithm generates a linear transformation of the form

$$v_n^{(k)} = C z_n^{(k)} \tag{4.29}$$

where C is a $S \times S$ square matrix. The s-entries (the rows) in the K instances of the $S\times$N matrix $v_n^{(k)}$ are the so called individual components. The decomposition can be used in two important ways: as a filter and as a dimensional reduction step towards

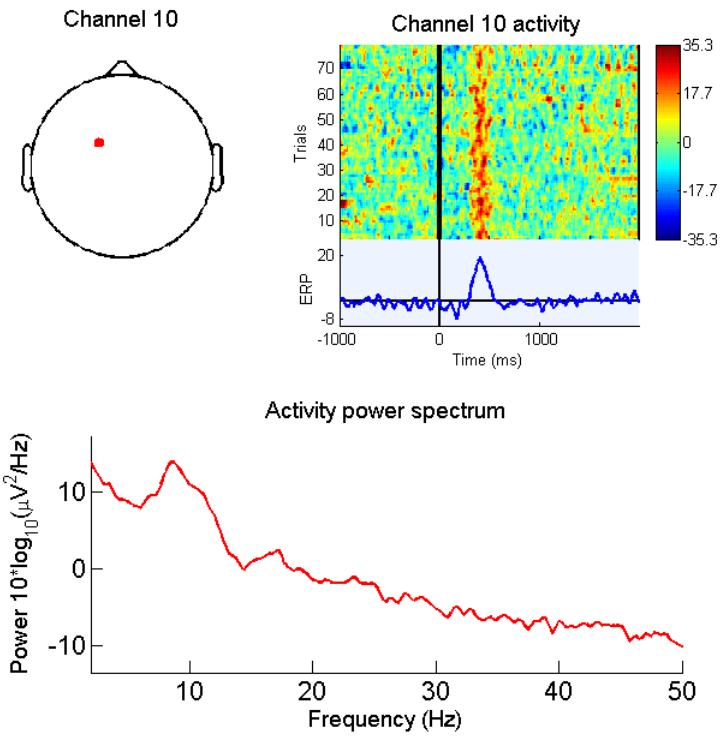

Figure 4.2: Channel properties. The diagram shows the schematic location of the channel on the top left. To the right, the potentials observed in different trials are shown as colored dots. At the bottom of that section the average potential is shown as a function of time. At the bottom, the scheme shows the power spectra for this channel showing the characteristic peak at 10 Hz associated with evoked potentials.

the identification of the source dipoles.

The ICA components can be used as a filter. Each of the components can be classified, for example, as a signal, noise or artifact component. A simple discrimination between the different components can be obtained by their spectral properties and amplitudes. Clearly, is expected the components associated to signals to have the largest amplitudes. In addition, it is empirically found that they tend to exhibit a strong component at around 10 Hz. The components that can be labeled as noise have a monotonically decreasing spectrum and lower amplitudes. Finally, the components associated with artifacts have a sparse time-frequency domain presence. Furthermore, their location in physical space appears most commonly at the sensors

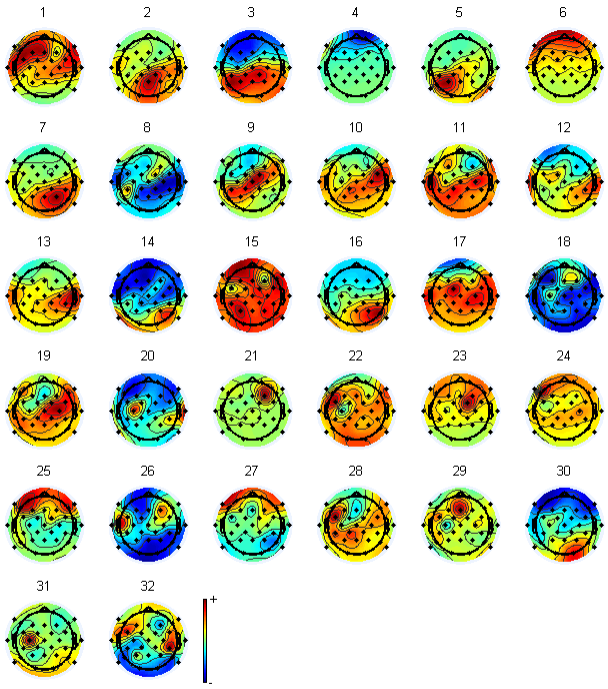

Figure 4.3: Independent components. The scheme shows the interpolated 2D projections of the potential maps of the independent components for the data set. A heuristic interpretation of the components significance indicates, for example, that component 6 corresponds to an eye blinking artifact.

near the eyes or at individual sensors, indicating a physical disconnection.

As an example, Figure 4.3 shows the schematic potential maps for the ICA components for the data set used. Component 6 is identified as an artifact as it is clearly localized in the right eye.

Further, once the ICA components have been obtained, the signal can be projected into these components, and their time-evolution can be assessed. Figure 4.4 the time evolution of the projection onto channel 1. It can be seen to have a strong evoked potential component and it can therefore be classified as an evoked potential contribution, but not as an artifact or a a noise channel. The diagram also shows the

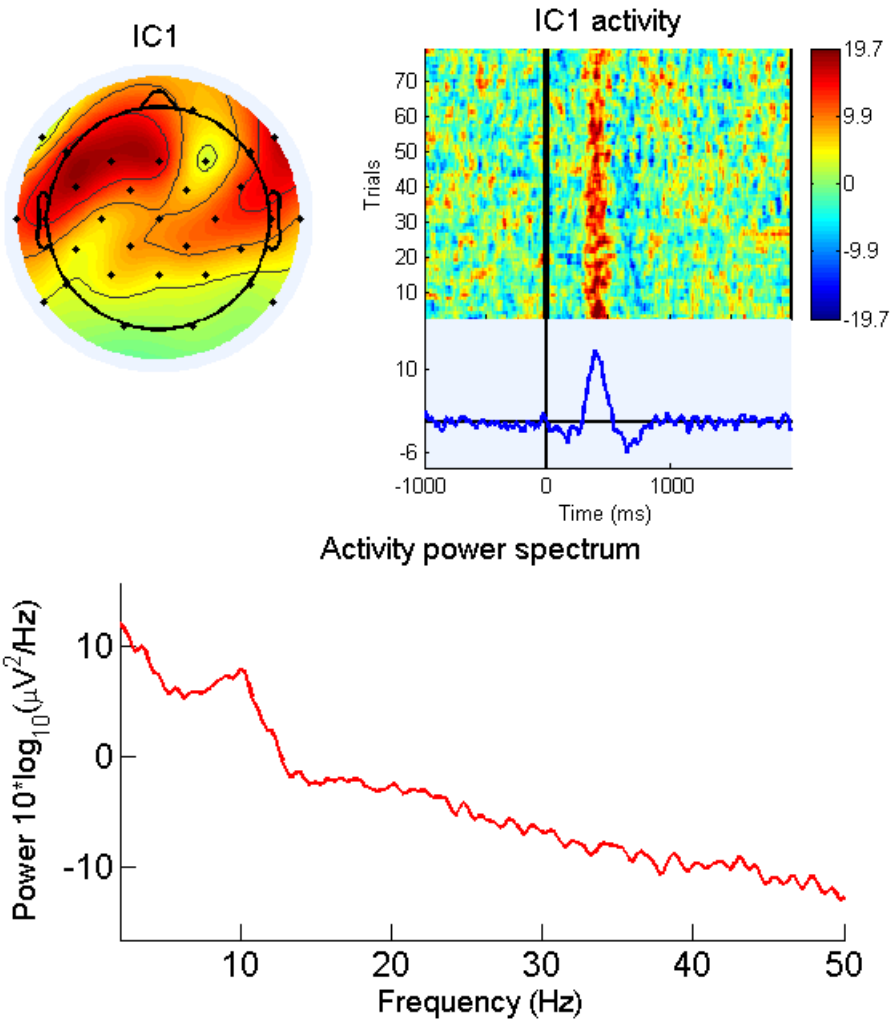

Figure 4.4: Component 1 properties. The diagram repeats the map of the potential and the time run of the projection of the actual data onto the component.

power spectrum for the average evoked potential.

After the components have been labeled as signal, noise or artifacts, a reduced signal can be created by projecting into a desired subspace. As noted below, the projection can be made into individual components, but it can also be carried out to simply select relevant data. For example, if the components are sorted so that the first S_g indices $s = 1, \ldots, S_g$ correspond to signals, then a signal without noise

components s_{sig}, can be reconstructed by projecting onto the subspace spanned by the first $S_g$components. The projector P_{sig} is a unit matrix in the first $S_g$rows and columns and is zero elsewhere. Then:

$$z_{sig} = C^{-1} P_{sig} C z \tag{4.30}$$

is an expression for the signal.

The second use for the ICA is the direct interpretation of each of the components as originating from an individual or a small set of fixed dipoles. In this case, a set of projectors $P^{[i]} = \delta_{ij}$ for $i = 1, \ldots, S_i$ determines the signal component $s^{[i]}$ as

$$z^{[i]} = C^{-1} P^{[i]} C z. \tag{4.31}$$

It is then furthermore assumed that a single or small number of dipoles, say $D^{[i]}$ is responsible for this signal. In addition, the dipole is assumed fixed in space and orientation, so that the best fitting attempts to recover this signal as

$$\hat{z}_{s,n} = \sum_{d=1}^{D^{[i]}} G_s(\mathbf{r}_d) \mathbf{q}_d^T s_{d,n} \tag{4.32}$$

where the matrix G is constructed as above on the assumption that only $D^{[i]}$dipoles are present. The matrix depends on the positions $\mathbf{r}_d$ that are assumed to be constant over time so they do not depend on the index n. Similarly, the vectors $\mathbf{q}_d$ are also independent of the time index and can be normalized to a unit magnitude. Finally $s_n$is allowed to change in magnitude over time modeling the activation of the dipoles. This is the standard approach to use ICA.

In this project, the experimental data is averaged and filtered into the signal subspace but individual dipoles are not fitted.

4.6 Analysis Results

A typical run of the method consists on the fitting of a given number of dipoles. The result is picture of changing dipoles with moving locations. Two measurements (among others) can be used to assess the results. First is the discrepancy between the predicted and the original field $\|\mathbf{z} - \hat{\mathbf{z}}\|$. Second, it is possible to contrast the results against a set of expected behaviors known from previous research: a fix localization for active dipoles, a uniform axis for the dipole and time locking of the external stimuli and the recovered signal. These are discussed in detail below. Additionally, a simple way to obtain a qualitative understanding of the results is to look at the maps of dipole locations presented as movies or a set of time-snapshots, and similarly observe movies or snapshots of the recovered signal and the original signal. A run with $D = 4$ dipoles is discussed in detail here, and a summary for other values is discussed at the end of the section.

The sequence of states produced by the filter is shown in Figure 4.5. The filter initial condition was chosen as a set of random locations for the four dipoles; locations for a single dipole are shown in the same color. At each step 1000 multiparticles were used, with each multiparticle describing the location of each dipole. As can be seen, the particle filter converges rather quickly to a set of clouds, one for each dipole covering a relatively small region. This is observed for the time interval $t < 1$ in the experiment. At times between $1 < t < 2$ it is observed that each cloud further converges into a nearly single point. This is due to the strength of the signal to noise ratio and indicates that the location of the dipoles is well defined in this time frame. In the final time segment it is observed a return to a not so well determined set of positions. It is to be noted that the locations are different in these time segments. In the first and last time intervals the locations correspond to the attempt to model as

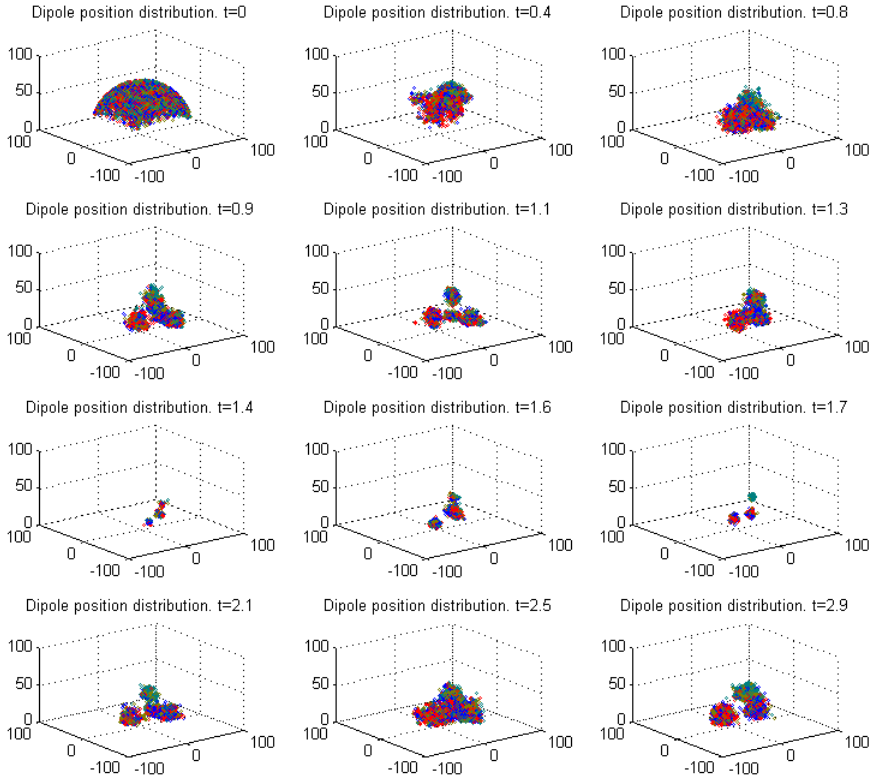

Figure 4.5: Particle filter run for the case of D=4 dipoles. The first 4 frames correspond to the resting brain state and identify plausible locations of high activity. The next 5 frames, between t=1 and t=2 clearly show the convergence to well defined points. The approximation reverts to a less well defined state in the last second, after the effect of the stimulus has mostly vanished.

dipoles the general behavior of the brain in a rest state, which is not considered as a well defined problem from the physiological point of view. Therefore, the most useful information resides in the time interval after the stimulus.

To further emphasize these results, the Figure 4.6, shows the locations of the averages of the clouds as a function of time, for the most relevant time interval, from $< t <$. It is observed that the location is not fixed, but that it remains within a general zone of the brain.

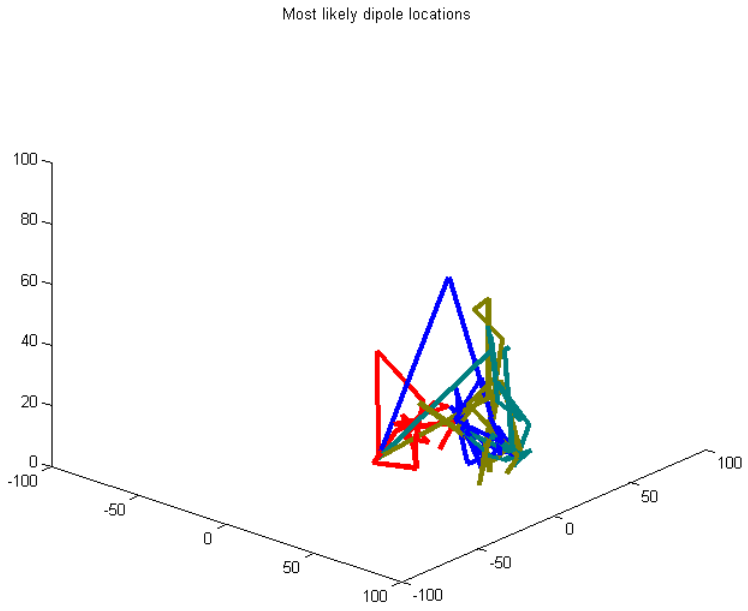

Figure 4.6: Most likely locations for dipoles in for a run in the case of D=4 dipoles. The particles remain localized during the run, but there is a distinct shift to different locations after stimuli. This is observed here in the exploration of positions with higher z coordinate values during the process.

As with the location of the dipoles, their orientations are assumed, from a neurophysiological perspective, to be fixed. The particle filter method does not assume a fixed direction. As a result, the orientations of the dipoles receive a probability distribution. The Figure 4.7 presents a plot of the orientations, as points on a sphere, corresponding to the most likely particles in the ensembles for each time step and each dipole. The size of the points is proportional to the magnitude of the dipole. It is expected that in the time frame where there exists an evoked response, the dipole magnitudes be stronger. The figure shows that the likely orientations of the dipoles are not randomly distributed but do not take a sharply defined direction either. Additionally, it is to be noted that during this period the potential is known to invert in direction and the dipole should change to an antipodal orientation. Thus, a distri-

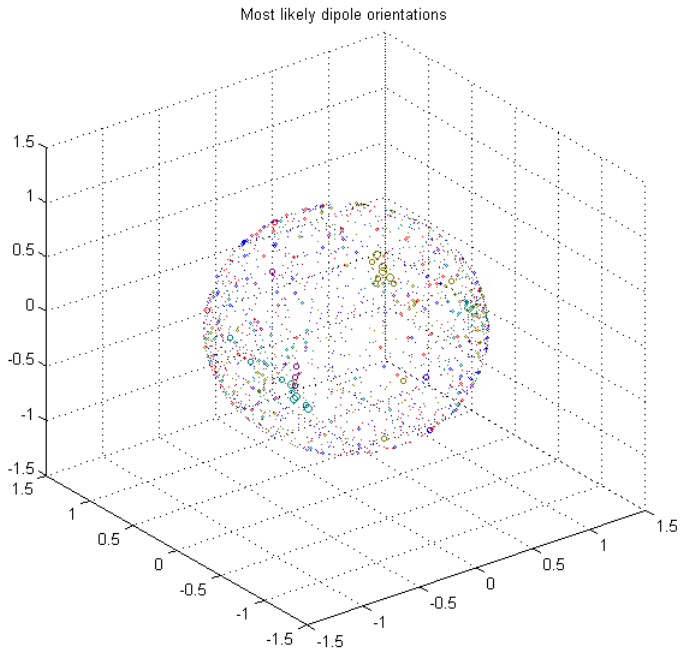

Figure 4.7: Most likely orientations for dipoles for a run in the case of D=4 dipoles. Each point lies at the surface of the unit sphere and indicates a direction in space. The size of the points is proportional to the magnitude of the dipoles. The orientations are not distributed randomly but do not present sharp localization.

bution conforming with the expectation of fixed directions would have two peaks at antipodal positions.

To discern the role of the different dipoles, it is convenient to establish their contributions to the total field. The Figure 4.8 shows the amplitude of the different dipoles, and the ratio of the dipole amplitude to the mean square sum of all the amplitudes taken at the same time. The bottom frames of the figure show the same plots but within a restricted time frame. This region corresponds to the time location of the main evoked potential. It can be seen that when the response requires the maximum amplitudes of the dipoles, there are two that contribute the largest amount to the total field. This indicates that the evoked potential is predominantly generated

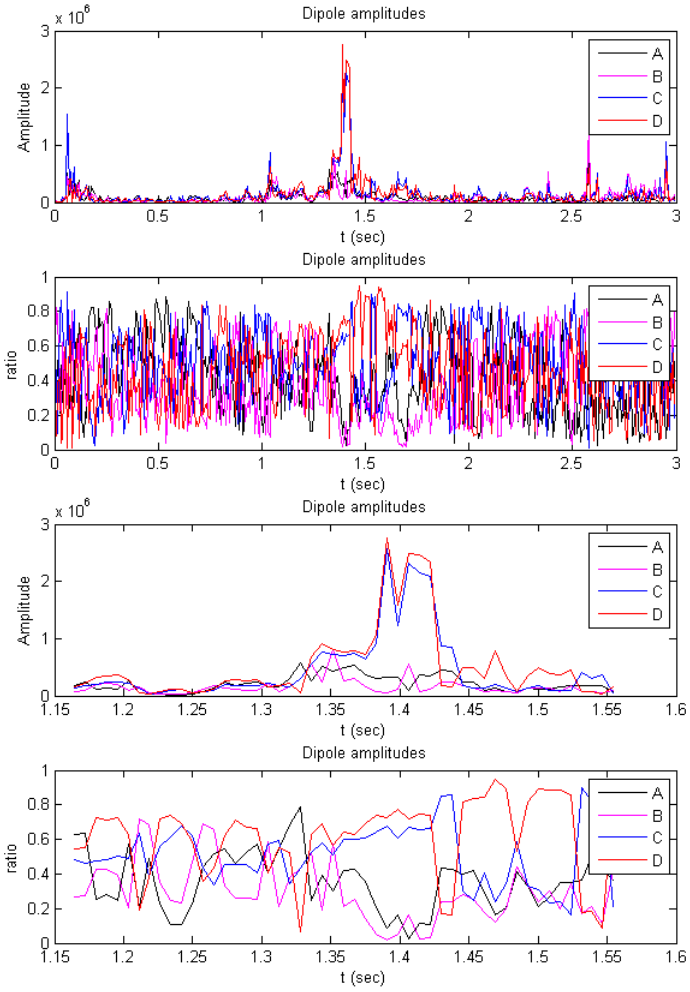

Figure 4.8: Magnitudes of dipoles and their relative sizes. In the bottom panels, the same top plots are repeated for a shorter time interval that corresponds to the presence of the evoked potential.

at two locations. As shown below, the use of more dipoles do improve the recovery of the total field but it is likely that the the dominant response originates from these two locations.

The measured potentials at the electrodes and the potentials obtained from the dipoles are shown in Figure 4.9 for selected times around the maximum of the evoked potential for a run with $D = 4$. The scale used in all plots is the same. It can be seen

that the recovered potential has a clear resemblance to the original recordings.

To quantify the extent to which the selected dipoles reproduce the total field, the difference $\|z - \hat{z}\|$ between the original field and the estimation can be calculated. To normalize it, this quantity is compared to the maximum value of the signal. Other measures can be used, but this is a reasonable choice as the signal magnitude peaks in the region of interest (the times at which an evoked potential appears). Plots of this ratio for an instance of simulation appear in Figure 4.10. There, it can be seen that increasing the number of dipoles improves the prediction and reduces the discrepancy. A large change can be seen in going from 3 to to 4 dipoles.

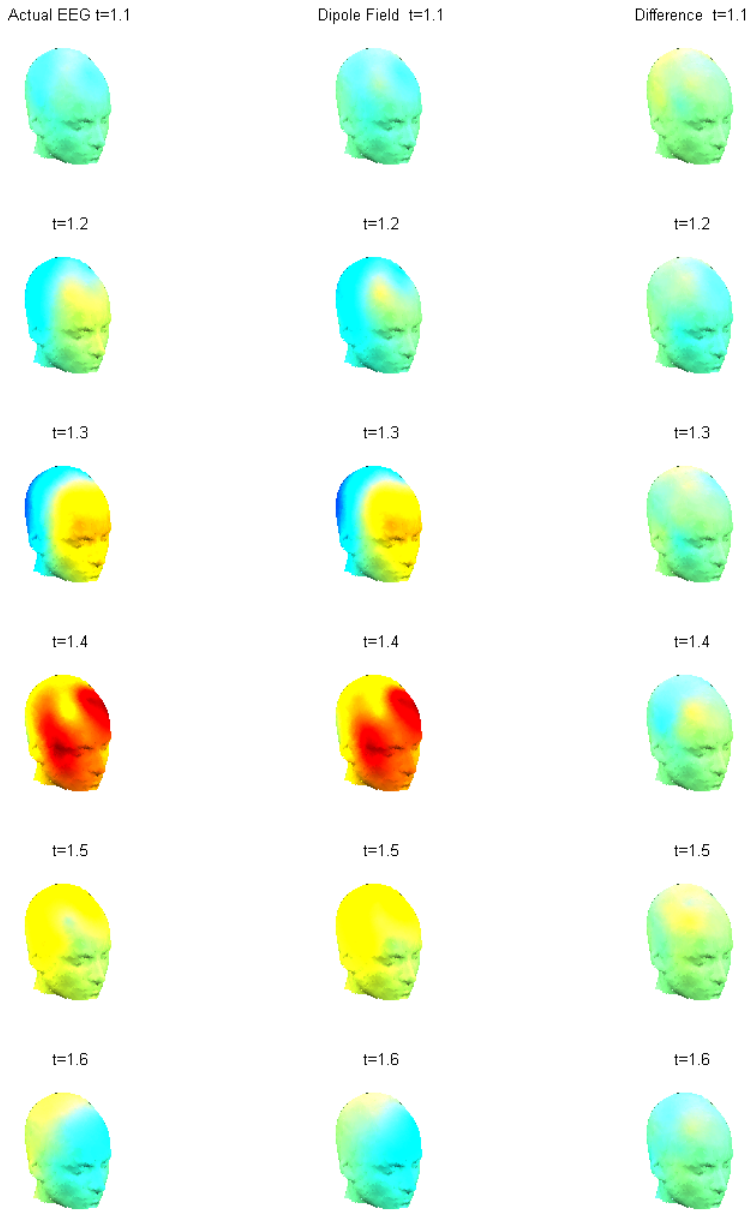

Figure 4.9: Color maps of the actual measured potentials, the recovered dipole field (D=4) and the difference between these for different times around the maximum evoked potential activity. The stimulus occurs at $t = 1$.

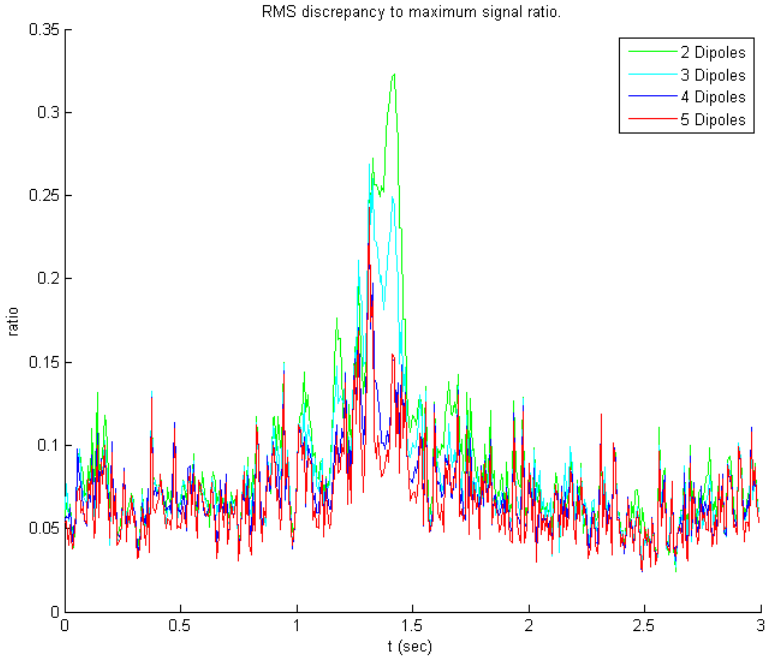

Figure 4.10: Plots of the ratio of the RMS of the discrepancy between recovered and original signal to the peak value of the signal. The four graphs correspond to simulations with different number of dipoles, D=2,3,4,5 as indicated in the legend.

Chapter 5

CHARGE AND POWER IN EEG MODELS

This chapter introduces a more detailed description of the electric processes in the brain using the physical variables of charge and power. These are particularly useful when considering models with realistic heads.

5.1 Inverse Problem

The EEG inverse problem is the process of determining, given a set of EEG recordings, sources associated with brain activity. Various methods have been developed to solve the inverse problem [8, 59–61], including Bayesian filtering that uses simulations to estimate the source probability distribution [62–64]. These methods require knowledge of the scalp potential created by known neural sources provided by the forward solution [16, 60, 65]. Construction of this solution is usually obtained by solving the Geselowitz integral equation (GIE) [23] or its related symmetric formulation [66]. These are integral equations for the electric potential at boundaries between homogeneous conductive regions. Software packages are now publicly available that implement methods to solve the inverse problem using forward solutions; these include EEGLAB [11] based on the isolated problem approach [67–69], and OpenMEEG [12] based on the symmetric formulation [66]. There are important connections between

a number of important GIE properties and two physical variables: *surface charge and passive dissipated power*. The surface charge is the charge that accumulates at the interfaces between contiguous head regions of homogeneous conductivity. The passive power dissipation results from the conductive currents that appear in the re-

gions of homogeneous conductivity. Although these variables appear naturally in the GIE, their relation to EEG has not been previously demonstrated, to the best of our knowledge. Both of these variables are important as they provide opportunities for the simultaneous use of EEG methods along with other techniques. In particular, we note that important physiological facts as well as basic assumptions in the GIE model can be described in terms of the surface charge. For example, careful analysis of conductivity in physiological tissues is associated with ionic concentrations in the extracellular fluid [70]. Discussion of non-transient phenomena that determine the time scales over which EEG models are valid also requires consideration of the ionic redistribution that occurs within cells and neurons [15]. At a more applied level, it can be noted that many neurological processes are associated with ion exchange [71], and that the changes in the local ionic composition can be experimentally assessed, for example, by optical spectroscopy [72, 73]. The use of accumulated charge and the related concept of polarization surface charge has been used in the description of biophysical structures [74], dielectric interfaces [75] and geophysical phenomena [76] to name a few. The passive dissipated power is important in impedance tomography [77], where determination of the conductivity values in a region (the Calderon problem [78]) can be shown to be extrema of a power dissipation functional. Note that there have already been simultaneous measurements of conductivity and EEG signals [79].

We provide a solution to the EEG forward problem using integral equations based on the surface charge accumulated at the boundaries between homogeneous regions [65, 80]. This surface charge method (SCM) has been used in other bioelectric problems such as the study of external electrical stimuli [74, 81]. Using variational bounds, the passive power dissipation is used to derive a number of features of the eigenvalue structure of the kernels that appear in the SCM and GIE integral operators. The

structure provided by the power dissipation also allows the identification of the relation between the GIE and SCM; their key operators are shown to be adjoint and therefore have an identical eigenvalue structure. From these results, it is possible to identify a critical eigenvalue and associated eigenspace that makes the relevant operators non-invertible. The results obtained by considering the roles of charge and power dissipation can be used to construct alternative methods for solving the forward problem. We demonstrate this by formulating a projection method for the SCM and GIE solution. The equations satisfied by the model are singular and require regularization that is achieved using the isolated problem approach or deflation [61, 82]. The projection method we describe eliminates a region of singular or near-singular eigenvalues to regularize the operators.

5.2 Surface Charge Method

In the Geselowitz model, the head is considered to be composed of a number of homogeneous linear conductive regions. The currents in these regions can be described by a steady quasi-static current density $\mathbf{J}(\mathbf{x})$, where $\mathbf{x}$ is a three-dimensional position vector. There are two components to the current density: the conductive or passive current $\mathbf{J}_c(\mathbf{x})$ and the forced current $\mathbf{J}_f(\mathbf{x})$. The forced currents arise from localized neural activity where, by electrochemical processes, a large number of neurons coherently transfer charge in a particular direction. A mesoscopic average of these processes can be described as a set of forced current dipoles. A current dipole is a localized current in a particular direction.

After the onset of forced currents on a region, the charge transfer produces a charge accumulation during its transient period. This charge accumulation produce electric fields $\mathbf{E}(\mathbf{x})$, that in turn produce the conduction currents $\mathbf{J}_c(\mathbf{x}) = \sigma\mathbf{E}(\mathbf{x})$ given the

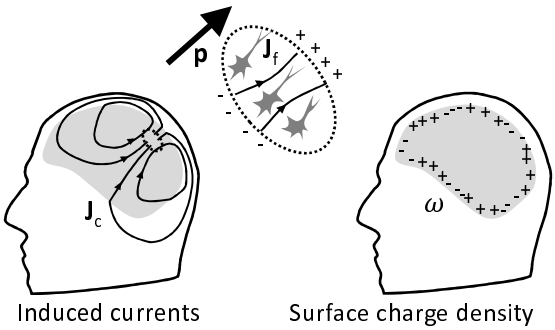

Figure 5.1: Coherent neural activity creates a forced current density $\mathbf{J}_f$ and an associated charge accumulation described by a dipole $\mathbf{p}$ (center top). The electric field due to the dipole induces a conductive current $\mathbf{J}_c$ (left). Due to this current, a surface charge density (SCD) ω (right) appears at the boundary between regions of different conductivity (grey and white regions).

assumed linear behavior of the conductive regions. The conductivity σ is considered constant throughout the physiologically different regions of the head. It is also assumed that the forced currents change over time scales much larger than the relaxation times of the mobile ion distributions. The currents, electric fields and potentials are then quasi-static. The continuity equation satisfied by the total current can be written as $\partial_t \rho_m(\mathbf{x}) + \nabla_x \cdot \mathbf{J}(\mathbf{x}) = 0$, where ρ_m is the density of mobile charges and $\nabla_x \cdot \mathbf{J}(\mathbf{x})$ computes the current divergence. In the quasi-static case, the time derivative can be set to zero, resulting in $\nabla_x \cdot \mathbf{J}(\mathbf{x}) = 0$. This yields the divergenceless of the total current and to $\nabla_x \cdot (\mathbf{J}_f(\mathbf{x}) + \sigma \mathbf{E}(\mathbf{x})) = 0$. From the quasi-static assumption, $\mathbf{E}(\mathbf{x}) = -\nabla_x \phi(\mathbf{x})$, where $\nabla_x \phi(\mathbf{x})$ computes the gradient of the electric potential $\phi(\mathbf{x})$ with respect to $\mathbf{x}$. Combining with Gauss' law results in $\nabla_x \cdot \mathbf{E}(\mathbf{x}) = \rho(\mathbf{x})/\varepsilon_0$, where $\rho(\mathbf{x})$ is the net total charge density and ε_0 is the vacuum permittivity. The divergence of the forced current can then be evaluated in a region where it is not zero and away from regions of discontinuity of the conductivity. This results in $\nabla_x \cdot \mathbf{J}_f(\mathbf{x}) = -\sigma \rho_s(\mathbf{x})/\varepsilon_0$, where the source charge density $\rho_s(\mathbf{x})$ is due only to the forced current. For a single dipolar source, $\rho_s(\mathbf{x}) = -\mathbf{p} \cdot \nabla_x \delta(\mathbf{x} - \mathbf{x}_s)$, with $\mathbf{p}$ the effective dipole vector. The partial

differential equation that describes the system has then the form:

$$\nabla \cdot (\sigma \mathbf{E}) = \sigma \rho_s(\mathbf{x})/\varepsilon_0. \tag{5.1}$$

5.3 Charge Accumulation at Region Interfaces

Net charges are found at the boundaries between regions of constant conductivity. These boundaries separate regions with homogeneous properties. These boundaries are interchangeably called interfaces or surfaces in the paper. We assume that the head model has N_r+1 distinct regions R_i, $i=0,1,\ldots,N_r$, with respective conductivities σ_i. The regions are assumed concentric so that the ith interface, S_i, $i=1,\ldots,N_r$, is defined as the boundary between regions R_{i-1} and R_i. The assumption simplifies exposition and numerical work, though is not indispensable. The interfaces are assumed to be smooth so that a normal unit vector, $\mathbf{n}(\mathbf{x})$, is well-defined at all points. At an interface, the continuity of the potential makes the tangential component of the electric field continuous. However, the normal component of the electric field can be discontinuous. A point in the S_i interface can be reached from within the R_{i-1} and R_i regions. The limiting values of the field in each case are denoted as $\mathbf{E}_{i-1}$ and $\mathbf{E}_i$ respectively. We use a similar notation for the current density $\mathbf{J}$ as well. The divergenceless condition for the current implies continuity of its normal component at interfaces, $\mathbf{J}_{i-1}(\mathbf{x})\cdot\mathbf{n}(\mathbf{x}) = \mathbf{J}_i(\mathbf{x})\cdot\mathbf{n}(\mathbf{x})$; the tangential components need not be continuous. Therefore, the limit values of the electric field at an interface satisfy $\sigma_{i-1}\mathbf{E}_{i-1}(\mathbf{x})\cdot\mathbf{n}(\mathbf{x}) = \sigma_i\mathbf{E}_i(\mathbf{x})\cdot\mathbf{n}(\mathbf{x})$.

The discontinuity of the electric field at the interface results in a net surface change density (SCD) $\omega(\mathbf{x})$. Physically, this charge has two sources: the accumulation of mobile ions at the interfaces during the transient period and the net mismatch in the

dielectric polarization of two neighbouring regions. Note that the quasi-static condition implies that this charge accumulation must only occur at the interfaces or at the source location. Physically, the interface has a finite thickness and a relatively complex structure, but at the mesoscopic level, it can be modeled as a charged, infinitely thin surface. With this approximation, the electric field is assumed discontinuous but with a well defined value at the interface. Figure 5.1 illustrates some of the variables described above.

In order to derive the interface condition for normal components of the electric field, we use a standard pillbox construction. A small disk and its surface charge are excluded from the surface; its contribution to the field is considered separately. The construction produces a field that is zero at the center of the disk and that, for positive charges, points away from the disk. Near the disk center, the outward component of the field has magnitude $\omega(\mathbf{x})/(2\,\varepsilon_0)$. The field due to all other charges in the system at the center of the disk is $\mathbf{E}(\mathbf{x})$ and is not modified by the charge in the disk. As a result, the field value $\mathbf{E}(\mathbf{x})$ at a point $\mathbf{x}$ in interface S_i, and the limiting values $\mathbf{E}_{i-1}(\mathbf{x})$ and $\mathbf{E}_i(\mathbf{x})$ at the same location satisfy

$$\begin{aligned} \mathbf{E}_{i-1}(\mathbf{x}) &= \mathbf{E}(\mathbf{x}) + \frac{\omega(\mathbf{x})}{2\,\varepsilon_0}\mathbf{n}(\mathbf{x}) \\ \mathbf{E}_i(\mathbf{x}) &= \mathbf{E}(\mathbf{x}) - \frac{\omega(\mathbf{x})}{2\,\varepsilon_0}\mathbf{n}(\mathbf{x})\,, \end{aligned} \tag{5.2}$$

where the normal at the interface is chosen to point into region R_{i-1} and away from region R_i. Using these expressions and the continuity equation, the SCD can be written in terms of the field at interface S_i as

$$\omega(\mathbf{x}) = -\varepsilon_0\, s_i\, \mathbf{E}(\mathbf{x})\cdot\mathbf{n}(\mathbf{x}), \tag{5.3}$$

where $s_i = \Delta\sigma_i/\bar{\sigma}_i = 2(\sigma_{i-1} - \sigma_i)/(\sigma_{i-1} + \sigma_i)$. Here, the mean conductivity at the interface is $\bar{\sigma}_i = (\sigma_{i-1} + \sigma_i)/2$ while the conductivity difference is $\Delta\sigma_i = \sigma_{i-1} - \sigma_i$.

Expression (5.3) has been used in the description of bioelectric systems [74]. Similar relations are implicit in other formulations of the EEG problem [66].

To obtain a complete set of SCD equations, we must calculate the electric field in terms of the charges and source distributions. For this purpose, we use the geometric Green's function $G(\mathbf{x},\mathbf{y}) = (4\pi)^{-1}|\mathbf{y}-\mathbf{x}|^{-1}$ that solves the Poisson equation in free space: $\nabla_x \cdot \nabla_x G(\mathbf{x},\mathbf{y}) = -\delta^3(\mathbf{x}-\mathbf{y})$. The resulting electric potential ϕ can then be written as

$$\phi(\mathbf{x}) = \frac{1}{\varepsilon_0}\int_A G(\mathbf{x},\mathbf{y})\,\omega(\mathbf{y})\,dA_{\mathbf{y}} + \frac{1}{\varepsilon_0}\int_V G(\mathbf{x},\mathbf{y})\rho_s(\mathbf{y})\,dV_{\mathbf{y}}\,. \tag{5.4}$$

Here, the area integral A is over all interfaces, with area differential $dA_{\mathbf{y}}$ associated with position $\mathbf{y}$, while the volume integral V is over the whole space, with volume differential $dV_{\mathbf{y}}$. This representation assumes that the potential goes to a zero reference value at points infinitely far from the head. From the potential, the electric field is determined by $\mathbf{E}(\mathbf{x}) = -\nabla_x \phi(\mathbf{x})$.

5.4 Surface Charge Integral Equation

Combining (5.3) and (5.4) we obtain the surface charge method (SCM) integral equation for the SCD:

$$\omega(\mathbf{x}) = \int_A s(\mathbf{x})\,\mathbf{n}(\mathbf{x})\cdot\nabla_x G(\mathbf{x},\mathbf{y})\,\omega(\mathbf{y})\,dA_{\mathbf{y}} + \int_V s(\mathbf{x})\,\mathbf{n}(\mathbf{x})\cdot\nabla_x G(\mathbf{x},\mathbf{y})\,\rho_s(\mathbf{y})\,dV_{\mathbf{y}}\,. \tag{5.5}$$

Here, the position $\mathbf{x}$ is assumed to be at one of the interfaces S_i so that the the conductivity ratio can also be written as $s(\mathbf{x}) = s_i$. To simplify notation, (5.5) can be rewritten as

$$\omega = \mathcal{B}\,\omega + \mathcal{C}\,\rho_s. \tag{5.6}$$

where operator $\mathcal{C}$ acts on the volumetric charge distribution ρ_s to yield a contribution to the SCD defined only at the interfaces. Operator $\mathcal{B}$ maps an SCD onto a new SCD. The SCDs ω and $\mathcal{C}\rho_s$ can be considered as vectors in a space of functions defined at the surfaces. Then, $\mathcal{B}$ is a linear operator acting in this space. Its integral kernel is $B(\mathbf{x},\mathbf{y}) = s(\mathbf{x})\mathbf{n}(\mathbf{x})\,\bar{\sigma}(\mathbf{x})\cdot\nabla_x G(\mathbf{x},\mathbf{y})$.

The formal solution of (5.6) is

$$\omega(\mathbf{x}) = (\mathcal{I}-\mathcal{B})^{-1}\mathcal{C}\rho_s(\mathbf{x}) \tag{5.7}$$

where $\mathcal{I}$ is the identity operator in the space of functions defined on the surfaces between homogenous regions. This solution requires the operator $(\mathcal{I}-\mathcal{B})$ to be invertible. After the SCD is obtained, the potential is calculated using (5.4) or in operator form as, $\phi(\mathbf{x}) = \mathcal{G}_c\omega(\mathbf{x}) + \mathcal{G}_s\rho_s(\mathbf{x})$. The integral operators $\mathcal{G}_c$ and $\mathcal{G}_s$ are defined by the kernels in (5.4) and act on the surface and volume charge distributions, respectively.

For reference, the GIE is given by

$$\begin{aligned}\bar{\sigma}(\mathbf{x})\phi(\mathbf{x}) &= \int_A \nabla_y G(\mathbf{x},\mathbf{y})\cdot\mathbf{n}(\mathbf{y})\, s(\mathbf{y})\,\bar{\sigma}(\mathbf{y})\phi(\mathbf{y})\,dA_{\mathbf{y}} \\ &\quad + \int_V \nabla_y G(\mathbf{x},\mathbf{y})\cdot\mathbf{J}_f(\mathbf{y})\,dV_{\mathbf{y}}\,.\end{aligned} \tag{5.8}$$

In the first integral, the normal, the discontinuity $\Delta\sigma$, and the potential are evaluated at points $\mathbf{y}$ in the interfaces S_i. This is in contrast to the SCM integral equation in (5.5) where the normal and the conductivity ratio are evaluated at the observation point. The position $\mathbf{x}$ is arbitrary but should be taken at one of the interfaces to obtain a closed boundary integral equation. The GIE can also be written in operator form using as key variable the product of the average conductivity and the potential $\bar{\sigma}\phi$ at different locations of the system interfaces. The equation reads

$$\bar{\sigma}\phi = \mathcal{B}'\bar{\sigma}\phi + \mathcal{C}'\rho_s\,. \tag{5.9}$$

The integral kernel for of the operators in (5.9) can be obtained from the explicit expressions in (5.8). For $\mathcal{B}'$, this is given by $B'(\mathbf{x},\mathbf{y}) = s(\mathbf{y})\bar{\sigma}(\mathbf{y})\mathbf{n}(\mathbf{y})\cdot\nabla_y G(\mathbf{x},\mathbf{y})$. Comparing the integral kernels of the SCM and GIE, and using the symmetry of the Green's function we see that $B'(\mathbf{x},\mathbf{y}) = B'(\mathbf{y},\mathbf{x})$ and conclude that the operators $\mathcal{B}$ and $\mathcal{B}'$ are transpose to each other.

5.5 Eigenvalues of the SCM Charge Interaction Operator

We use eigenanalysis of the linear operators in (5.6) or (5.7) to analyze the properties of the SCM abstract solution. A number of results can be derived by considering the dissipated power as a variational functional [83]. In addition, power dissipation has independent and intrinsic significance as a physical variable. The key result of this analysis is that the operator $\mathcal{B}$ has real bounded eigenvalues that satisfy $\lambda \leq 1$. The largest eigenvalue of $\mathcal{B}$ and its corresponding eigenfunction are interpreted as the addition of a net charge to the surface of the head. Note that some previous results on eigenvalue structure were first obtained in the development of deflation methods [61, 82].

The solution to the SCM equation (5.7) is based on the use of the $\mathcal{B}$ integral operator. We refer to this operator as the charge interaction operator as it describes the charge accumulation at interfaces due to the fields created by these same charges. The operator $\mathcal{B}'$ in (5.9) serves a similar purpose for the GIE. We first consider the case of the operator $\mathcal{B}$ for the SCM solution, and then we extend the results to $\mathcal{B}'$ for the GIE solution.

The starting point of the analysis is to note that, as the conductivity is always positive, the product $\mathbf{E}(\mathbf{x})\cdot\mathbf{J}_c(\mathbf{x}) = \sigma(\mathbf{x})\mathbf{E}(\mathbf{x})\cdot\mathbf{E}$ is positive everywhere. This product can be interpreted as the rate of power dissipation per unit time per unit volume.

Integration over all space gives the net power dissipation rate P of the system as

$$P = \int_V \mathbf{E}(\mathbf{x}) \cdot \mathbf{J}_c(\mathbf{x})\, dV_{\mathbf{x}} \geq 0\,.$$

We consider the case where the fields are created by an SCD $\omega(\mathbf{x})$, and when there are no forced current sources. The SCD is arbitrary and not necessarily an SCM solution. The electric potential created by this distribution is

$$\phi(\mathbf{x}) = \frac{1}{\varepsilon_0} \int_A G(\mathbf{x}, \mathbf{y})\, \omega(\mathbf{y})\, dA_{\mathbf{y}}\,.$$

The expression for the power can be written in terms of the potentials created by the given densities as

$$\begin{aligned} P &= \int_V \Big[-\nabla_x \phi(\mathbf{x}) \Big]\, \sigma(\mathbf{x}) \Big[-\nabla_x \phi(\mathbf{x}) \Big]\, dV_{\mathbf{x}} \\ &= \int_V \phi(\mathbf{x}) \Big[-\nabla_x \cdot \sigma(\mathbf{x})\, \nabla_x \phi(\mathbf{x}) \Big]\, dV_{\mathbf{x}}\,. \end{aligned}$$

The term in square brackets can be put in the form $-\nabla \cdot (\,\sigma\, \nabla\phi) = -\sigma \nabla^2 \phi - \nabla(\phi \cdot \nabla\sigma)$, where we omit the position $\mathbf{x}$. The first term is simplified noticing that it has contributions only at the interfaces, where charge accumulation appears: $\nabla^2 \phi = -(\omega/\varepsilon_0)\delta(t)$. This expression uses a local coordinate systems where $t = 0$ singles out the location of the interface. Both ω and σ must be evaluated at interface points. There, the conductivity is averaged over the two neighboring homogeneous regions so that this term gives $\bar{\sigma}\omega\delta(t)$. The second term is $-\nabla\phi \cdot \nabla\sigma$. The gradient of the conductivity is a vector in the direction normal to the interface, localized there as a delta function, times a factor $\Delta\sigma = \bar{\sigma} s$. The whole term reads $-\bar{\sigma} s \mathbf{n} \cdot \nabla\phi\delta(t)$. Integrating over the volume reduces the expression to an integral over the interfaces. The factor $\bar{\sigma}$ is factorized and we have:

$$P = \int_A \bar{\sigma}(\mathbf{x}) \phi(\mathbf{x}) \Big[\varepsilon_0^{-1} \omega(\mathbf{x}) - s\mathbf{n}(\mathbf{x}) \cdot\, \nabla_x \phi(\mathbf{x}) \Big]\, dA_{\mathbf{x}}\,.$$

The potential in the last term of the integrand is expressed as an integral over the SCD and we obtain

$$P = \int_A \frac{1}{\varepsilon_0} \bar{\sigma}\, \phi(\mathbf{x}) \Bigg[\omega(\mathbf{x}) - s\mathbf{n}(\mathbf{x}) \cdot \left(\int_A \nabla_x G(\mathbf{x}, \mathbf{y})\, \omega(\mathbf{y}) dA_{\mathbf{y}} \right) \Bigg] dA_{\mathbf{x}}\,, \tag{5.10}$$

where the second term can be identified as the action of the charge interaction operator $\mathcal{B}$ on the SCD $\omega(\mathbf{x})$.

We can now choose the SCD to be an eigenvector of the charge interaction operator, $\mathcal{B}\,\omega_\lambda(\mathbf{x}) = \lambda\,\omega_\lambda(\mathbf{x})$, resulting in

$$P = \int_A \frac{1}{\varepsilon_0} \Big[\bar{\sigma}\, \phi(\mathbf{x})\, (1 - \lambda)\, \omega_\lambda(\mathbf{x}) \Big] dA_{\mathbf{x}}\,.$$

If we explicitly write the potential in terms of the SCD, then the non-negativity of the power implies the following relation

$$\frac{1}{\varepsilon_0}(1 - \lambda) \left[\int_A \int_A \omega_\lambda(\mathbf{y})\, G(\mathbf{x}, \mathbf{y}) \bar{\sigma}\, \omega_\lambda(\mathbf{x})\, dA_{\mathbf{x}}\, dA_{\mathbf{y}} \right] \geq 0\,. \tag{5.11}$$

Note that the double integral within the square brackets in (5.11) is also non-negative. This follows from the positivity of the two operators involved: the one defined by the multiplication by the mean conductivity and the one defined by Green's function. This implies that the operator $\mathcal{B}$ is positive and thus have real eigenvalues. Furthermore, we have $(1 - \lambda)/\varepsilon_0 \geq 0$ in (5.11), and thus all eigenvalues of the $\mathcal{B}$ operator must satisfy

$$\lambda \leq 1\,.$$

This result is of great importance, as crucial aspects of the problem arise from the behavior near the critical value $\lambda = 1$.

The eigenvalue analysis also yields a result for the lowest eigenvalue. For this one notes that the power dissipation is bounded above by the value calculated using the

largest conductivity in the system σ_{max}. We have $(\sigma_{max} - \sigma)\mathbf{E} \cdot \mathbf{E} \geq 0$. Integrating this expression over all space, and following essentially the same steps as above for P we obtain an expression similar to (5.11) but with a factor, inside the integral, of the form $(\sigma_{max}/\bar{\sigma}) - 1 + \lambda$, instead of $1 - \lambda$. Using again the properties of positive operators, we determine the bound $\lambda \geq 1 - (\sigma_{max}/\bar{\sigma}_{min})$ where $\bar{\sigma}_{min}$ is the minimum value of the mean conductivity, which is always non-zero.

Finally, we note that as the operator $\mathcal{B}'$ in the Geselowitz formulation, (5.9), is the transpose of the SCM operator, their eigenvalue system is the same and discussion of the properties of one can be directly applied to the other.

5.6 Interpretation of the Maximum Eigenvalue

The maximum eigenvalue $\lambda_{\max} = 1$ and its eigenvector have a clear interpretation. In the model used, the head is surrounded by a non-conductive medium (air), and the outermost interface has a conductivity contrast factor of $s = 2(\sigma_{\text{out}} - \sigma_{\text{in}})/(\sigma_{\text{in}} + \sigma_{\text{out}}) = -2$. A solution to the potential equations can be constructed such that the electric field inside the conductive region is zero. Then, the potential inside the region must be constant, as depicted in Figure 5.2 on for the potential satisfies the Laplace equation with a constant potential boundary condition at the interface. Such a solution always exists. The field is discontinuous at the outmost interface with a non-zero charge distribution $\omega_1(\mathbf{x})$. At points just inside this surface, the total field is zero; this is due to the cancellation of the field in the small disk around a given point in the surface and the field due to all other charges. That is, we can use (5.2) with the field at one of the interfaces set to zero and the field $\mathbf{E}(\mathbf{x})$ set to the value at the surface. Therefore, we identify the necessary charge in terms of the field to be $\omega_1(\mathbf{x}) = -2\,\varepsilon_0\,\mathbf{n}(\mathbf{x}) \cdot \mathbf{E}(\mathbf{x})$. This field can be calculated by summing all the

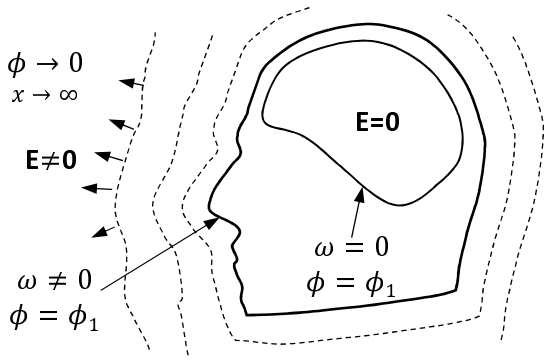

Figure 5.2: Solution to the SCM and GIE equations for eigenvalues $\lambda = 1$ and $\lambda' = 1$. Inside the head, all interfaces have zero charge density and the potential is constant. In the air, the field decays to the zero reference value at infinity.

contributions due to this same charge distribution so that

$$\omega_1(\mathbf{x}) = 2\,\mathbf{n}(\mathbf{x})\cdot\nabla_x \int_A G(\mathbf{x},\mathbf{y})\,\omega_1(\mathbf{y})\,dA_{\mathbf{y}} = \mathcal{B}\,\omega_1(\mathbf{x})\,.$$

Therefore, this SCD solution is an eigenvector of the operator $\mathcal{B}$ with $\lambda = 1$. This SCD creates a constant potential in the outmost surface and throughout the whole interior of the conductive system, the head.

From this analysis, and our deduction that operators $\mathcal{B}$ and $\mathcal{B}'$ are adjoint, then we have also constructed the eigenvector $\bar{\sigma}\phi_1(\mathbf{x})$ corresponding to $\lambda' = 1$ for $\mathcal{B}'$. Specifically, the eigenvector corresponds to a potential that is constant at the outermost interface, which also takes this constant value inside the conductor. Note, however, that this potential is set to zero at the reference point at infinity to avoid any ambiguity in the GIE solution.

We can also note one more characteristic of the eigenvector corresponding to $\lambda = 1$. Specifically, we consider the case where the constant potential at the outmost surface is positive. The electric field just outside this surface must point outwards as the potential must decrease to reach its zero value at infinity. Therefore, at all points of the surface, the local charge density must be positive. Then the accumulated charge obtained by integrating the local charge density, is also positive: $Q_1 = \int_A \omega_1(\mathbf{x})\,dA_{\mathbf{x}} \neq$

0. On the other hand, it can be shown that the eigenvectors for all other eigenvalues, $\lambda \neq 1$, carry zero net charge, $Q_{\lambda \neq 1} = 0$.

Chapter 6

SOLUTIONS SPACE OF THE SURFACE CHARGE METHOD

This chapter describes the space of solutions of the forward problem and its connection to the eigenvalue structure of the integral operators that appear in SCM and GIE. Using these results, a new method of solution of the forward problem is proposed, based on the truncation of the space of eigenvectors of these operators.

6.1 Solutions Space

The eigenanalysis discussed in the previous section can be used to construct solutions to both SCM and GIE. First, is necessary to identify the space of possible solutions. When a solution to equation (5) exists, it is not unique. If $\omega_A(\mathbf{x})$ is a solution to the SCM, then adding a scalar multiple of the $\lambda = 1$ eigenvector $\omega_1(\mathbf{x})$ produces a new solution $\omega_A + \alpha\omega_1$, with α a real number. A similar result also follows for the GIE. This fact can be also be expressed indicating that the operators $(\mathcal{I} - \mathcal{B})$ and $(\mathcal{I} - \mathcal{B}')$ have kernels of dimension one. From the results in Section 5.6, there is a clear physical interpretation of the ambiguity in the solutions. The addition of a multiple of the charge distribution $\omega_1(\mathbf{x})$ does not change the fields in the inside of the head and simply modifies the external fields. In the GIE approach, we can add a constant value to the potential throughout the head while keeping the reference value at infinite equal to zero. This method produces a truly new physical solution and it is not simply a reflection of the freedom to add a constant potential value everywhere.

The argument for the non-uniqueness of the solution can also be obtained from analysis of the PDE expressing current conservation (5.1). For this, it is convenient again to separate space into the outer region, the air, with zero conductivity, and an

interior region with non-zero conductivity. In the interior, in regions of homogeneous conductivities, the PDE reduces to the Laplace or Poisson equations and also leads to a relation between the limit values of the electric field at boundaries between those regions. On the other hand, in the exterior region, there is no current and the equation is null. Instead of the current conservation equation, the field there is determined from Gauss law $\nabla \cdot \mathbf{E} = 0$. Current continuity at the interface between the inner and outer regions (labeled i and o), $\sigma_i \mathbf{n} \cdot \mathbf{E}_i = \sigma_o \mathbf{n} \cdot \mathbf{E}_o = 0$, requires the limit of the internal normal component of the field to be zero but does not restrict the outer field. The potential at this interface is continuous. The internal region problem thus has a Neumann condition for the potential and its solution is unique up to a constant in that region. The external region has a Dirichlet boundary condition given by the potential from the inner region and, in addition, can be set to have a zero value at infinity. This construction provides a one dimensional space of solutions for any given source. The difference between any two of these provides a solution of the problem with no sources. Such solutions can be seen to be eigenvectors of the GIE with $\lambda = 1$. Therefore, this eigenspace is one-dimensional.

To make the solution unique, an extra condition should be imposed. For a given internal source, members of the one dimensional family of solutions found can be distinguished from each other by the net charge they carry. In practical applications is possible to assume that the human head carries no net charge. The condition of no net charge can be used to single out a unique canonical physical solution to the problem of determining the potential and accumulated charges for the prescribed source. The projection method outlined below produces, in essence, such solution.

6.2 Neural Dipole Sources

The presence of a kernel for the operators $(\mathcal{I}-\mathcal{B})$ and $(\mathcal{I}-\mathcal{B}')$ implies that there is a restriction in the space of sources as well. In the solution of the integral equations the inverses of these operators act on the charge directly induced by the source $\mathcal{C}\rho_s$. This directly induced charge should not have a component in the space of kernels of the operators. However, this restriction has also a clear interpretation and causes no consistency problems for the SCM and GIE. As noted above, the total surface charge Q_1 for $\lambda=1$ is not zero, but it vanishes for all other values. Therefore, the restriction in the space of sources is that the surface density directly induced by the source must integrate to zero. This directly induced surface density is calculated as

$$\omega_s(\mathbf{x}) = \int_V s(\mathbf{y})\,\mathbf{n}(\mathbf{y})\cdot\nabla_x G(\mathbf{x},\mathbf{y})\,\rho_s(\mathbf{y})\,dV_{\mathbf{y}},$$

so that the restriction that the total charge be zero is

$$Q_s = \int_A \omega_s(\mathbf{x})\,dA_{\mathbf{x}} = 0\,.$$

This condition is immediately satisfied by dipolar sources. This follows since the integration becomes a sum over all the interfaces, and at each interface, the accumulated charge is proportional, by Gauss' law, to the charge of the source, which for dipoles is zero.

6.3 Projection Method

Even though the SCM equations are mathematically consistent in the case of dipole sources, it is still necessary to develop a practical implementation method. The formal solution $\omega=(\mathcal{I}-\mathcal{B})^{-1}\mathcal{C}\rho_s$ cannot be carried out since the operator $(\mathcal{I}-\mathcal{B})$ is not invertible. This issue can be circumvented by considering the equation in a subspace where the critical eigenvector is excluded. In practice, this goal posses

concrete challenges as the eigenvalues of discretized surfaces does not fully satisfy the bounds for the operators $\mathcal{B}$ or $\mathcal{B}'$ and in spite of its clear physical interpretation, the eigenvectors might not be directly constructed. Furthermore, eigenvectors with eigenvalues close to $\lambda = 1$, create high numeric sensitivity as the solution effectively contains the value $1/(1-\lambda)$.

A practical solution to the aforementioned problems is to find a solution in an SCD subspace that excludes a whole range of eigenvalues close to the critical value using a projection operator $\mathcal{P}$. The operators $\mathcal{B}$ and $\mathcal{B}'$ can be easily adapted to this subspace using their spectral decomposition. In particular, we must solve the equation

$$\omega = (\mathcal{I} - \mathcal{B})_p^{-1} \, \mathcal{P} \, \mathcal{C} \, \rho_s. \tag{6.1}$$

Here, $(\mathcal{I}-\mathcal{B})_p^{-1}$ acts as the pseudoinverse of the operator $(\mathcal{I}-\mathcal{B})$ in the subspace. The projection eliminates a number of eigenvectors that are not singular in the solution. The effect of this elimination can be checked in specific models, such as the set of concentric spheres. In this example, the critical eigenvector is isolated but, upon discretization, a number of eigenvectors appear with neighboring eigenvalues. Their elimination by the projection procedure does not directly affect the space that carries most of the relevant information.

6.4 Comparison to Deflation Approach

We briefly contrast the projection method with the basic deflation approach (as discussed, for example, in [84]). In the GIE formulation, the $\lambda = 1$ eigenvector is a function of the form $\psi(\mathbf{x}) = \bar{\sigma}(\mathbf{x})\phi(\mathbf{x})$ with ϕ a constant potential value. The deflation method modifies the integral operator kernel $B'(\mathbf{x}, \mathbf{y})$ by adding a term proportional to $\bar{\sigma}(\mathbf{x})/\bar{\sigma}(\mathbf{y})$. This addition leaves the eigenvalue system unmodified except for the

critical value $\lambda = 1$. For the modified operator, with a suitable normalization of the added term, the same eigenvector acquires an eigenvalue $\lambda = 0$. When the operator is applied to any other original eigenvector ψ_λ, it returns a value $\lambda\psi_\lambda + \alpha(\lambda)\psi_1$. The net result is to modify solutions of the original equation by adding a constant potential value at interfaces. This constant value can be ignored in applications that look only at potential differences at the scalp. There are two practical problems that appear with this method when the integral equation is discretized. First, the eigenvectors and eigenvalues of the modified operator will not have the properties exhibited by the continuum form and thus the solutions obtained will not exactly follow the pattern sought. A second issue is that there might be other eigenvalues near the critical value $\lambda = 1$ that, while not producing invertibility problems, do lead to high sensitivity of the solutions. The projection method outlined above, by explicitly considering the eigenvalues, avoids these problems.

Chapter 7

FINITE ELEMENT IMPLEMENTATION OF THE SCM

This chapter provides details of the finite element implementation of the projection method for forward. It also presents numerical examples of solutions for realistic heads.

7.1 Surface Description

The integral equation in (5.7) can be effectively solved to obtain the induced charge distribution for a known dipolar source given a known set of values for the conductivity and a given explicit shape of the head environment. Numerical solutions of the equation are obtained by discretization of the interfaces between regions of constant conductivity. We consider the head volume to be composed of $N_r + 1$ concentric regions R_i, indexed by $i = 0, 1, \ldots, N_r$. The region R_0 is the surrounding air. The dipole source is assumed to always be within the brain region, which is assumed to be the innermost region with index N_r. When considering only concentric regions, the boundaries between regions of constant conductivity define a number N_r of surfaces; these are assumed to be non-intersecting. The surfaces are oriented and the normal vector at a surface point is always oriented outwardly.

To proceed numerically, the N_r interfaces are discretized as a set of triangulated meshes. As the surfaces are disconnected, the discretizations are independent. The triangles and vertices that comprise the triangulations can be grouped together into a total set with N_g triangles and N_v vertices. The spatial location of vertex v is the three dimensional row vector $\mathbf{v}_v$. The full set of vertices then forms the array $\mathbf{V}$ of size $N_v \times 3$; the row number in this array is the index of the vertex. The triangles in the

meshes are described by the indices of their three vertices. Thus, to the gth triangle, we associate the 3-D integer vector $[v_{g,1}, v_{g,2}, v_{g,3}]$, where $v_{g,i}$ are the row indices for the vertices. During the construction of the meshes, it is useful to keep track of the orientation of the surfaces. The order of the vertices is chosen so that if they are followed in the order given, the circuit produces a counterclockwise circulation around the normal vector of the triangle. The normal vectors $\mathbf{n}_g$ of the triangles are chosen to reproduce the orientation of the continuous surface that is represented. The position $\mathbf{x}_g$ of the center of the gth triangle is easily calculated as the average of the positions of its three vertices. The area of the gth triangle is denoted as A_g. The conductivity ratio s_i is uniform at each interface S_i. This value is then given to each triangle in the surface. We form the vector $\mathbf{s}$ of size N_g containing the values of the ratio for each of the triangles.

The key variable of the system is the surface charge density. In the mesh, this is described by its values at the centers of the triangles $\omega(\mathbf{x}_g)$. It is more convenient, however, to work with the net charge in each of the mesh triangles. We construct the vector $\mathbf{w}$ with entries $w_g = A_g\omega(\mathbf{x}_g)$. That is, the charge density is evaluated at the center of the triangles and the charge is obtained by multiplying by the area of the triangle.

7.2 Matrix Form of Integral Equations

Upon discretization of the interfaces, the integral equation (5.6) is approximated by a linear equation of the form

$$\mathbf{w} = \mathbf{B}\mathbf{w} + \mathbf{C}\mathbf{p}\,.$$

In this expression, $\mathbf{p}$ is the current source dipole vector presented as a 3×1 column vector. The matrices $\mathbf{B}$ and $\mathbf{C}$ are the corresponding discretizations of the operators

$\mathcal{B}$ and $\mathcal{C}$. The matrix $\mathbf{B}$ captures the interaction between the charges at interfaces while $\mathbf{C}$ couples the dipole source to these charges.

The matrix elements $B_{gg'}$ of the matrix $\mathbf{B}$ are obtained from evaluation of the normal component of the electric field at the triangle g, due to a charge in triangle g' which is considered to be accumulated at its center, $\mathbf{x}_{g'}$. A direct evaluation at the center of triangle g, however, leads to poor properties of the $\mathbf{B}$ matrix. Instead, it can be shown that the integration over the surface of the triangle leads to a term proportional to the solid angle $\Omega_{gg'}$ defined by the triangle surface when observed from $\mathbf{x}_{g'}$ [85]. These matrix elements are

$$B_{gg'} = -\frac{1}{4\pi} s_g u \, \Omega_{g'}.$$

Here u is the sign of the component of the field at the surface $\mathbf{E}$ along the normal $\mathbf{n}$ at the surface. In this definition, diagonal matrix elements can be taken as zero, $B_{gg} = 0$. The matrix $\mathbf{B}$ is of dimensions $N_g \times N_g$.

The matrix $\mathbf{C}$ is of dimensions $N_g \times 3$ and its components are proportional to the normal component of the electric field $E^{(s)}_{n,gj}$ due to the dipole source pointing in the Cartesian direction j, observed at location $\mathbf{x}_g$. For a dipole source in a general direction, the normal field $E^{(s)}_{n,g}$ is

$$\varepsilon_0 E^{(s)}_{n,g} = \frac{1}{4\pi} \left[\frac{3(\Delta\mathbf{x}^{(s)}_g \cdot \mathbf{p})(\Delta\mathbf{x}^{(s)}_g \cdot \mathbf{n}_g)}{|\Delta\mathbf{x}^{(s)}_g|^5} - \frac{\mathbf{p} \cdot \mathbf{n}_g}{|\Delta\mathbf{x}^{(s)}_g|^3} \right]$$

with $\Delta\mathbf{x}^{(s)}_g = \mathbf{x}_g - \mathbf{x}^{(s)}$ the relative location of the gth triangle center with respect to the source. Evaluation of this expression when the dipole vector $\mathbf{p}$ is a unit vector in the jth direction defines the value of $E^{(s)}_{n,gj}$. We can then write the elements of the $\mathbf{C}$ matrix as

$$C_{gj} = -s_g A_g \varepsilon_0 E^{(s)}_{n,gj}.$$

After the solution of the discretized version of the integral equation for the charge density, the electric potential ϕ can be evaluated using the relation (5.4). The values of the potential at the centers of the triangles form a vertical vector Φ of size N_g. The discretized version of this evaluation takes the form

$$\Phi = \mathbf{H}^{(c)}\mathbf{w} + \mathbf{H}^{(s)}\mathbf{p} \tag{7.1}$$

The first term calculates the potential due to the charges associated to the triangles in the mesh. The matrix $\mathbf{H}^{(c)}$ is of size $N_g \times N_g$ and its non-diagonal entries have the form

$$H^{(c)}_{gg'} = (4\pi\varepsilon_0)^{-1}|\Delta\mathbf{x}_{gg'}|^{-1}$$

where, as before, $\Delta\mathbf{x}_{gg'}$ is the relative position of the centers of the triangles g and g'. The diagonal element $H^{(c)}_{gg}$ is the potential created, at the center of the gth triangle, by a uniform charge density in the same triangle. This value is finite and can be calculated by constructing the g-triangle by joining or subtracting six right triangles. Three intermediate triangles are formed by joining the center with the vertices. Each of these subtriangles is decomposed into the join or difference of two right triangles; the difference is needed in cases where the original triangle has an angle larger than $\pi/2$. The matrix element is the sum over these six components $H_{gg} = (4\pi\varepsilon_0 A_g)^{-1}\sum_{i=1}^{i=6} \pm h_{gi}$, where negatives ae used for subtracted triangles. For each triangle $h_{gi} = d_i \ln(\sec\theta + \tan\theta)$ with θ the angle at the vertex corresponding to the center of the original triangle, and d_i the normal distance from original center to original side.

The second term in (7.1) calculates the potential due to the dipole at each of the triangle centers. The potential at position $\mathbf{x}_g$ due to a dipole $\mathbf{p}$, using the notation

introduced above, is

$$\phi_g = \frac{1}{4\pi\varepsilon_0} \frac{\mathbf{p}\cdot\Delta\mathbf{x}_g^{(s)}}{|\Delta\mathbf{x}_g^{(s)}|^3}.$$

Evaluation of this expression when the dipole is a unit vector in the jth direction defines the value ϕ_{gj}. These values are assembled into the $N_g \times 3$ matrix $\mathbf{H}^{(s)}$ with entries

$$H_{gj}^{(s)} = \phi_{gj}\,.$$

7.3 Subspace Projection

The key result of the analysis of the properties of the operator $\mathcal{B}$ is that its eigenvector with $\lambda = 1$ cannot be part of the solution and that, in addition, all eigenspaces with eigenvalues near it can create numerical problems. If these issues were not present, any accurate numeric matrix inversion method could be used to obtain a solution in the form $\mathbf{w} = (\mathbf{I} - \mathbf{B})^{-1}\mathbf{C}\mathbf{p}$, where $\mathbf{I}$ is the identity matrix. On the other hand, we have argued that the eigenspaces near $\lambda = 1$ do not carry important information for the solution of the forward problem and can be safely eliminated. In the discrete formulation of the integral equations, this idea can be implemented by carrying out the operator inversion in (5.7) in a subspace that excludes eigenvalues in a finite range.

The right eigenvalues λ and respective eigenvectors $\mathbf{b}^\lambda$ of the matrix $\mathbf{B}$ can be numerically obtained. We denote by Λ the set of all eigenvalues, and by $\mathbf{W}$ the vector space of all possible triangulation charge vectors $\mathbf{w}$. The eigenvectors $\mathbf{b}^\lambda$ span the space $\mathbf{W}$. We choose a range of eigenvalues to be excluded, for example those in a range of the form $\lambda > \lambda_X$ for some value $\lambda_X < 1$. This selection partitions the eigenvalues into two sets, Λ_0 and Λ'. The first set contains all eigenvalues except those, near the value 1, as selected above. The excluded values form the set Λ'. The

sizes of these sets are N_{Λ_0} and $N_{\Lambda'}$ respectively. This selection defines the subspaces $\mathbf{W}_0$ and $\mathbf{W}'$ spanned by the eigenvectors associated to Λ_0 and Λ' respectively. We can then construct a base change matrix $\mathbf{L}$ such that its first N_{Λ_0} columns are the eigenvectors $\mathbf{b}^\lambda$ from $\mathbf{W}_0$ while the last $N_{\Lambda'}$ columns are eigenvectors from $\mathbf{W}'$. The inverse of this matrix, $\mathbf{L}^{-1}$ is well defined. In a base defined by the eigenvectors, a projector $\mathbf{P}$ into the subspace $\mathbf{W}_0$ can be constructed simply as a $N_{\Lambda_0} \times N_g$ matrix that is equal to the identity diagonal matrix in its first N_{Λ_0} rows, and zero in the rest.

The solution to the linear problem in (7.1) is now carried out within the subspace $\mathbf{W}_0$. That is, we compute the pseudo inverse $\mathbf{R}$ of $\mathbf{I} - \mathbf{B}$ in this subspace. Our approximate solution then reads:

$$\mathbf{w} = \mathbf{RCp}$$

and the pseudoinverse is explicitly constructed as

$$\mathbf{R} = \mathbf{L}\mathbf{P}^T[\mathbf{P}\mathbf{L}^{-1}(\mathbf{I} - \mathbf{B})\mathbf{L}\mathbf{P}^T]^{-1}\mathbf{P}\mathbf{L}^{-1}\,.$$

where the superscript T denotes vector transpose. In this expression, the matrix in the square brackets has dimensions $N_{\Lambda_0} \times N_{\Lambda_0}$ and is in fact a diagonal matrix with elements of the form $1 - \lambda$ in the diagonal, where λ is a non-excluded eigenvalue.

7.4 Computational Costs

The projection method outlined above increases the complexity of the calculation compared to that of the the simple deflation approach. Forward problem methods that include deflation steps, such as the symmetric method [66], can be in principle modified with the use of the projection method and thus general considerations regarding the added complexity are important beyond a direct comparison with a simple deflation implementation. The main computational added cost of the projection method is the determination of the eigenvalues and eigenvectors of the integral

operator. This operation adds $\mathcal{O}(N_t^3)$ operations to the calculation. The most important excess storage requirement of the method is the space needed for the eigenvector matrix of size N_t.

7.5 Numerical Examples

We applied the SCM method to two cases: a head model comprised of concentric spheres and a realistic shape head model. In both cases, the models have five different conductivity regions, separated by four interfaces. Proceeding inwards, these regions are: surrounding air R_0, scalp R_1, skull R_2, CSF R_3, and, R_4 the brain. The values of the conductivities for the realistic head model and the outer radius of the spherical model are shown in 7.1. The projection method was implemented using a cutoff of $\lambda_X = 0.97$. Namely, the pseudoinverse was carried out in the space span by eigenvectors with values lower than this limit.

Region	Description	Conductivity (S/m) (realistic head model)	Outer radius (m) (spherical model)
R_0	Air	0	∞
R_1	Scalp	0.44	0.1
R_2	Skull	0.018	0.095
R_3	CSF	1.79	0.09
R_4	Brain	0.25	0.085

Table 7.1: Realistic head parameters

These numerical examples presented here serve different goals. The spherical system, though can be used as a crude head model, is presented to assess the accuracy of the method as it can also be solved analytically as an infinite series. In addition, we have implemented a deflation method on the same meshes and with similar finite

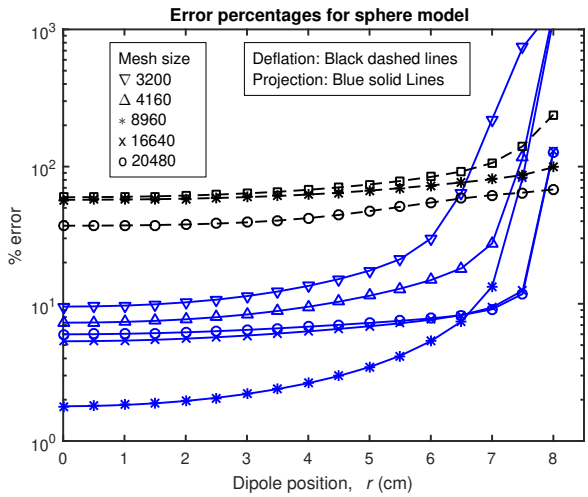

Figure 7.1: Error percentages for projection and deflation methods compared to analytical solutions for the concentric spheres system as a function of dipole position.

elements. The comparison shows the gain in accuracy that can be obtained by replacing deflation by projection. Other methods that solve the forward problem achieve better accuracy by employing double layers and higher order finite elements [66, 84] though still make use of deflation. Incorporation of projection into these methods should lead to increase accuracy and will be investigated in future work. For the realistic head shape system there is no established ground truth though it can be expected to exhibit similar error rates as the spherical one. Results for this case show qualitative stability of the method for more complex shapes and allows us to briefly discuss below the characteristics of the charge variables in addition to the potential itself.

Results for the spherical case are shown in Figure 7.5 for mesh sizes and dipole locations as indicated. The source dipole is radially directed. In all cases the dipole is located in the innermost region. The figure shows the error in the calculation when compared against the analytical result. The error is measured as the square root of the area weighted mean squared deviations divided by the area weighted mean of squared values of the analytic solution. For the projection method, increasing the grid size

leads to errors close to 6% for most positions of the dipole. Some intermediate grid sizes perform better for positions closer to the center. At positions closer to the first interface, radius r=8.5 cm, convergence is very slow. As shown, the deflation method produces a 30% error in the largest mesh used. Results for some intermediate mesh sizes, not shown in the graph, have larger errors. These intermediate mesh sizes have unequal triangle numbers for the different spheres, indicating considerable sensitivity to uneven triangulations. In previous work, for the basic deflation method, it was found that an increased mesh size could result in non-convergence [66, 84]. In the implementation used in this article, we observe convergence albeit with the noted high sensitivity to triangulation details. The projection method clearly improves on the deflation approach for similar finite elements, though it also retains some sensitivity to the triangulation. Use of more refined forms of finite elements have been shown to further reduced overall errors [86]. We expect this will also be the case for the projection method when implemented with higher order finite elements.

Both of the methods show non-monotonic error trends as the mesh size changes. To understand the origin of this feature it is useful to note that electrostatic problems of the type solved here have no characteristic microscopic length. When the surface is discretized, solutions to the problem depend on ratios of the form $\gamma = \ell/R$ where ℓ is a typical triangle size and R a macroscopic length in the system, such as the radius of the largest sphere. A successful discretization scheme would produce convergence to the analytic solution as $\gamma \to 0$.. We note, however, that this limit can also be understood as increasing the size of the system while maintaining fixed the typical triangle size and applying an overall multiplicative factor to the evaluated potentials. From this second point of view is clear that a wide variety of limit behaviors are possible and that results are sensitive to the explicit form of the triangulations and to the approximations implicit in the process. For example, we note that diagonal elements in the matrices

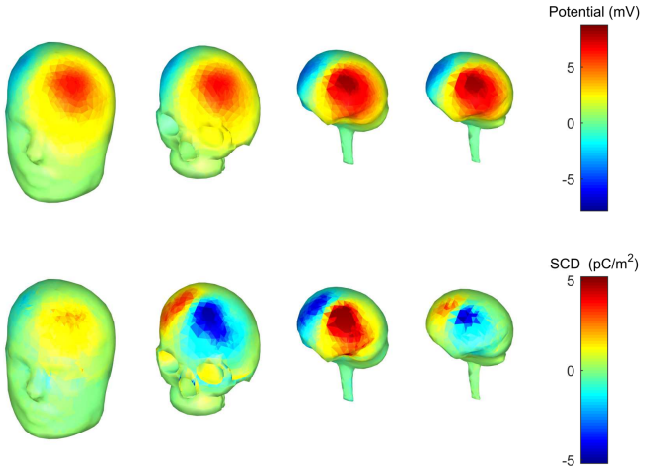

Figure 7.2: Results for a realistic head shape for the interfaces between the regions identified in Table I. Due to the different separation between regions, the potential and charge density show larger value amplitudes in the inner interfaces and are weaker than at the air scalp interface. The direction of the source dipole is reflected in the final potential distribution, and the SCD is alternating across consecutive interfaces.

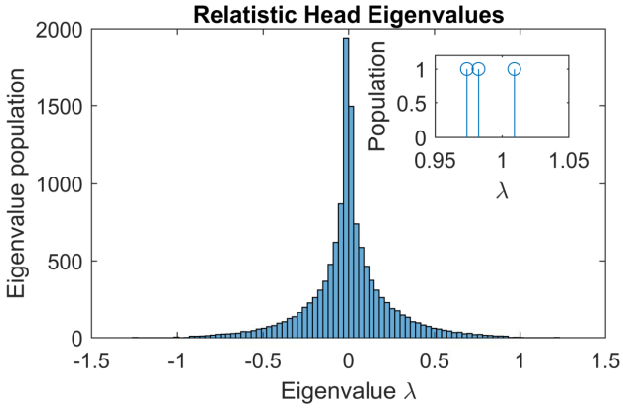

Figure 7.3: Eigenvalue population for the realistic head model. The population near the critical value $\lambda = 1$ is shown in the inset.

that appear in the problem need to be treated differently than off-diagonal elements to ensure that no fictitious divergent values enter into calculations. As the number of triangle increases, the relative relevance of the approximations in these two different types of matrix elements changes, and can produce non-uniform behavior in evaluation errors.

For a realist head shape, we used the CSH028 model with the provided volumetric tetrahedron discretization [87]. Using this discretization, a triangular mesh was

obtained for all interfaces between regions of constant conductivity. We edited some of the surfaces to avoid overlaps and refined the resulting grid for higher accuracy. The final discretization used 12,336 triangles to describe the interfaces. Figure 7.2 shows results for a dipole, located 2 cm below the top of the head, with magnitude $p = 1.0 \times 10^{-15} C \cdot m$. Both the potential and the charge acquire larger values in the inner interfaces than at the scalp. For this example, the discretization refinements were mainly applied to regions of the interfaces that were close to neighboring surfaces as well as to features with sharp edges. These two features are the main sources of error in the numerical solution of the problem.

A histogram of the eigenvalues for the realistic head is shown in Figure 7.3. The inset shows the eigenvalues λ near the critical value of 1 in more detail. When discrete approximations to smooth surfaces are used, the bounds are derived above are not strictly satisfied. In the perfectly smooth case, there is an eigenvalue $\lambda = 1$ but in the finite element case there is a small set of eigenvalues near and above the value of 1. Their corresponding eigenvectors are projected out to regularize the problem. The eigenvalues depend on the structure of the finite element. In particular, we note that the $\mathbf{B}$ matrix has better properties when constructed by means of solid angles instead of a simple center point evaluation of the electric field. With this construction method, the number of eigenvalues outside the expected bounds is greatly reduced. This example also demonstrated that the inhomogeneous term of the linear problem has very small components along the projected eigenvectors.

Chapter 8

CONDUCTIVITY MODELS

Solution of the inverse problem in EEG requires the use of a physical model. The Geselowitz integral equation (GIE), [23] for example, assumes that head tissues are purely conductive. Experiments show, however, that biological tissues are best described by complex conductivities indicating both conductive and capacitive behavior. This chapters discusses the connection between tissue structure and macroscopic electrical properties. The results from this work suggest that the physical models employed in EEG analysis should consider incorporating complex conductivities to improve their accuracy.

8.1 Confined Electrolytes in Tissues

The standard method of analysis of EEG signals for the purpose of identifying source locations uses a description of the head as composed of a number of different media with constant conductivities [23]. The signals are considered as associated to quasi-static current sources producing a dipolar potential. The purpose of this chapter is to connect this macroscopic description of head tissues with a mesoscopic, cellular-level picture of the underlying electric processes. In the macroscopic picture, charge concentration appears at the interface between regions with different conductivity. This phenomenon deserves more careful consideration at the mesoscopic level; it is worth considering the nature of the accumulated charge, its origin, and properties. Furthermore, mesoscopic models can indicate proper extensions of the macroscopic model with constant conductivities to situations where frequency dependent properties must be considered. The chapter discusses a novel model that addresses

these issues on the basis of the properties of confined liquid electrolytes which are, in essence, fundamental electrochemical models of cells and other biological structures.

In the literature on the subject, the response of a tissue to oscillating electric fields is usually separated into different frequency regimes [88]. When the source frequency is in the GHz range, the response is dominated by molecular level polarization and its features are labeled as γ-relaxation. In the MHz range, the response is dominated by ionic polarization; this is the β relaxation regime. At low frequencies larger structures are considered. It is well established that cells in suspension act as polarizable colloids [70, 89] and that their response is well characterized by a Debye type effective conductivity, with a single characteristic frequency response. This is known as the α-relaxation regime. Within most tissues, however, cells do not act as if in suspension. A model of tissues as composed of cells and other structures containing liquid electrolytes is more useful. This observation is exploited in detail next. It is shown that it is possible to understand a good number of electrical properties of tissues on the basis of this model.

The basic model discussed here is a simple confined electrolyte. In this picture, a macroscopic tissue simply consists of a group of similar confining regions, as shown in Figure 8.1. A detailed treatment of the effective electrical properties of a single compartment appears in the work by McDonald [90]. The results of this work, however, have not been applied to tissue conductivity. Application of oscillating electric fields to bounded electrolytes produces a polarized double layer as ions accumulate at its boundaries. Therefore, in addition to the conductive properties of the ion-rich liquid, consideration of the accumulation of charge at boundaries is required. An important insight of the work of MacDonald [90] is to note that during the application of external fields, an essentially uniform current is maintained in the bulk of the system. This, in turn, requires the presence of a bulk electric field. More complex analysis of

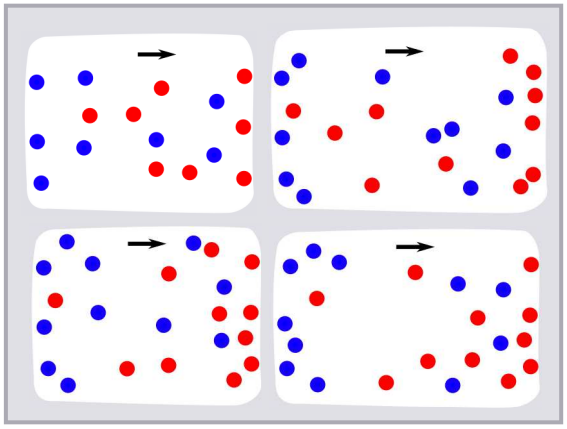

Figure 8.1: Scheme of cross section of an idealized tissue composed of multiple, similar regions of confined electrolytes. The ions, shown in red and blue for different charge type, move within these regions to produce net currents in the bulk of the separate regions. The arrows indicate the direction of motion of the positive ions in presence of a horizontal electric field.

the single compartment system has been carried out in the non-linear regime and for its transient aspects [91], but these results are not required for the present discussion.

In connecting these ideas to tissues, it is also useful to consider the precise nature of the macroscopic measurements. This is facilitated by consideration of the displacement current, that bridges the results for a single confined electrolyte to a full tissue.

8.2 Displacement Currents

In analyzing electrical conduction in tissues and other heterogeneous structures, it is necessary to consider not only the movement of ions *per se* but also the contribution of the electromagnetic field [92]. The total electromagnetic current $\mathbf{J}$ is the sum of the ionic current $\mathbf{j}$ and the displacement current $\mathbf{j}_D$. The displacement current is proportional to the time derivative of the electric field. In a material medium, the displacement current is $\mathbf{j}_D = \partial_t \mathbf{D}$, where the displacement vector $\mathbf{D}$ is the product of the relative permittivity ε, the free space permittivity ε_0, and the electric field $\mathbf{E}$, that is, $\mathbf{D} = \varepsilon\varepsilon_0\mathbf{E}$. The total elecromagnetic current is then :

$$\mathbf{J} = \mathbf{j} + \mathbf{j}_D = \mathbf{j} + \frac{\partial \mathbf{D}}{\partial t}.$$

The explicit consideration of these currents is necessary as we have a system with confined charges. Mobile ions in biologically systems, though relatively free to move in an aqueous environment, are essentially confined to tissue substructures such as cells and organelles. Even when ions are resent in larger structures such as blood vessels or the cerebro-spinal fluid, the ions must remain, for the most part, within specific spatial regions. Ions can be exchanged between regions by means of active transfer through pores. However, such processes are not significant in the analysis of the tissue response to external fields. Many organs, cells, and organelle walls have an effective zero ionic conductivity. Nevertheless, the regions they bound still contribute to an overall macroscopic conduction. The concentration of ionic species can be different across walls, and a macroscopic description that includes charge conservation must emerge from such settings where ions do not have large scale free-paths and the current carriers change from region to region. An even more extreme case of this issue occurs at the boundary between electrodes and tissues. Tissue conductivity is ionic in nature while, in electrodes, the carriers are electrons. The minute electronic conduction of tissues does not account for the current registered in measuring devices connected to tissues via electrodes. Only when displacement currents are considered can all pieces fall into place to recover a macroscopic picture of tissues as linear conductors. The issues noted here also apply to any heterogeneous material. However, standard frameworks allows the analysis of electric circuits to bypass these details; in RC circuits, the charge accumulation at the capacitors can replace the consideration of the displacement current. In the AC circuits, this charge accumulation is replaced by an imaginary (in the mathematical sense) current and leads to a description of the circuit with current conservation. These issues have been

recently reviewed by Eisenberg *et al.* [92].

The main reason to use the electromagnetic current is that it is conserved. In a medium, Ampere's equation can be written as $\mu_0(\mathbf{j} + \partial_t \mathbf{D}) = \nabla \times \mathbf{B}$, with $\mathbf{B}$ the magnetic field and μ_0 the magnetic permeability. Therefore, the electromagnetic current satisfies $\mathbf{J} = \mu_0^{-1} \nabla \times \mathbf{B}$. Taking the divergence on both sides leads to current conservation:

$$\nabla \cdot \mathbf{J} = 0. \tag{8.1}$$

In turn, this relation leads to the ionic current continuity equation

$$\partial_t \nabla \cdot \mathbf{D} = \partial_t \rho = -\nabla \cdot \mathbf{j}, \tag{8.2}$$

with ρ the charge density. While the ionic current is conserved only up to the consideration charge accumulation, the total electromagnetic current $\mathbf{J}$ is always conserved. It is this conservation that allows the construction of macroscopic conserved currents and connects the values of ionic currents across hard walls.

The structure of these currents, for the setting we are concerned, appears in Figure 8.2. The figure shows two neighboring regions with ionic content that are separated by a hard wall. An oscillatory external electric field is applied in the horizontal direction. The figure can be considered as showing the state of the system at the time where the oscillating external field is largest. There are three regions with different features. In the bulk region, far away from the wall, the combination of the external field and local contributions due to accumulated charges still produces a net field in the same direction as the external one. In this region, the ionic current $\mathbf{j}$ can be considered to be proportional to the net local field and satisfy the constitutive equation $\mathbf{j} = \sigma_0 \mathbf{E}$, with σ_0 the conductivity of the ionic medium. The bulk region is distant from the walls where ions accumulate, and there are no significant gradients to contribute as driving forces, to the creation of ionic currents. The total current in this region is

$\mathbf{J} = \sigma_0 \mathbf{E} + \partial_t \mathbf{D}$. It can be shown that in the electrolyte bulk the second term is much smaller than the first. In short, in an oscillatory field, the ratio of the two terms is $\sigma/\varepsilon\omega$, where ω is the external field frequency. For typical values in ionic systems, this ratio is very large, up to GHz frequencies and can be ignored in low frequency applications. Thus, in the bulk region, the electromagnetic current and the ionic current coincide:

$$\mathbf{J} \approx \mathbf{j}_B.$$

The B subindex emphasizes that the ionic current is evaluated in the bulk region. In a system that is effectively one dimensional, this implies that the current everywhere in the system is equal to the ionic current of any bulk region, even in places where the ionic current is zero. In more complex systems with three dimensional structures, the electromagnetic current does change but obeys the conservation condition $\nabla \cdot \mathbf{J} = \mathbf{0}$.

Next to the walls of the system, there is a region called the double layer, where ions accumulate as they are pushed by the field and diffusion gradient, but cannot escape due to the wall. The action of the oscillatory external field creates a time dependent accumulation of charge which in turn produces a time dependent contribution to the net electric field. In contrast to the bulk region, changes in the charge density produce non-negligible contributions to the displacement current. The displacement current exhibits large spatial variations as it accounts for the accumulation of charge $\partial_t \rho = \nabla \cdot \mathbf{j}_D$. Figure 8.2 shows a reduced ionic current and a compensating displacement current, both of which add to the value of the conserved total electromagnetic current.

In the hard wall region, there is no ionic current $\mathbf{j} = \mathbf{0}$, and the total current equals the displacement contribution $\mathbf{J} = \mathbf{j}_D$. The region is permeated by the time varying electric field. In the one dimensional, case the field must be spatially uniform since its divergence must be zero, $\nabla \cdot \mathbf{E} = \mathbf{0}$. In tissues and complex structures, the

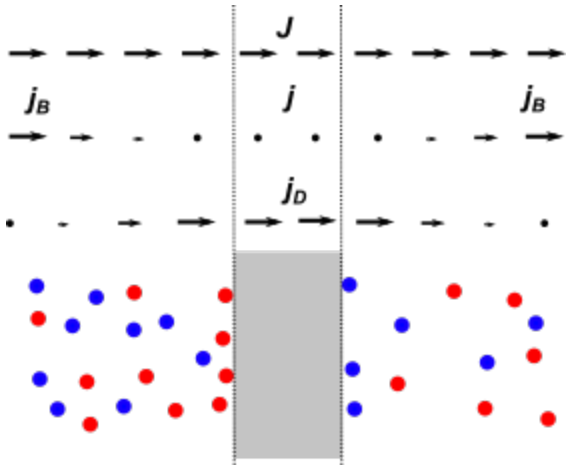

Figure 8.2: Scheme of two neighboring regions with confined electrolytes separated by a hard wall. The electrolyte's positive and negative ions are shown in an implicit aqueous background, and the wall is shown in gray. An external potential difference is applied in the horizontal direction. At the top of the scheme, the arrows indicate the direction and magnitude of the electromagnetic current $\mathbf{J}$, the ionic current $\mathbf{j}$ and the displacement current $\mathbf{j}_D$. The electromagnetic current is conserved and therefore, in this one-dimensional case, constant. The ionic current takes the bulk value $\mathbf{j}_B$ away from the wall in both of the neighboring compartments. The ion density in the two different compartments is not the same, but the bulk currents as well as the electromagnetic current, are the same.

field in the walls connects the electrical activity across regions.

In Figure 8.2 , the two compartments separated by the wall do not have the same properties and have, in particular, different ionic concentrations. The effective ionic conductivities of these two compartments, say (a) and (b), are $\sigma^{(a)}$and $\sigma^{(b)}$, with $\sigma^{(a)} \neq \sigma^{(b)}$. In the bulk regions of the two compartments, the ionic currents are $\mathbf{j}_B^{(a)}$ and $\mathbf{j}_B^{(b)}$. The previous analysis then shows that in a one dimensional geometry, or in slowly varying three dimensional structures, the ionic currents must be equal:

$$\mathbf{j}_B^{(a)} = \mathbf{J} = \mathbf{j}_B^{(b)}.$$

In short, in spite of the presence of a hard wall, the ionic current is continuous. Furthermore, if the ion rich bulk regions form the largest part of the system, these bulk currents can be used to define the average macroscopic current which is then

conserved. This current matches a intuitive notion of currents in tissues and heterogeneous structures. As such, unfortunately, it hides the role of the displacement current. Finally, it is worth noticing that the previous discussion carries over to tissues in contact with an electrode. Again, taking the view of an approximately one-dimensional system, the bulk current in the ionic region is equal to the bulk current, this time carried by electrons, within the wires of the measuring device. With superscripts indicating the evaluation region, the equality between the total current and the bulk currents in the two media is

$$\mathbf{j}_B^{(\text{wire})} = \mathbf{J} = \mathbf{j}_B^{(\text{tissue})}.$$

Remarkably, the ionic conduction seamlessly becomes the electronic current and thus the tissue can be simply thought as part of a standard electric circuit.

In the discussion of the bulk region for a compartment, it was noted that the ionic current can be phenomenologically related to the net electric field $\mathbf{j} = \sigma_0 \mathbf{E}$. This net field, however, is composed of the external field $\mathbf{E}_0$ and a field $\mathbf{E}_c$ created by charges in the medium, $\mathbf{E} = \mathbf{E}_0 + \mathbf{E}_c$. The second field is determined by the accumulated charge density ρ: $\nabla \cdot \varepsilon\varepsilon_0 \mathbf{E}_c = \rho$. In the bulk of the compartment, it is shown below that, in the complex representation of oscillating fields and currents, the two fields are proportional to each other. The constitutive equation can be then expressed in terms of the external field:

$$\mathbf{j}_B = \sigma_0 \mathbf{E} = \sigma_M \mathbf{E}_0.$$

This expression defines the effective conductivity σ_M, which can be identified with a macroscopic value. For notational simplicity this value will be denoted as $\sigma = \sigma_M$. In macroscopic measurements that relate external fields to currents, this value σ is the

measured constant of proportionality and thus defines the macroscopic conductivity. As shown in the next section, the value of σ can be calculated from the properties of the confined electrolyte system. A key feature of this effective macroscopic conductivity is its dependence on the frequency ω of the applied external field. When this point needs to be emphasized the notation $\sigma(\omega)$ will be used. Only at very high frequencies, when the oscillation period is so short that precludes charge accumulation, the effective conductivity and the pure parameter σ_0 coincide.

8.3 Conductivity of Confined Electrolytes

The properties of the confined electrolyte can be discussed from a coarse-grained level where average values of particle and charge density are meaningful. To simplify some of the discussion, the electrolyte is considered to consist of two charged species of 1:1 valence. The equilibrium number density of each of the ionic species, averaged over the whole confined region, is denoted by n_0. Though cells per se are usually not electroneutral, their charge is balanced by ions in the intercellular space. For simplicity, the compartments are assumed electroneutral so that both species have equal average concentrations. The analysis assumes an effective one dimensional geometry. The confining region is taken to be prismatic. The variable x denotes the coordinate along the field direction. The electrolyte rich regions is $-L/2 < x < L/2$.

Analysis of this system leads to a dynamic version of the Poisson-Boltzmann equation. Derivation details appear in the literature [90]. The key result is the equation for the charge density in the electrolyte region:

$$\partial_t \rho = D[\nabla^2 \rho - \kappa^2 \rho].$$

The inverse screening length κ is given by $\kappa^2 = \sigma_0/(\varepsilon\varepsilon_0 D) = 2e^2 n_0/(\varepsilon\varepsilon_0 k_B T_m)$. Here D is the diffusion constant, k_B is the Boltzmann constant, e the fundamental charge

and T_m is the temperature.

The dynamic equation for the charge density does not fully describe the system as, crucially, the potential is not uniquely determined for a given charge density. To determine the potential, the Poisson equation

$$-\varepsilon\varepsilon_0\nabla^2\phi = \rho$$

must be simultaneously solved along with the dynamic Possion-Boltzmann relation, Equation 8.3. The boundary conditions for the compartment considered are the no-particle flux at both hard walls, $\mathbf{j}|_{wall} = 0$, and the continuity of the displacement vector at the walls. For the multiple compartment system, the continuity of the potential and the displacement current provide the necessary boundary conditions.

In the case of oscillating external fields, solutions to the density and potential equation can be written as described next. For ease of notation, dynamical variables are expressed as the real part of complex numbers and oscillatory time dependence is factorized. The potential, for example, is $\phi(x,t) = Re[\phi(\omega,x)\exp(i\omega t)]$ where $\phi(\omega,x)$ is the frequency dependent complex amplitude. The same symbol $\phi(\cdot,\cdot)$ is used for variables in the time and frequency domains, but the quantities are differentiated by the time t and frequency ω variables.

In the one dimensional case, the potential can be expressed as

$$\phi(x,t) = -E_B(t)x + \phi_c(x,t)$$

where ϕ_c is the solution to the Poisson equation with zero derivative at the center point of the region $x = 0$. Here, E is the x-component of a constant electric field. This field can be understood as the bulk value of the total field and it exactly matches the total field at $x = 0$.

In a system with multiple similar cells, separated by finite thickness walls, solutions for the potential and ion concentration can be constructed that assume a periodic

behavior for the charge density and electric field and monotonic changes for the potential. The region $-L/2 < x < L/2$ has ions in an aqueous environment while the region $-T - L/2 \leq x \leq -L/2$ is the wall, of thickness T. The system repeats periodically along the x coordinate, with periodicity $L + T$.

Inside the aqueous region the ion concentration can be written as $\rho(x,t) = Re[\rho(\omega,x)\exp(i\omega t)]$. The spatial dependence of the solution is $\rho(\omega,x) = A\cosh(qx) + B\sinh(qx)$, where the complex inverse decay length q must satisfy the relation imposed by the dynamic equation,

$$i\omega = D[q^2 - \kappa^2].$$

At low frequencies the inverse decay length $q \approx \pm\kappa \pm i\omega/(2\kappa^2)$. From here on, the symbol q denotes the root with positive real value. For the low frequency case of interest, the magnitude of the inverse decay length is of the order of the screening length, $q \sim \kappa$, so that the charge density decays quickly away from the boundaries. This leads to the approximate form, near the left boundary, $\rho(\omega,x) = A\exp[-q(x + L/2)]$. Near the right boundary it is, similarly, $\rho(\omega,x) = -A\exp[q(x - L/2)]$. In these expressions, A is a complex amplitude that will be determined so as to be consistent with a prescribed value of the externally applied field.

Near the left boundary, the accumulated charge generates a potential of the form

$$\phi_c(\omega,x) = [A/\varepsilon_0\varepsilon q]\exp[q(x + L/2)]$$

The field associated to this potential is

$$E_c(\omega,x) = -[A/\varepsilon_0\varepsilon]\exp[q(x + L/2)]$$

The diffusion current $j_f = -D\nabla\rho$ is given by the gradient of the charge. The horizontal component of the frequency domain amplitude of this current is

$$j_f(\omega, x) = -qDA \exp[q(x + L/2)].$$

The net ionic current near this boundary is then

$$j(\omega, x) = [\sigma E_B + (\frac{\sigma A}{\varepsilon\varepsilon_0 q} - qDA) \exp(q(x + L/2))].$$

This quantity is zero at the left boundary. Solving this relation for the amplitude, and using the dispersion relation in Equation (8.3) leads to a value for the charge amplitude in terms of the bulk field.

$$A = \frac{iqD\kappa^2}{\omega}\varepsilon_0\varepsilon E_B = \frac{iq\sigma}{\omega}E_B.$$

The amplitude of the potential due to charge accumulation, evaluated at the left and right boundaries, $x = \pm L/2$, is denoted by $\phi_{c,L}$ and $\phi_{c,R}(\omega)$, respectively. Similarly, ϕ_L and ϕ_R denote the evaluation of the total potential ϕ at these points, which includes the contribution of the bulk field. Their values are given by

$$\phi_{c,L} = -i\frac{D\kappa^2}{q\omega}E_B, \tag{8.3}$$

with $\phi_{c,R} = -\phi_{c,L}$. The total potential also satisfies $\phi_R = -\phi_L$, and at the left boundary,

$$\phi_L = \left[-i\frac{D\kappa^2}{q\omega} + \frac{L}{2}\right] E_B. \tag{8.4}$$

In the wall region, with $-T - L/2 \leq x \leq -L/2$, the field is spatially uniform and the ion concentration is zero. In this region the field is given by

$$E(x, t) = Re[E_W \exp(i\omega t)],$$

and the potential is

$$\phi(x,t) = Re[-E_W(x + L/2) + \phi_L] \exp[i\omega t]$$

where ϕ_L is the left boundary value of the potential. The ionic current in this region is zero

$$j(\omega, x) = 0.$$

The displacement current in this region is

$$j_D(\omega, x) = i\omega\varepsilon_W E_W.$$

At the boundary between wall and aqueous region, the field satisfies the relation

$$\varepsilon_W E_W = \varepsilon E_L$$

where E_L is the amplitude of the field at the left boundary and ε_W is the relative permittivity of the wall. In terms of the bulk field value, this is $E_L = (1 - iD\kappa^2/\omega)E_B = (iDq^2/\omega)E_B$. Therefore, the amplitude of the oscillating field in the wall is

$$E_W = i\frac{\varepsilon}{\varepsilon_W}\frac{Dq^2}{\omega}E_B \tag{8.5}$$

and the displacement current is

$$j_D(\omega) = i\omega\varepsilon Dq^2 E_B.\} \tag{8.6}$$

The potential difference across the wall region is

$$\Delta\phi_W = -TE_W = i\frac{\varepsilon}{\varepsilon_W}\frac{TDq^2}{\omega}E_B.\} \tag{8.7}$$

To summarize, Equations 8.3, 8.3 and 8.7 relate the amplitudes of the density, and potential at the edges of the electrolyte region and the wall, to the bulk value of the

electric field. Next, this value will be determined for a prescribed external potential difference.

Figure 8.3 shows plots of the behavior described by these results. For these plots, the position along the current direction, x, is measured in units of the inverse screening length κ. The unit repeated cell has length $\kappa(L + L_W) = 20$. The conductivity is scaled so that $\sigma_0 = 1$. The potential is scaled so that the amplitude of the potential difference on a single repeating cell is $\Delta V = 1$. The field is scaled to units of potential times characteristic length.

In the context of electric circuits, the most important relation is the one between the potential difference at the boundaries of a circuit element and its current. The potential drop V, across a region consisting of an aqueous bulk of length L, with surrounding walls of thickness T, is

$$V(\omega) = \phi_L - \phi_R - \Delta\phi_W = 2\phi_c + LE_B - \Delta\phi_W.$$

This value can be expressed in terms of the bulk field E_B as

$$V(\omega) = [L - iA\frac{\varepsilon}{\varepsilon_W}\frac{Dq^2}{\omega} - i\frac{2D\kappa^2}{q\omega}]E_B.$$

At this point, it is useful to introduce the complex frequency ω_α, to denote the characteristic relaxation frequency of the macroscopic system. This is given by

$$\omega_\alpha = \frac{D\kappa}{L}[2 + \frac{\varepsilon}{\varepsilon_W}\frac{q^2}{\kappa}T] \approx \frac{D\kappa}{L}[2 + \frac{\varepsilon}{\varepsilon_W}\kappa T].$$

The approximate value in the right hand side of the equation is real. The second term in the square brackets of the approximate form can be large compared to 2, due, for example, to the large contrast of permittivities. The key feature of this quantity, however, is its dependence on the length L of the aqueous region.

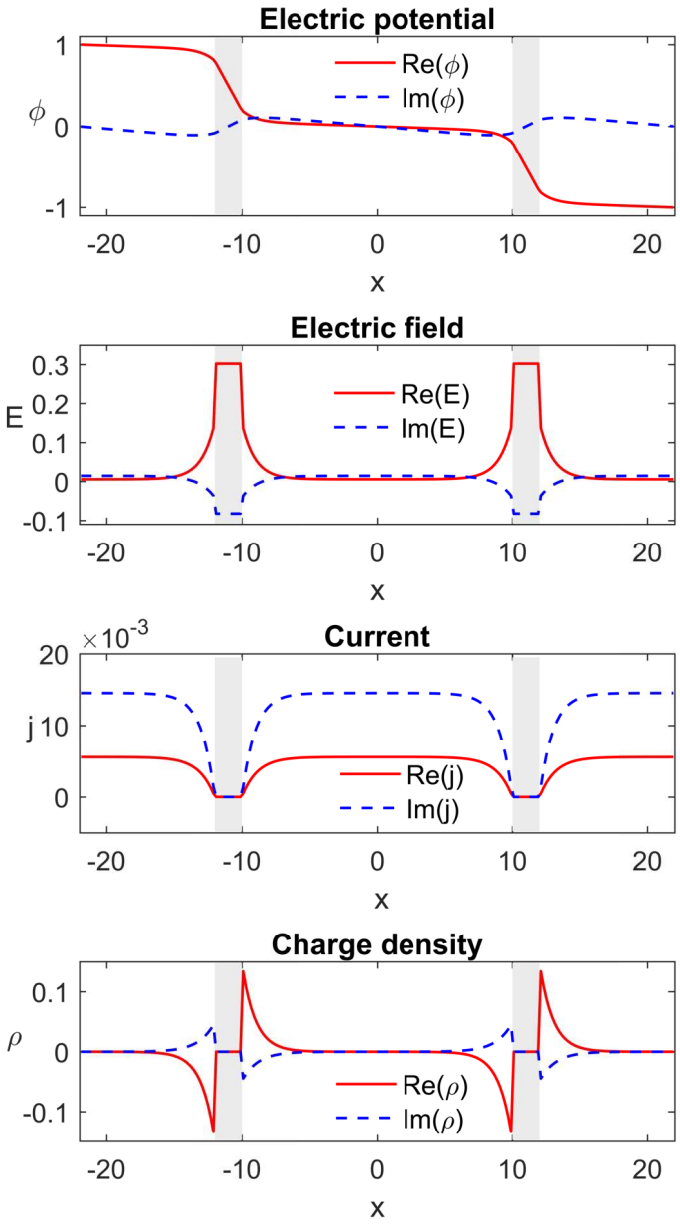

Figure 8.3: Plots of the real and imaginary parts of (a) potential, (b) charge density, (c) current and, (d) electric field, for a system with confined electrolytes under the action of an external, horizontal, oscillating field with complex potential $\Phi_{ext} = \Phi_0 \exp(i\omega t)$. The figures assume multiple similar confined regions along the horizontal direction. The region corresponding to the wall is shaded.

The ionic current density at the bulk locations j_B is

$$j_B = \sigma_0 E_B = \frac{\omega}{\omega - i\omega_\alpha}\sigma_0 \frac{V}{L}.$$

The total ionic current I through a transversal section of area S is

$$I = \frac{\omega}{\omega - i\omega_\alpha}\sigma_0 \frac{SV}{L}.$$

From this expression, the complex impedance of the region of volume $S \times (L + T)$ is given by

$$Z = \frac{L}{S}\left[1 - i\frac{\omega_\alpha}{\omega}\right]\frac{1}{\sigma_0}$$

This expression roughly corresponds to a simple RC series combination with the caveat that the frequency ω_α is complex. The resistance is simply provided by the bulk ionic conduction over the length of the compartment

$$R \approx \frac{1}{\sigma_0}\frac{L}{S}.$$

This is not an identity relation as the α frequency, as defined, is complex instead of purely real. The capacitance C at low frequencies is

$$C \approx \frac{\sigma_0}{Re(\omega_\alpha)}\frac{S}{L}.$$

In essence, this is the capacitance of the parallel plate capacitor with plate separation $\kappa^{-1} + T\varepsilon/\varepsilon_W$. At the macroscopic level, the whole confined region acts, therefore, as a single entity with effective macroscopic complex conductivity σ given by the Debye form

$$\sigma(\omega) = \frac{\omega}{\omega - i\omega_\alpha}\frac{L}{L+T}\sigma_0 = \frac{\omega}{\omega - i\omega_\alpha}\sigma_{0av}.$$

Here, to simplify the expression, the average value σ_{0av} over the region including the wall is used. It is standard to decompose this expression into its real and imaginary parts, σ'_M and σ''_M, so that $\sigma_M = \sigma'_M + i\sigma''_M$. As noted above, the characteristic frequency is complex but has a larger real part at low frequencies. In that case, the real and imaginary parts are

$$\sigma'(\omega) \approx \frac{\omega^2}{\omega^2 + \omega_\alpha^2}\sigma_{0av},$$

$$\sigma''(\omega) \approx \frac{\omega\omega_\alpha}{\omega^2 + \omega_\alpha^2}\sigma_{0av}.$$

These results indicate that, for frequencies near the α frequency, the AC effective conductivity is of the order of the free ion conductivity in the aqueous medium. The imaginary part of the conductivity can be interpreted as a frequency dependent permittivity $\varepsilon(\omega) = \sigma''/\varepsilon_0\omega$ so that

$$\varepsilon(\omega) \approx \frac{\omega_\alpha}{\omega^2 + \omega_\alpha^2}\frac{\sigma_{0av}}{\varepsilon_0}.$$

Figure 8.4 depicts plots of scaled real and imaginary parts of the conductivity and scaled permittivity. The figure also presents the Cole plot associated with these values. The deviation from the semicircular shape is due to the frequency dependence of the characteristic inverse length q. The conductivity plots are scaled to units where $\sigma_0 = 1$ and $\varepsilon(0) = 1$.

8.4 Comparison to Observed Properties

The previous calculations show that a Debye type response can be obtained from the model of confined electrolytes. For typical values of ionic concentrations, in the millimolar range, and structures of size of microns, the predicted α relaxation

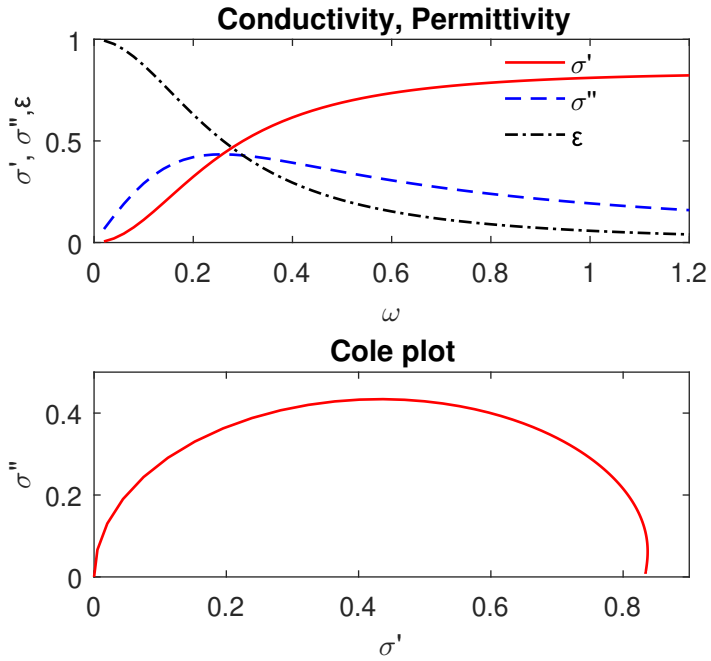

Figure 8.4: Plots of the (a) conductivity and permittivity and (b) Cole diagrams of the confined electrolyte.

frequency is 10^4 Hz, which is well within the range of the observed features.

The model described can be modified to include important details that apply to specific cases. In particular, modifications are required when the electrolyte-rich region occupies a much smaller region with more complex geometry. This would be the case, for example, when the electrolyte-rich region is an extracellular region, as is the case of the CSF.

Future work will address precise extensions of the model to other geometries and discuss the application to different types of tissues and physiological systems.

Chapter 9

CONCLUSIONS AND FUTURE WORK

This work has addressed three different aspects of the properties and applications of EEG. Namely, the implementation of sequential filters in source identification, elucidation of the structure of the forward problem when described using accumulated charge and power variables, and a mesoscopic view of the conductive properties of tissues.

9.1 Source Identification

The central objective of this component of the project is the application of a group of techniques, in particular sequential particle filters, to the problem of localization of evoked potentials in the presence of artifacts. The resulting method, is capable to recover the location of individual dynamic dipoles in test cases [93].

The method described was employed in a simplified setting with a three sphere head model. Its application becomes more difficult in the case of realistic heads as this requires solution of the forward problem as an intermediate step. The need for effective ways to solve the forward problem prompted a more detailed study of its solution methods. This work presents two contributions that aim at improving the accuracy of the solutions. The first is the use of power and charge variables to elucidate the properties of the forward problem as is commonly formulated, namely, as a solution of the Geselowitz integral equation [23]. The second contribution aimed to establish the validity of assumptions used in its most common formulation.

9.2 Power and Charge Variables

The second component of this work is the use of charge and power variables as part of the description of the EEG problem. Their use elucidates several of its features, both from the point of view of its physical interpretation and its mathematical structure. In particular, important features of the spectrum of the integral operator that defines the problem were obtained. A critical eigenvalue, that obstructs the straightforward solution of the forward problem was identified and interpreted. Key results have been described in this document and have appeared in publications [65, 80, 94].

Future work in this area includes further investigation of the consequences of the eigenvalue structure. The work presented here focused on implications for first order discretizations of surfaces, but consequences for higher order schemes should also be considered. Additionally, the explicit evaluation of surface charge densities at interfaces provides opportunities to connect this work with other approaches in the investigation of neural activity such as impedance tomography[95]. Results from this work are also likely of to be relevant in other bioelectricity problems such as the analysis of cardiac signals [74].

9.3 Tissue Models

The section on tissue modeling aims to examine commonly made assumptions in EEG investigations regarding the properties of head tissues. The Geselowitz model applies to conditions where the currents are considered to be in steady state and tissues are described by a constant conductivity [15, 23]. However, biological tissues exhibit frequency dependent conductivities [96]. The contribution in this work is to show that this second view is more accurate. The frequency dependence observed in experiments matches the properties that emerge from consideration of mesoscopic

models of cells. In particular, the model of tissues as confined electrolytes leads to Debye type relaxation characteristics often found in experimental investigations [96].

This work will be extended in several ways. First, it can be noted that the basic assumptions on which it is based apply not only to head tissues but to many other biological tissues. Therefore, its results can be tested and applied in other contexts. For EEG applications, the model provides a rational approach to the construction of whole head models that incorporate frequency dependence effects.

REFERENCES

[1] H. Damasio, T. Grabowski, R. Frank, A. M. Galaburda, A. R. Damasio *et al.*, "The return of Phineas Gage: clues about the brain from the skull of a famous patient," *Science*, vol. 264, no. 5162, pp. 1102–1105, 1994.

[2] L. Haas, "Hans Berger (1873–1941), Richard Caton (1842–1926), and electroencephalography," *Journal of Neurology, Neurosurgery & Psychiatry*, vol. 74, no. 1, pp. 9–9, 2003.

[3] S. Sanei and J. A. Chambers, *EEG Signal Processing*. John Wiley & Sons, 2013.

[4] S. Tong and N. V. Thakor, *Quantitative EEG analysis methods and clinical applications*. Artech House, 2009.

[5] A. G. Filler, "The history, development and impact of computed imaging in neurological diagnosis and neurosurgery: CT, MRI, and DTI," *Nature Precedings*, vol. 7, no. 1, pp. 1–69, 2009.

[6] J. Ashburner, J. G. Csernansk, C. Davatzikos, N. C. Fox, G. B. Frisoni, and P. M. Thompson, "Computer-assisted imaging to assess brain structure in healthy and diseased brains," *The Lancet Neurology*, vol. 2, no. 2, pp. 79–88, 2003.

[7] B. Z. Allison, E. W. Wolpaw, and J. R. Wolpaw, "Brain–computer interface systems: progress and prospects," *Expert review of medical devices*, vol. 4, no. 4, pp. 463–474, 2007.

[8] R. Grech, T. Cassar, J. Muscat, K. P. Camilleri, S. G. Fabri, M. Zervakis, P. Xanthopoulos, V. Sakkalis, and B. Vanrumste, "Review on solving the inverse problem in EEG source analysis," *Journal of neuroengineering and rehabilitation*, vol. 5, no. 1, p. 25, 2008.

[9] R. S. Bourne, C. Minelli, G. H. Mills, and R. Kandler, "Clinical review: Sleep measurement in critical care patients: research and clinical implications," *Critical Care*, vol. 11, no. 4, p. 226, 2007.

[10] J. R. Williamson, D. W. Bliss, D. W. Browne, and J. T. Narayanan, "Seizure prediction using EEG spatiotemporal correlation structure," *Epilepsy & Behavior*, vol. 25, no. 2, pp. 230–238, 2012.

[11] A. Delorme and S. Makeig, "EEGLAB: an open source toolbox for analysis of single-trial EEG dynamics including independent component analysis," *Journal of neuroscience methods*, vol. 134, no. 1, pp. 9–21, 2004.

[12] A. Gramfort, T. Papadopoulo, E. Olivi, and M. Clerc, "Forward field computation with OpenMEEG," *Computational Intelligence and Neuroscience*, 2011, 13 pages.

[13] G. H. Klem, H. O. Lüders, H. Jasper, and C. Elger, "The ten-twenty electrode system of the International Federation," *Electroencephalogr Clin Neurophysiol*, vol. 52, no. suppl., p. 3, 1999.

[14] S. Chatterjee and A. Miller, *Biomedical Instrumentation Systems*. Cengage Learning, 2010.

[15] P. L. Nunez and R. Srinivasan, *Electric fields of the brain: the neurophysics of EEG*. Oxford university press, 2006.

[16] H. Hallez, B. Vanrumste, R. Grech, J. Muscat, W. De Clercq, A. Vergult, Y. D'Asseler, K. P. Camilleri, S. G. Fabri, S. Van Huffel *et al.*, "Review on solving the forward problem in EEG source analysis," *Journal of neuroengineering and rehabilitation*, vol. 4, no. 1, p. 46, 2007.

[17] C. M. Michel, M. M. Murray, G. Lantz, S. Gonzalez, L. Spinelli, and R. G. de Peralta, "EEG source imaging," *Clinical neurophysiology*, vol. 115, no. 10, pp. 2195–2222, 2004.

[18] J. P. Ary, S. A. Klein, and D. H. Fender, "Location of sources of evoked scalp potentials: corrections for skull and scalp thicknesses," *Biomedical Engineering*, vol. 28, pp. 447–52, 1981.

[19] Y. Salu, L. G. Cohen, D. Rose, S. Sxato, C. Kufta, and M. Hallett, "An improved method for localizing electric brain dipoles," *IEEE Transactions on Biomedical Engineering*, vol. 37, no. 7, pp. 699–705, 1990.

[20] J. C. Mosher, R. M. Leahy, and P. S. Lewis, "EEG and MEG: forward solutions for inverse methods," *IEEE Transactions on Biomedical Engineering*, vol. 46, no. 3, pp. 245–259, 1999.

[21] Z. Zhang, "A fast method to compute surface potentials generated by dipoles within multilayer anisotropic spheres," *Physics in medicine and biology*, vol. 40, no. 3, p. 335, 1995.

[22] J. De Munck, M. Hämäläinen, and M. Peters, "The use of the asymptotic expansion to speed up the computation of a series of spherical harmonics," *Clinical Physics and Physiological Measurement*, vol. 12, no. A, p. 83, 1991.

[23] D. B. Geselowitz, "On bioelectric potentials in an inhomogeneous volume conductor," *Biophysical journal*, vol. 7, no. 1, p. 1, 1967.

[24] T. F. Oostendorp, J. Delbeke, and D. F. Stegeman, "The conductivity of the human skull: results of in vivo and in vitro measurements," *IEEE Transactions on Biomedical Engineering*, vol. 47, no. 11, pp. 1487–1492, 2000.

[25] K. P. Murphy, *Machine learning: a probabilistic perspective*. MIT press, 2012.

[26] R. E. Kalman, "A new approach to linear filtering and prediction problems," *Journal of Fluids Engineering*, vol. 82, no. 1, pp. 35–45, 1960.

[27] R. E. Kalman and R. S. Bucy, "New results in linear filtering and prediction theory," *Journal of Fluids Engineering*, vol. 83, no. 1, pp. 95–108, 1961.

[28] M. S. Arulampalam, S. Maskell, N. Gordon, and T. Clapp, "A tutorial on particle filters for online nonlinear/non-gaussian bayesian tracking," *Signal Processing, IEEE Transactions on*, vol. 50, no. 2, pp. 174–188, 2002.

[29] A. Smith, A. Doucet, N. de Freitas, and N. Gordon, *Sequential Monte Carlo methods in practice*. Springer Science & Business Media, 2013.

[30] G. Kitagawa, "The two-filter formula for smoothing and an implementation of the Gaussian-sum smoother," *Annals of the Institute of Statistical Mathematics*, vol. 46, no. 4, pp. 605–623, 1994.

[31] R. Chen and J. S. Liu, "Mixture kalman filters," *Journal of the Royal Statistical Society: Series B (Statistical Methodology)*, vol. 62, no. 3, pp. 493–508, 2000.

[32] H. Sidenbladh, "Multi-target particle filtering for the probability hypothesis density," *arXiv preprint cs/0303018*, 2003.

[33] O. Erdinc, P. Willett, and Y. Bar-Shalom, "Probability hypothesis density filter for multitarget multisensor tracking," in *2005 8th International Conference on Information Fusion*, vol. 1. IEEE, 2005, pp. 8–pp.

[34] D. E. Clark, K. Panta, and B.-N. Vo, "The GM-PHD filter multiple target tracker," in *2006 9th International Conference on Information Fusion*. IEEE, 2006, pp. 1–8.

[35] C. Jutten and J. Herault, "Blind separation of sources, part I: An adaptive algorithm based on neuromimetic architecture," *Signal Processing*, vol. 24, no. 1, pp. 1–10, 1991.

[36] P. Comon, "Independent component analysis, a new concept?" *Signal processing*, vol. 36, no. 3, pp. 287–314, 1994.

[37] A. Hyvärinen and E. Oja, "Independent component analysis: algorithms and applications," *Neural networks*, vol. 13, no. 4, pp. 411–430, 2000.

[38] S. Makeig, A. J. Bell, T.-P. Jung, T. J. Sejnowski *et al.*, "Independent component analysis of electroencephalographic data," *Advances in neural information processing systems*, pp. 145–151, 1996.

[39] A. Delorme, J. Palmer, J. Onton, R. Oostenveld, S. Makeig *et al.*, "Independent EEG sources are dipolar," *PloS one*, vol. 7, no. 2, p. e30135, 2012.

[40] C. M. Bishop, *Pattern recognition and machine learning*. springer, 2006.

[41] J. C. Mosher, P. S. Lewis, and R. M. Leahy, "Multiple dipole modeling and localization from spatio-temporal MEG data," *IEEE Transactions on Biomedical Engineering*, vol. 39, no. 6, pp. 541–557, 1992.

[42] J. C. Mosher and R. M. Leahy, "Source localization using recursively applied and projected (RAP) MUSIC," *IEEE Transactions on Signal Processing*, vol. 47, no. 2, pp. 332–340, 1999.

[43] B. D. Van Veen and K. M. Buckley, "Beamforming: A versatile approach to spatial filtering," *IEEE assp magazine*, vol. 5, no. 2, pp. 4–24, 1988.

[44] H. R. Mohseni, F. Ghaderi, E. E. Wilding, and S. Sanei, "A beamforming particle filter for EEG dipole source localization," in *IEEE International Conference on Acoustics, Speech and Signal Processing, 2009. ICASSP 2009.* IEEE, 2009, pp. 337–340.

[45] J. M. Antelis and J. Minguez, "Dynamic solution to the EEG source localization problem using Kalman filters and particle filters," in *Engineering in Medicine and Biology Society, 2009. EMBC 2009. Annual International Conference of the IEEE.* IEEE, 2009, pp. 77–80.

[46] E. Somersalo, A. Voutilainen, and J. Kaipio, "Non-stationary magnetoencephalography by Bayesian filtering of dipole models," *Inverse Problems*, vol. 19, no. 5, p. 1047, 2003.

[47] A. Sorrentino, L. Parkkonen, and M. Piana, "Particle filters: a new method for reconstructing multiple current dipoles from MEG data," in *International congress series*, vol. 1300. Elsevier, 2007, pp. 173–176.

[48] A. Sorrentino, L. Parkkonen, A. Pascarella, C. Campi, and M. Piana, "Dynamical MEG source modeling with multi-target Bayesian filtering," *Human brain mapping*, vol. 30, no. 6, pp. 1911–1921, 2009.

[49] A. Galka, O. Yamashita, T. Ozaki, R. Biscay, and P. Valdés-Sosa, "A solution to the dynamical inverse problem of EEG generation using spatiotemporal Kalman filtering," *NeuroImage*, vol. 23, no. 2, pp. 435–453, 2004.

[50] H. R. Mohseni, E. L. Wilding, and S. Sanei, "Sequential Monte Carlo techniques for EEG dipole placing and tracking," in *SAM 2008. 5th IEEE Sensor Array and Multichannel Signal Processing Workshop, 2008.* IEEE, 2008, pp. 95–98.

[51] C. Campi, A. Pascarella, A. Sorrentino, and M. Piana, "A Rao–Blackwellized particle filter for magnetoencephalography," *Inverse Problems*, vol. 24, no. 2, p. 025023, 2008.

[52] A. Pascarella, A. Sorrentino, C. Campi, and M. Piana, "Particle filtering, beamforming and multiple signal classification for the analysis of magnetoencephalography time series: a comparison of algorithms," *Inverse Problems and Imaging*, vol. 4, no. 1, pp. 169–170, 2010.

[53] C. Campi, A. Pascarella, A. Sorrentino, and M. Piana, "Highly automated dipole estimation (HADES)," *Computational intelligence and neuroscience*, vol. 2011, Article ID 982185, 11 pages, 2011.

[54] A. Maurer, L. Miao, J. J. Zhang, N. Kovvali, A. Papandreou-Suppappola, and C. Chakrabarti, "EEG/MEG artifact suppression for improved neural activity estimation," in *2012 Conference Record of the Forty Sixth Asilomar Conference on Signals, Systems and Computers (ASILOMAR)*. IEEE, 2012, pp. 1646–1650.

[55] L. Miao, J. J. Zhang, A. Papandreou-Suppappola, and C. Chakrabarti, "Neural activity tracking using spatial compressive particle filtering," in *2012 IEEE International Conference on Acoustics, Speech and Signal Processing (ICASSP)*. IEEE, 2012, pp. 3461–3464.

[56] L. Miao, J. J. Zhang, C. Chakrabarti, and A. Papandreou-Suppappola, "Efficient Bayesian tracking of multiple sources of neural activity: Algorithms and real-time FPGA implementation," *IEEE Transactions on Signal Processing*, vol. 61, no. 3, pp. 633–647, 2013.

[57] L. Miao, S. Michael, N. Kovvali, C. Chakrabarti, and A. Papandreou-Suppappola, "Multi-source neural activity estimation and sensor scheduling: algorithms and hardware implementation," *Journal of Signal Processing Systems*, vol. 70, no. 2, pp. 145–162, 2013.

[58] J. Jiang, "Multiple Neural Artifacts Suppression Using Gaussian Mixture Modeling and Probability Hypothesis Density Filtering," Master's thesis, Arizona State University, 2014.

[59] E. Somersalo, "The inverse problem of magnetoencephalography: Source localization and the shape of a ball," *SIAM News*, vol. 40, 2007.

[60] J. C. Mosher, R. M. Leahy, and P. S. Lewis, "EEG and MEG: Forward Solutions for Inverse Methods," *IEEE Transactions in Biomedical Engineering*, vol. 146, pp. 245–259, 1999.

[61] J. Sarvas, "Basic mathematical and electromagnetic concepts of the biomagnetic inverse problem," *Physics in Medicine & Biology*, vol. 32, pp. 11–22, 1987.

[62] A. Galka, O. Yamashita, T. Ozaki, R. Biscay *et al.*, "A solution to the dynamical inverse problem of EEG generation using spatiotemporal Kalman filtering," *NeuroImage*, vol. 23, pp. 435–453, 2004.

[63] A. Pascarella, A. Sorrentino, C. Campi, and M. Piana, "Particle filtering, beamforming and multiple signal classification for the analysis of MEG time series: A comparison of algorithms," *Inverse Problems and Imaging*, vol. 4, pp. 169–190, 2010.

[64] L. Miao, J. J. Zhang, C. Chakrabarti, and A. Papandreou-Suppappola, "Efficient Bayesian tracking of multiple sources of neural activity: Algorithms and real-time FPGA implementation," *IEEE Transactions on Signal Processing*, vol. 61, pp. 633–647, 2013.

[65] F. J. Solis and A. Papandreou-Suppappola, "Surface charge method for the forward EEG problem," in *Asilomar Conference on Signals, Systems and Computers*, 2016, pp. 1646–1650.

[66] J. Kybic, M. Clerc, T. Abboud, O. Faugeras *et al.*, "A common formalism for the integral formulations of the forward EEG problem," *IEEE Transactions on Medical Imaging*, vol. 24, pp. 12–28, 2005.

[67] M. S. Hamalainen and J. Sarvas, "Realistic conductivity geometry model of the human head for interpretation of neuromagnetic data," *IEEE Transactions on Biomedical Engineering*, vol. 36, pp. 165–171, 1989.

[68] N. G. Gençer and Z. Akalin-Acar, "Use of the isolated problem approach for multi-compartment BEM models of electro-magnetic source imaging," *Physics in Medicine & Biology*, vol. 50, pp. 3007–3022, 2005.

[69] M. Stenroos and J. Sarvas, "Bioelectromagnetic forward problem: Isolated source approach revis(it)ed," *Physics in Medicine & Biology*, vol. 57, pp. 3517–3355, 2012.

[70] H. P. Schwan, "Electrical properties of tissue and cell suspensions," in *Advances in Biological and Medical Physics*, 1957, vol. 5, pp. 147–209.

[71] P. A. Schwartzkroin, S. C. Baraban, and D. W. Hochman, "Osmolarity, ionic flux, and changes in brain excitability," *Epilepsy Research*, vol. 32, pp. 275–285, 1998.

[72] A. Villringer and B. Chance, "Non-invasive optical spectroscopy and imaging of human brain function," *Trends in Neurosciences*, vol. 20, pp. 435–442, 1997.

[73] P. Giacometti and S. G. Diamond, "Correspondence of electroencephalography and near-infrared spectroscopy sensitivities to the cerebral cortex using a high-density layout," *Neurophotonics*, vol. 1, pp. 1–24, 2014.

[74] S. N. Makarov, G. M. Noetscher, and A. Nazarian, *Low-frequency electromagnetic modeling for electrical and biological systems using MATLAB.* John Wiley & Sons, 2015.

[75] K. Barros, D. Sinkovits, and E. Luijten, "Efficient and accurate simulation of dynamic dielectric objects," *The Journal of Chemical Physics*, vol. 140, pp. 064 903–1–064 903–14, 2014.

[76] Y. Li and D. W. Oldenburg, "Aspects of charge accumulation in dc resistivity experiments," *Geophysical Prospecting*, vol. 39, no. 6, pp. 803–826, 1991.

[77] A. Adler and A. Boyle, "Electrical impedance tomography: Tissue properties to image measures," *IEEE Transactions on Biomedical Engineering*, vol. 64, no. 11, pp. 2494–2504, 2017.

[78] A. P. Calderón, "On an inverse boundary value problem," *Computational & Applied Mathematics*, vol. 25, pp. 133–138, 2006.

[79] Z. A. Acar, C. E. Acar, and S. Makeig, "Simultaneous head tissue conductivity and EEG source location estimation," *NeuroImage*, vol. 124, pp. 168–180, 2016.

[80] F. Solis and A. Papandreou-Suppappola, "Multiple interface brain and head models for EEG: A surface charge approach," in *Asilomar Conference on Signals, Systems and Computers*, 2017, pp. 1323–1327.

[81] S. N. Makarov, G. M. Noetscher, J. Yanamadala, M. W. Piazza *et al.*, "Virtual human models for electromagnetic studies and their applications," *IEEE Reviews in Biomedical Engineering*, pp. 95–121, 2017.

[82] M. S. Lynn and W. P. Timlake, "The use of multiple deflations in the numerical solution of singular systems of equations, with applications to potential theory," *SIAM Journal on Numerical Analysis*, vol. 5, pp. 303–322, 1968.

[83] P. Hammond, *Energy methods in electromagnetism*. Clarendon Press, 1981.

[84] H. Hallez, B. Vanrumste, R. Grech, J. Muscat *et al.*, "Review on solving the forward problem in EEG source analysis," *Journal of Neuroengineering and Rehabilitation*, vol. 4, 2007, 29 pages.

[85] B. He, Y. Wang, and D. Wu, "Estimating cortical potentials from scalp EEGs in a realistically shaped inhomogeneous head model by means of the boundary element method," *IEEE Transactions on Biomedical Engineering*, vol. 46, pp. 1264–1268, 1999.

[86] J. Kybic, M. Clerc, O. Faugeras, R. Keriven, and T. Papadopoulo, "Fast multipole acceleration of the MEG/EEG boundary element method," *Physics in Medicine and Biology*, vol. 50, pp. 4695–4710, 2005.

[87] A. Tizzard and R. H. Bayford, "Improving the finite element forward model of the human head by warping using elastic deformation," *Physiological Measurement*, vol. 28, p. S163, 2007.

[88] E. C. Burdette, J. Seals, S. P. Auda, A. D. Ambhire, and R. L. Magin, "Review of the dielectric properties of animal and human tumors determined from in vivo measurements," *Critical Reviews^{TM} in Biomedical Engineering*, vol. 44, no. 4, 2016.

[89] H. P. Schwan, "Electrical properties of tissues and cell suspensions: mechanisms and models," in *Proceedings of 16th Annual International Conference of the IEEE Engineering in Medicine and Biology Society*, vol. 1. IEEE, 1994, pp. A70–A71.

[90] J. R. Macdonald, "Double layer capacitance and relaxation in electrolytes and solids," *Transactions of the Faraday Society*, vol. 66, pp. 943–958, 1970.

[91] M. Z. Bazant, K. Thornton, and A. Ajdari, "Diffuse-charge dynamics in electrochemical systems," *Physical review E*, vol. 70, no. 2, p. 021506, 2004.

[92] B. Eisenberg, X. Oriols, and D. Ferry, "Dynamics of current, charge and mass," *Computational and Mathematical Biophysics*, vol. 5, no. 1, pp. 78–115, 2017.

[93] F. J. Solis, A. Maurer, J. Jiang, and A. Papandreou-Suppappola, "Adaptive EEG artifact suppression using Gaussian mixture modeling," in *Asilomar Conference on Signals, Systems and Computers*, 2015, pp. 607–611.

[94] F. J. Solis and A. Papandreou-Suppappola, "Power dissipation and surface charge in eeg: Application to eigenvalue structure of integral operators," *IEEE Transactions on Biomedical Engineering*, 2019.

[95] M. Cheney, D. Isaacson, and J. C. Newell, "Electrical impedance tomography," *SIAM review*, vol. 41, no. 1, pp. 85–101, 1999.

[96] R. D. Stoy, K. R. Foster, and H. P. Schwan, "Dielectric properties of mammalian tissues from 0.1 to 100 mhz; a summary of recent data," *Physics in Medicine & Biology*, vol. 27, no. 4, p. 501, 1982.